UNIVERSITY OF CALIFORNIA

Los Angeles

Error Protection Techniques for Source and Channel Coding

A dissertation submitted in partial satisfaction of the requirements for the degree Doctor of Philosophy in Electrical Engineering

by

Thomas W. Sun

2002

2002

© Copyright by

Thomas W. Sun

2002

The dissertation of Thomas W. Sun is approved.

Mario Gerla

Gregory J. Pottie

Kung Yao

Richard D. Wesel, Committee Chair

University of California, Los Angeles

2002

DEDICATION

To my parents,

who love me,

To Wei,

who loves and supports me,

To Frank,

who likes smiling

Contents

List of Figures

ACKNOWLEDGEMENTS

First of all, I would like to thank Professor Rick Wesel for accepting me as his student and giving me full support throughout my Ph.D. study. He is the best advisor I can imagine by actively helping in my research and giving wonderful comments to my papers. I really appreciate the support Professor Wesel gave to everyone in his research group by encouraging us to attend conferences, short courses, etc. I cannot thank him enough for his persistent help, support and encouragement in my research. He is indeed a role model, and his influence will definitely help me in the coming years. I hope that I can always have such rewarding experiences from all the places I will work in, and all the people I will work with.

I would also like to thank Professor Greg Pottie for advising me in course study when I came to UCLA, and Professor Babak Daneshrad for giving me the great opportunity of doing a wireless communications project.

Sincere thanks go to Professor Mario Gerla, Professor Greg Pottie, and Professor Kung Yao for investing their time to be on my doctoral committee.

I would also like to thank Professor Allan Willson from whom I learned a lot, not only about academics. His influence on me will also last lifetime.

I am very grateful to Dr. Jay Chang, Dr. Charles Chien, and Dr. Victor Lin at Rockwell Scientific for their help and discussion during my part time research work there. My experience at Rockwell helps me a lot in my academic career.

Many thanks to my group members, Addina Matache, Aditya Ramamoorthy, Cenk Kose, Jun Shi, Mark Shane, and Wen-Yen Weng, for being friendly and supportive. Many thanks to Chris Jones, Christina Fragouli, Christos Komninakis and Xueting Liu for their very useful discussions and help in my research. Special thanks to Chris Jones for the valuable discussions about simulation and Robertson and Wörz turbo TCM structure. Special thanks to Ramesh Pyndiah who posed the question addressed by Chapter 3 at ICC 2000.

I have benefited greatly from many other fellow students from their technical inputs and interactions and most importantly they have boosted my morale with their friendship which I have found most invaluable during my study at UCLA. I would like to mention them in my acknowledgment: Eric Berg, Jing Cao, Min Chen, Kyung-Ho Cho, Jining Duan, Dengwei Fu, Wei Fu, Jian Huang, Ryan Kim, Jing Ling, Sumit Mohan, Jeff Putnam, Jibing Wang, Charles Wu, Fan Xu, Zhan Yu, Jiaxiang Zhao, and Hanli Zou.

Very importantly, I like to thank my parents and my brother for their constant love, support and encouragement through my lifetime. Thank Wei Shi, my wife, for her endless love, understanding and support. Finally I like to thank Frank Sun, my little cute son, for being my child and bringing me a lot of fun.

VITA

1986	B.S. in Biomedical Engineering Shanghai Jiao Tong University Shanghai, P.R.China
1990	M.S. in Electrical Engineering Cleveland State University Cleveland, Ohio

PUBLICATIONS

- T. W. Sun, R. D. Wesel, M. R. Shane, and K. Jarett, "Superposition turbo TCM for degraded broadcast channels," submitted to *IEEE Transactions on Communications.*
- T. W. Sun, R. D. Wesel, M. R. Shane, and K. Jarett, "Superposition turbo TCM for degraded broadcast channels," submitted to ICC 2003, May 2003.
- T. W. Sun and R. D. Wesel, "Constellation labeling for error-resilient source coding of PAM," *Proc. of 35th Annual Conference on Information Sciences and Systems,* March, 2001.
- W. Shi, T. W. Sun and R. D. Wesel, "Quasiconvexity and optimal binary fusion for distributed detection with identical sensors in generalized Gaussian noise," *IEEE Transactions on Information Theory.* January 2000.
- W. Shi, T. W. Sun and R. D. Wesel, "Optimal binary distributed detection," *Proc. of 2000 IEEE International Symposium on Information Theory,* June, 2000.
- W. Shi, T. W. Sun and R. D. Wesel, "Optimal binary thresholds for distributed detection in Gaussian noise," *Proc. of the 33th Asilomar Conference on Signals, System & Computers,* Oct., 1999.

- T. W. Sun, A. N. Willson Jr., "A datafusion model and its application in multiuser detection using successive interference cancellation in DS/CDMA systems," *Proc. of the IEEE International Conference on 3rd Generation Wireless Communications,* June 2000.

- J. Frigon, B. Daneshrad, J. Putnam, E. Berg, R. Kim, T. W. Sun, and H. Samueli, "Field trial results for high-speed wireless indoor data communications," *IEEE Journal on Selected Areas in Communications,* March 2000.

- J. Chang, T. W. Sun, J. Hu, and A. Wang, "Highly compact AC-AC converter achieving high throughput at 460V output," *Proceedings IPEMC 2000. Third International Power Electronics and Motion Control Conference,* August., 2000.

- J. Chang, T. W. Sun, A. Wang, and D. Braun, "Compact AC-AC converter using 3-in-1 IBPMs and adaptive commutation," *Proceedings of the IEEE 1999 International Conference on Power Electronics and Drive Systems. PEDS'99,* July., 1999.

- J. Chang, T. W. Sun, A. Wang, and D. Braun, "Medium power AC-AC converter based on integrated bidirectional power modules, adaptive commutation and DSP control," *Proceedings of 34th Annual Meeting of the IEEE Industry Applications,* October, 1999.

- J. Chang, T. W. Sun, and A. Wang, "Highly compact AC-AC converter achieving a high voltage transfer ratio," *IEEE Transactions on Industrial Electronics,* Vol. 49, April, 2002.

ABSTRACT OF THE DISSERTATION

Error Protection Techniques for Source and Channel Coding

by

Thomas W. Sun

Doctor of Philosophy in Electrical Engineering
University of California, Los Angeles, 2002
Professor Richard D. Wesel, Chair

Coding reduces error rate in digital communication systems. In this dissertation, several error protection techniques are discussed.

The first part of this dissertation shows that the superposition approach used by Bergmans and Cover may be implemented with turbo codes to provide performance within 1 dB of the capacity region boundary of the degraded broadcast channel at BER of 10^{-5}. Bergmans and Cover [1] identified the capacity region of the Gaussian degraded broadcast channel, where different receivers observe the transmitted signal with different signal to noise ratios. Performance is consistent over the entire useful range of the power allocation parameter α.

Coding for the degraded broadcast channel is equivalent to coding for unequal error protection. Adjusting α changes the transmitter constellation of our encoder, and changes the degree to which error protection is unequal. When α

is selected to provide equal error protection, the code is essentially a multilevel code. This multilevel code performs as well as single level turbo trellis-coded-modulation schemes with the advantage of the potential for flexible unequal error protection as α is varied.

The second part of this dissertation considers one dimensional (1-D) source data, such as the output of a linear quantizer, under the distortion criterion of maximum Euclidean distance. Under the assumption that bit errors are sparse, we seek a labeling that minimizes the maximum Euclidean distance associated with a single bit error. This quantity is defined as d_{max}. This dissertation lower bounds d_{max} and proposes a labeling which approaches that lower bound. The same d_{max} can be achieved for two dimensional (2-D) labeling with the direct product of two 1-D labelings.

In the third part of this dissertation, a distributed detection model with identical SNR distributions in local sensors is presented. For simplicity, identical local binary thresholds are used. This dissertation shows that for any admissible fusion rule, the probability of error is a quasi-convex function of threshold τ. Hence, the problem decomposes into a series of n quasi-convex optimization problems that may be solved using well-known techniques. The results hold for any distribution of transmission signal amplitudes. Based on the results for an odd number of decisions, a multiuser detector with a data fusion based successive interference cancellation (DFSIC) scheme for DS/CDMA systems is presented. With low complexity, and no additional delay, the bit error rate (BER) of DFSIC is significantly below that of a single-user receiver due to interference diversity.

Chapter 1

Introduction

High-speed data communication requires effective error correction. In this dissertation, some error protection techniques are presented.

The capacity region of the Gaussian degraded broadcast channel was identified by Bergmans and Cover in 1970's. The region can be theoretically achieved by superposition coding. However, prior to this dissertation, there was no close to capacity practical superposition code that performed close to the theoretical limits..

Chapter 2 of this dissertation presents a superposition turbo coding scheme that performs within 1 dB of the capacity region boundary of the degraded broadcast channel at BER of 10^{-5}. Since it offers multiple data rates supported at multiple SNRs, superposition coding for the degraded broadcast channel is equivalent to coding for unequal error protection. Our simulation results show that codes designed for equal Euclidean distance constellations provide consistent performance over the entire useful range of the power allocation parameter α. Adjusting α changes the Euclidean distance between any two adjacent constellation points of our encoder, and changes the degree of unequal error protection.

Chapter 2 also shows that the multilevel coding scheme is actually a special case of multi-rate degraded broadcast channel coding, when every receiver has the same error free SNR. This can be realized by adjusting data rates and the power allocation parameter α. It is also proved in Chapter 2 that the multi-rate superposition turbo TCM, when configured for single rate, can perform as well as the typical single rate turbo TCM. Comparing to typical single rate turbo TCM, our superposition turbo TCM offers multi-rate unequal error protection in addition, without any loss in terms of performance and complexity when configured as a single rate scheme.

We designed and simulated two-rate superposition turbo TCM utilizing 16-point square constellations and 8-point circular constellations, as well as three-rate superposition turbo TCM utilizing 64-point square constellations. We also designed and simulated a two-rate Robertson and Wörz based superposition turbo TCM in 16-QAM. All simulation results consistently show the performance within 1 dB of the theoretical capacity region boundary at a BER of 10^{-5}.

When lossy compression is followed by transmission over a noisy channel, the best combination of source and channel coding could be simply a properly labeled source to reduce the distortion of data received over such a channel. Chapter 3 considers one dimensional source data under the distortion criterion of maximum Euclidean distance. Assuming that the bit errors are rare in the received data, we try to find a labeling that minimizes the maximum Euclidean distance between any two points what have single Hamming distance. This quantity is defined as d_{max}. Chapter 3 lower bounds d_{max} and proposes a labeling which approaches that lower bound. The same performance can be achieved for two dimensional labeling by simply multiplying two one-dimensional labelings.

Due to the steady growth of wireless communication in distributed wireless sensor networks, decentralized detection and estimation has attracted interest recently. Chapter 4 is an application of wireless communications to wireless sensor networks. In wireless sensor networks, efforts have been made in designing the thresholds of individual sensors and the optimal fusion rule in the fusion center to get optimal performance. In [2], we studied a binary fusion distributed detection scheme with the assumption of identical sensors with AWGN channels. In Chapter 4, we consider the case that a binary fusion distributed detection with the assumption of identical sensors with fading channels. We present a technique to find the optimal threshold τ for the binary hypothesis detection problem with n identical and independent sensors in wireless sensor network. The sensors all use an identical and single threshold τ to make local decisions, and the fusion center makes a global decision based on the n local binary decisions. We show that for any admissible fusion rule, the probability of error is a quasi-convex function of the threshold τ. Hence, the problem decomposes into a series of n quasi-convex optimization problems that may be solved using well known techniques.

With the odd-number distributed multi-sensor network model, we present a multiuser detector with a data fusion based successive interference cancellation (DFSIC) scheme for DS/CDMA systems. Without complexity, and delay increase, the bit error rate of DFSIC decreases significantly due to the interference diversity.

The main contributions presented in this thesis are as follows:

- Designed a superposition turbo TCM scheme for degraded broadcast channel within 1 dB of the theoretical capacity limit.

- Proved that multilevel coding is a special case of superposition coding for a degraded channel.
- Showed that our multi-rate superposition turbo TCM has the same performance as the typical single-rate turbo TCM without increase any implementation complexity. In addition, our multi-rate scheme can provide unequal error protection.
- Designed a labeling that minimizes the maximum Euclidean distance associated with a single bit error for error-resilient source coding, and discovered two lower bounds for the labeling.
- Proved the quasi-convexity property of the multi-sensor detection problem with any fading channel and applied the odd-number multi-sensor model in successive interference cancellation in DS/CDMA systems.
- Derived a necessary and sufficient condition that a slicer is optimal: $ln(f(x))$ is concave, where $f(x)$ is the pdf of the additive noise.

Chapter 2

Superposition Turbo TCM for Multi-Rate Broadcast

2.1 Introduction of Chapter 2

In many applications, different receivers experience different signal-to-noise ratios (SNRs). For example, in satellite television broadcasting, receivers in rain-fades have very low SNR, while other receivers under clear sky have high SNRs.

With progressive source coding, the data from the video source encoder is not uniformly important. Thus, it is desirable that the most important data be recovered even by a receiver with poor receiving condition (i.e. low SNRs). An unequal error protection (UEP) code provides more protection to more important data, permitting it to be received on channels with lower SNR.

Coding for UEP is identical to coding for the degraded broadcast channel. Consider the Gaussian broadcast channel with one sender transmitting X and two receivers observing Y_1 and Y_2 respectively with

$$Y_1 = X + Z_1 \tag{2.1}$$

$$Y_2 = X + Z_2\,, \tag{2.2}$$

where $Z_1 \sim \mathcal{N}(0, N_1)$ and $Z_2 \sim \mathcal{N}(0, N_2)$ with $N_2 > N_1$. As in Figure 2.1, this broadcast channel can be re-characterized as the statistically equivalent "degraded" broadcast channel.

$$Y_1 = X + Z_1 \tag{2.3}$$

$$Y_2 = Y_1 + Z_2'\,, \tag{2.4}$$

where $Z_2' \sim \mathcal{N}(0, N_2 - N_1)$.

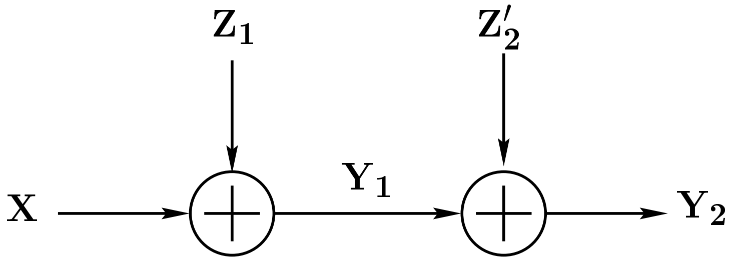

Figure 2.1: Gaussian degraded broadcast channel.

Let

$$C(x) = \log_2(1 + x) \tag{2.5}$$

denote the capacity in bits per channel use of a two dimensional memoryless Gaussian channel with SNR x.

The sender wishes to send information at rate-$(R_1 + R_2)$ to receiver 1, and part of the information for receiver 1 at rate-R_2 to receiver 2.

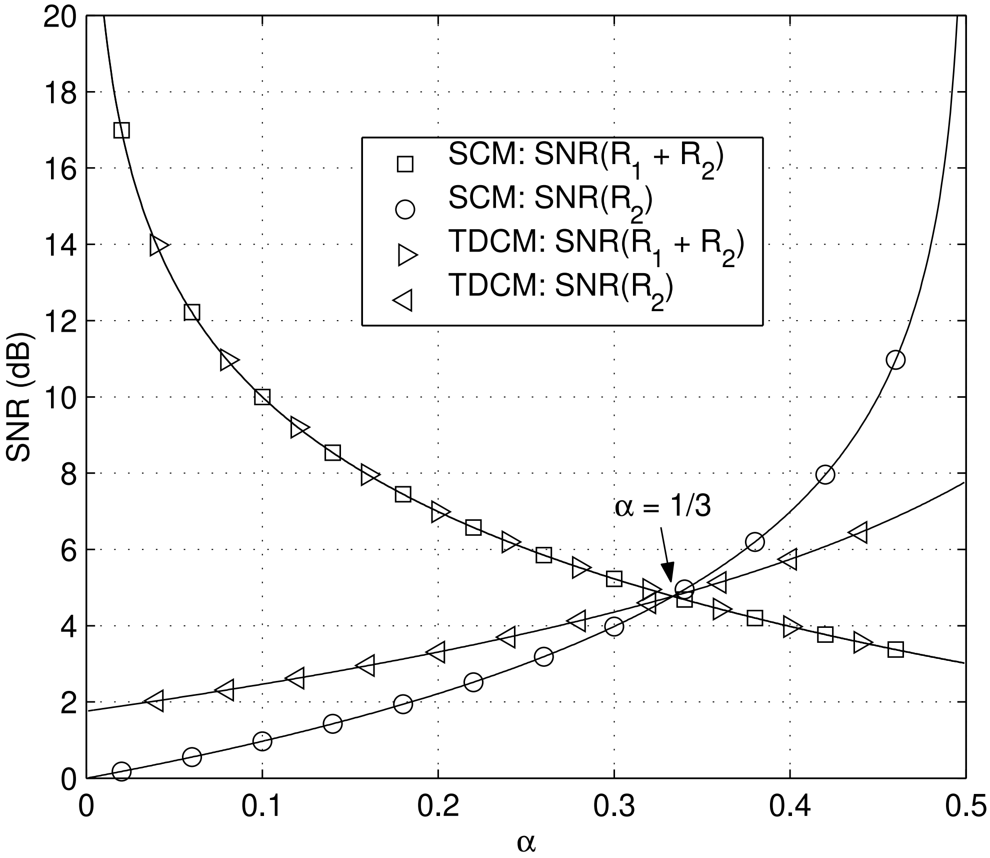

Figure 2.2: Comparison of Superposition Coded Modulation (SCM) and Time-Division Coded Modulation (TDCM).

The capacity region for the Gaussian broadcast channel, with signal power constraint P, is given by

$$R_1 < C(\frac{\alpha P}{N_1}) \tag{2.6}$$

$$R_2 < C(\frac{(1-\alpha)P}{\alpha P + N_2}) \quad \text{for } 0 \leq \alpha \leq 1 \tag{2.7}$$

This region is theoretically achieved by the superposition coding scheme described by Cover in [3]. Bergmans [4], [5] proved the converse. See also [6] for an excellent survey of broadcast channel information theory.

Figure 2.2 illustrates (2.6-2.7) for $R_1 = R_2 = 1$ by plotting the required SNRs for R_2 (circles) and $R_1 + R_2$ (squares) as a function of α. Since (2.6) assumes that the R_2 data has already been decoded, the plot is meaningful only when the $SNR(R_1 + R_2)$ curve lies above the $SNR(R_2)$ curve, i.e. for $\alpha < 1/3$.

Figure 2.2 shows how α controls the UEP tradeoff. As α decreases, the more important R_2 data can be received at lower and lower SNRs. However, this extra reliability of the R_2 data comes at the cost of decreased reliability for the less important R_1 data which requires a higher and higher SNRs as α decreases.

Figure 2.2 also shows the performance of an optimal time-division coded modulation (TDCM) scheme designed to match the $R_1 + R_2$ performance of SCM. As shown by the performance loss in the TDCM R_2 curve of Figure 2.2 as compared to the SCM R_2 curve, TDCM is theoretically inferior to superposition coded modulation (SCM). However, Wei [7] considered trellis-coded modulation (TCM) for UEP using both TDCM and SCM approaches, and found TDCM to be superior. Gadkari and Rose [8] explained this behavior by showing that TDCM outperforms SCM for some UEP regions when the channel code performance is sufficiently worse than the capacity-achieving performance assumed in

Figure 2.2. Recently, Wang and Orchard [9] carefully designed a TCM-based SCM scheme which incorporated shaping. This scheme does outperform TDCM in a UEP region of interest.

To encode the messages, the transmitter generates two codebooks, one with power αP at rate-R_1, and another codebook with power $(1-\alpha)P$ at rate-R_2, where R_1 and R_2 lie in the capacity region above. Then to send an index $i \in \{1, 2, \cdots, 2^{nR_1}\}$ and $j \in \{1, 2, \cdots, 2^{nR_2}\}$ to receivers with high SNR and receivers with low SNR, the transmitter takes the codeword $\mathbf{X}(i)$ from the first codebook and codeword $\mathbf{X}(j)$ from the second codebook and computes the sum. The transmitter sends the sum over the channel.

The receivers must now decode their messages. First consider a receiver with low SNR. The receiver merely looks through the second codebook to find the closest codeword to the received vector $\mathbf{Y_2}$. Its effective signal to noise ratio is $(1-\alpha)P/(\alpha P + N_2)$, since message at rate-$R_1$ acts as noise to Y_2.

A receiver with high SNR first decodes the codeword with rate-R_2, which it can accomplish because of its lower noise N_1. The receiver subtracts this codeword $\hat{\mathbf{X}}_\mathbf{2}$ from $\mathbf{Y_1}$, and the receiver then looks for the codeword in the first codebook closest to $\mathbf{Y_1} - \hat{\mathbf{X}}_\mathbf{2}$. The resulting probability of error can be made as low as desired [10].

In Claude E. Shannon's landmark paper "A Mathematical Theory of Communication" [11], the channel coding theorem establishes the existence of codes that can be used to transmit data through a channel at any rate less than the channel capacity with arbitrarily small probability of error [12, 13]. Nevertheless, there is no systematic way to design practical channel codes that meet the specifications of the coding theorem. Before the emergence of turbo codes in 1993, low complexity channel codes can only get within a few dBs of the Shannon bound. Turbo codes achieve near-Shannon-limit error correction performance with relatively simple constituent codes and a large interleaver [14].

In this chapter, we use turbo codes to design an SCM. Since turbo codes closely approximate capacity-achieving performance, it is not surprising that our SCM closely approaches the theoretical SCM curve in Figure 2.2. In all of our examples, the turbo coded SCM architecture at BER of 10^{-5} performs within 1 dB of the capacity region boundary of the degraded broadcast channel over the entire useful range of the power allocation parameter α.

We present two superposition turbo TCM schemes. One scheme uses the Fragouli and Wesel (F-W) based structure [15], while the other uses the Robertson and Wörz (R-W) based structure [16]. The performance of two schemes are within 0.8 dB and 0.9 dB respectively of constrained capacity at a BER of 10^{-5} for both high-SNR and low-SNR receivers with a standard 16-QAM constellation, which corresponds to $\alpha = 0.2$ in (2.6-2.7). We consider degraded broadcast channels with additive white Gaussian noise. In our schemes with a two-rate structure, low-SNR receivers only decode data with rate-R_2 (i.e. only 2-MSB of the 4-bit labeling of the 16-point square constellation), while high SNR receivers decode data with rate-$(R_1 + R_2)$, which means decoding all four bits of each 16-point square constellation symbol.

Section 2.2 discusses the power allocation parameter α in detail, and shows that when α takes a certain value, SCM reduces to multi-level coding as discussed in [17]. Section 2.3 presents the detail of our SCM turbo TCM architecture. Section 2.4 presents simulation results for two-rate SCMs using 8-point circular constellations and 16-point square constellations as well as a three-rate example using 64-QAM. Section 2.5 describes the structure and performance of a superposition turbo TCM utilizing Robertson and Wörz scheme. Section 3.5 concludes the chapter.

2.2 Reconfigurability of the Multi-rate Code Using α

The α in (2.6-2.7) controls the ratio of power allocation to the two data streams. For practical constellations, it decides the Euclidean distances between the constellation points. For a fixed-rate two-rate structure with $R_1 = R_2 = 1$, α can take a value from 0 to 0.5 according to (2.6-2.7). However, as seen in Figure 2.2 with two-stage decoding, only α's between 0 and 1/3 make sense.

By choosing α within this range, we configure the system supporting two groups of receivers with different pairs of error free SNR. When α equals 1/3, the two-rate structure becomes a single rate structure theoretically, since both rates are supported at the same SNR. It is essentially a multi-level code, and our two-stage decoding is actually the two-level multilevel code (MLC) decoding [17]. By choosing α within $(0, 1/3)$, we configure the system to support two rates with two corresponding operating SNRs.

2.2.1 Constellations

In Figure 2.3, the α in (2.6-2.7) can be easily determined to be 0.2 for standard 16-QAM which has equal Euclidean distance between adjacent constellation point. Solving (2.6-2.7) for the maximum N_1 and N_2 with $R_1 = R_2 = 1$ and $\alpha = 0.2$

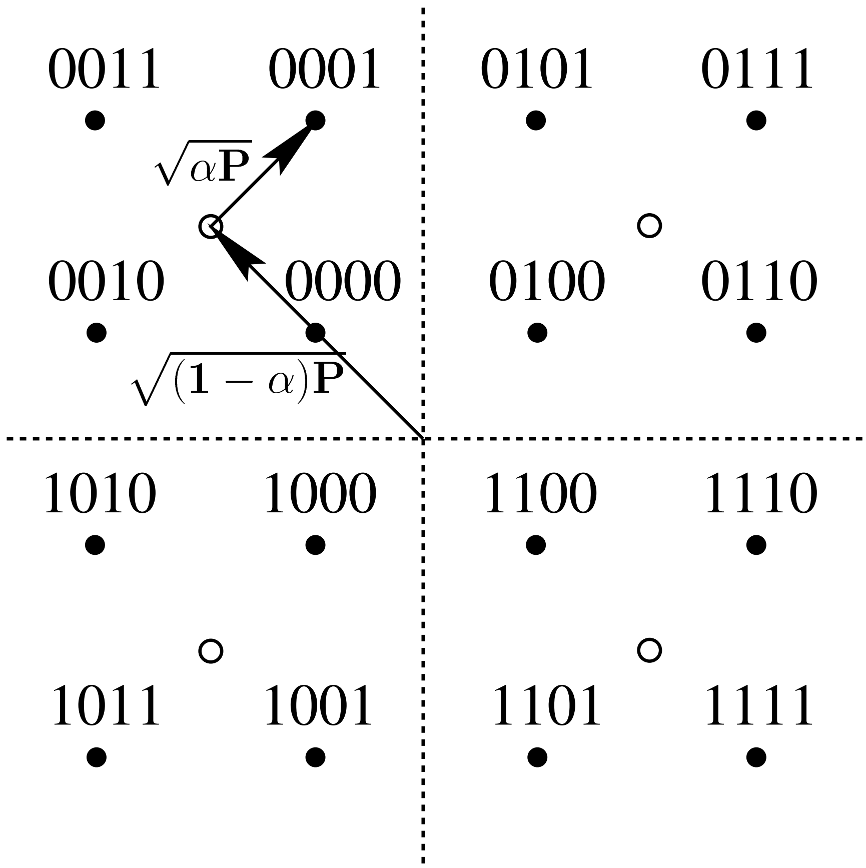

Figure 2.3: Labeling for the 16-QAM Constellation used in Simulations, $\alpha = 0.2$.

yields $N_1 = 0.2P$ and $N_2 = 0.6P$. respectively. Additionally, incorporating the constraint to 16-QAM signaling reduces the tolerable noise to $N_1 = 0.1917P$ and $N_2 = 0.5651P$ respectively. As a result, the error free SNRs are 7.0 dB and 2.2 dB as shown in Figure 2.2. The transmitted signal and the noise in Figure 2.2 are both assumed to have Gaussian distributions.

Figure 2.4 shows the 16-point square constellations resulting from $\alpha = 0.1$ and $\alpha = 0.3$. Figure 2.3-2.4 also illustrate the edge profile optimal constellation labeling [18] of the 16-point square constellation in simulation for $\alpha = 0.1$ and

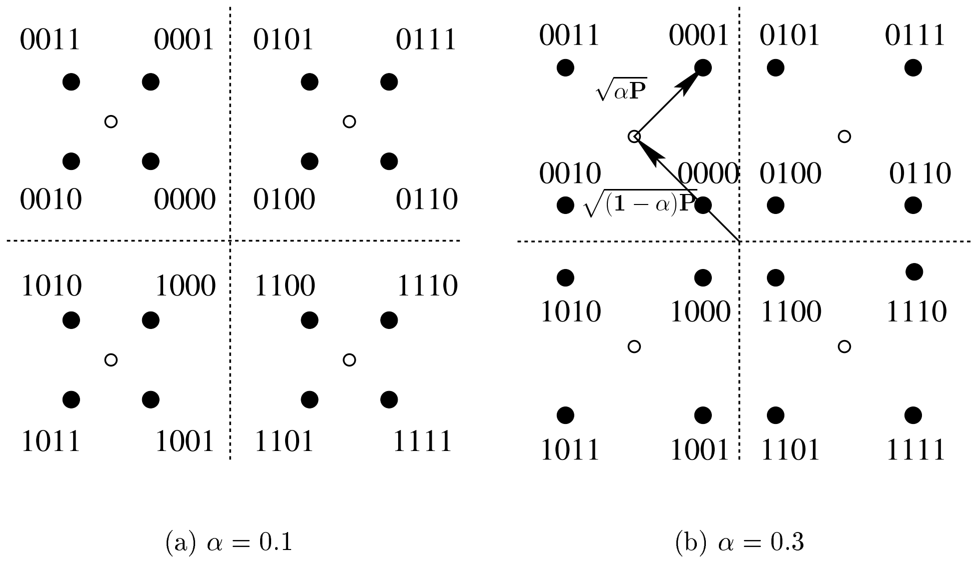

Figure 2.4: Example for constellations used in simulation for $\alpha = 0.1$, $\alpha = 0.3$.

$\alpha = 0.3$. It can be seen that the two most significant bits (MSBs) labeling the four constellation points in the same quadrant are identical.

Figure 2.4(b) also shows how α allocates power. For the 16-point square constellation in Figure 2.4(b), the 16-point square constellation can be considered as one QPSK constellation added to another QPSK constellation. Two bits of rate-R_2 data are modulated as a QPSK signal which can be mapped to one of four "empty dots" with amplitude of $\sqrt{(1-\alpha)P}$. Then, two bits of rate-R_1 data are modulated as another QPSK signal which can be represented by a solid dot with amplitude of $\sqrt{\alpha P}$, using one of four "empty dots" as its origin.

It can be seen that α allocates the power similarly for 64-QAM and for an 8-point circular constellation in Figure 2.8 and Figure 2.5 respectively. Figure 2.8 is the example of a 64-point square constellation with $\alpha_1 = 1/21$, $\alpha_2 = 4/21$ (standard 64-QAM), where α_1 and α_2 are the power allocation parameters in

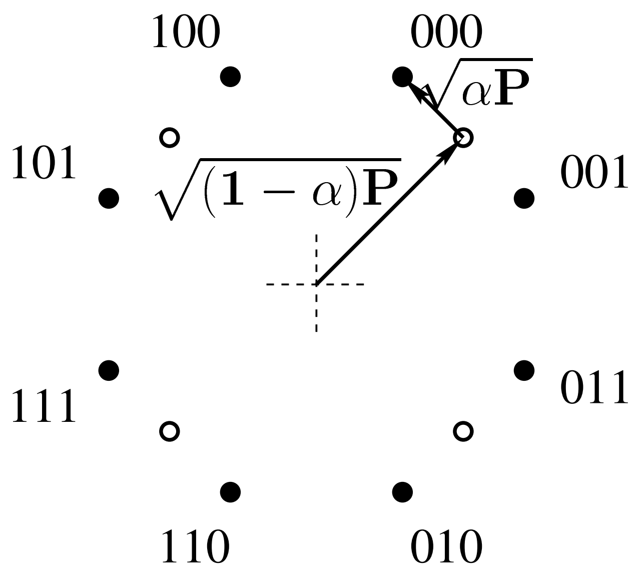

Figure 2.5: Labeling for the 8-point Circular Constellations Used in Simulation ($\alpha = 0.1464$).

(2.8-2.9).

Figure 2.5 is the example of the 8-point circular constellations with $\alpha = 0.1464$ (standard 8-PSK). An 8-point circular constellation can be considered as the superposition of a BPSK constellation on top of a QPSK constellation.

2.2.2 Multi-level Coding

The following theorem shows that the MLC coding scheme is a special case of multi-rate degraded broadcast channel when all receivers have the same error free SNR. Hence, it is likely we can tune a good MLC code into a good degraded broadcast channel code, or vice versa.

Theorem 1 *Consider the Gaussian broadcast channel with one sender and k receivers, $k \geq 1$, we have $Y_i = X + Z_i$, where $Z_i \sim \mathcal{N}(0, N_i)$*

$$R_1 < C(\frac{\alpha_1 P}{N_1}), \cdots, \quad (2.8)$$

$$R_i < C(\frac{\alpha_i P}{\sum_{j=1}^{i-1} \alpha_j P + N_i}), \cdots \quad (2.9)$$

where $1 \leq i \leq k$, *and* $\sum_{i=1}^{k} \alpha_i = 1$.

if $N_1 = N_2 = \cdots = N$, *then, the rate region reduces to*

$$\sum_{i=1}^{k} R_i < C(\frac{P}{N}). \quad (2.10)$$

Proof: Sum $R_1, \cdots, R_N$ with $N_i = N$. □

This theorem explains why our multi-rate superposition turbo TCM schemes, when configured for single rate, can perform as well as the typical single rate turbo TCM in simulation. If $N_i = N$ and the rates have been fixed to satisfy (2.10), (2.8-2.9) can always be solved for $\alpha_1, \cdots, \alpha_k$. So a good single rate code may be obtained from a good multi-rate code as a special case.

2.3 The Superposition Turbo TCM

For our SCM architecture, we use the symbol-interleaved parallel-concatenated turbo TCM (PCTCM) structure of Fragouli and Wesel [19, 15]. The bit-interleaved turbo TCM scheme of Benedetto, Divsalar, and Montorsi [20] is a possible alternative, but bit-interleaving further complicates the initial and subsequent soft information computations required to support multiple rates. We also implemented SCM using the symbol-interleaved turbo TCM structure of Robertson and Wörz [16], and found its performance to be quite similar, about 0.1 dB worse than SCM based on the Fragouli and Wesel symbol-interleaved architecture.

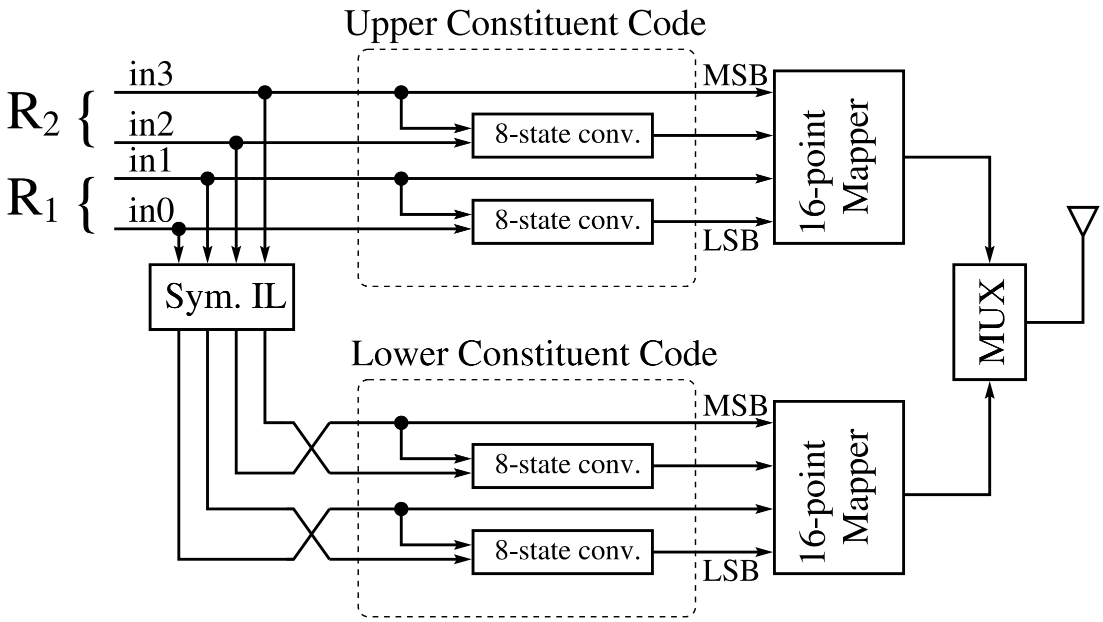

Figure 2.6: PCTCM Superposition Turbo TCM Encoder for Two Rates and a 16-point Square Constellation.

2.3.1 Encoder

Figure 2.6 shows the superposition turbo encoder based on the structure of [19, 15] for the family of 16-point square constellations, for which examples are illustrated in Figure 2.3-2.4.

It is a parallel concatenated trellis-coded modulation (PCTCM) with constituent encoder of rate-4/4. In fact, the constituent code consists of two identical recursive convolutional codes of rate-2/2. The rate-2/2 recursive convolutional encoder may be considered as a rate-2/3 recursive convolutional encoder with one systematic bit punctured.

The upper rate-4/4 constituent encoder has as systematic outputs the two input MSBs while the lower rate-4/4 constituent encoder has as systematic outputs the two least significant input bits (LSBs). Thus the systematic bits are evenly divided between the constituent encoders, and the overall turbo code cannot be catastrophic.

Figure 2.3 illustrates the edge profile optimal constellation labelings [18] of the 16-QAM modulation in use. It can be seen that the 2 MSBs of four constellation labelings in the same quadrant are identical.

The rate-2/2 8-state recursive convolutional encoder within the constituent encoders is obtained through exhaustive computer search, and optimized for normalized d_{s2}^{E}, where d_{s2}^{E} represents effective free distance. The superscript E refers to the output squared Euclidean distance, and the subscript $s2$ denotes that the symbol-wise input weight is two. It was proved [21] that the lowest d_{s2}^{E} error event is a dominant factor in performance. The interleaver gain is proportional to $N^{1-w_{min}}$, where N is the interleaver length, and w_{min} is the minimum weight in any finite-weight error event. It is easy to see that w_{min} is equal to 2 for all recursive convolutional encoders. Thus, the interleaver gain is proportional to $1/N$.

The exhaustive code search uses a forward trellis search, maximizing the Euclidean distance for two input symbol errors for given constellation. Among the codes searched, the one with the lowest number of nearest neighbor is selected. For the 16-QAM constellation in use, since class 0 has smallest squared Euclidean distance for each edge label among all four classes [22], the Euclidean distance between the test path and all zero state path determines the search result.

According to Fragouli [15] and Divsalar [23], an upper bound on effective free distance for a convolutional encoder with multiple “disconnected” shift registers is constrained by the minimum length shift register. Thus, the number of memory of two convolutional encoders in the same constituent code should be the same. We found a good constituent code with identical rate-2/2 recursive convolutional encoders for the two input MSBs and for the two input LSBs.

The 8-state recursive convolutional code we found by optimizing for normalized d_{s2}^E is

$$A = \begin{bmatrix} 0 & 1 & 0 \\ 0 & 0 & 1 \\ 1 & 1 & 0 \end{bmatrix}, \tag{2.11}$$

$$B = \begin{bmatrix} 0 & 0 & 1 \\ 0 & 1 & 1 \end{bmatrix}, \tag{2.12}$$

$$C = \begin{bmatrix} 1 & 0 \\ 0 & 0 \\ 1 & 0 \end{bmatrix}, \tag{2.13}$$

$$D = \begin{bmatrix} 1 & 0 \\ 0 & 1 \end{bmatrix}. \tag{2.14}$$

in the encoder state-space description:

$$[s_1\, s_2\, s_3]_{j+1} = [s_1\, s_2\, s_3]_j \cdot A + [u_1\, u_2]_j \cdot B \tag{2.15}$$

$$[y_1\, y_2]_j = [s_1\, s_2\, s_3]_j \cdot C + [u_1\, u_2]_j \cdot D \tag{2.16}$$

where s_i is the state vector, u_i is the input vector, and y_i is the output vector.

Matrix A is the companion matrix of the encoder's feedback polynomial [15]. Only primitive feedback polynomials are considered in the exhaustive code search. The state-space description is very general, since it can describe the constituent code with multiple rows of memory. It is also easy to implement in simulation.

The state-space description of the 64-state upper constituent code for 16-QAM is as follows:

$$A = \begin{bmatrix} 0 & 1 & 0 & 0 & 0 & 0 \\ 0 & 0 & 1 & 0 & 0 & 0 \\ 1 & 1 & 0 & 0 & 0 & 0 \\ 0 & 0 & 0 & 0 & 1 & 0 \\ 0 & 0 & 0 & 0 & 0 & 1 \\ 0 & 0 & 0 & 1 & 1 & 0 \end{bmatrix}, \tag{2.17}$$

$$B = \begin{bmatrix} 0 & 0 & 1 & 0 & 0 & 0 \\ 0 & 1 & 1 & 0 & 0 & 0 \\ 0 & 0 & 0 & 0 & 0 & 1 \\ 0 & 0 & 0 & 0 & 1 & 1 \end{bmatrix}, \tag{2.18}$$

$$C = \begin{bmatrix} 1 & 0 & 0 & 0 \\ 0 & 0 & 0 & 0 \\ 1 & 0 & 0 & 0 \\ 0 & 0 & 1 & 0 \\ 0 & 0 & 0 & 0 \\ 0 & 0 & 1 & 0 \end{bmatrix}, \tag{2.19}$$

$$D = \begin{bmatrix} 1 & 0 & 0 & 0 \\ 0 & 1 & 0 & 0 \\ 0 & 0 & 1 & 0 \\ 0 & 0 & 0 & 1 \end{bmatrix}. \tag{2.20}$$

And, the state-space description of the 64-state lower constituent code for 16-QAM is as follows:

$$A = \begin{bmatrix} 0 & 1 & 0 & 0 & 0 & 0 \\ 0 & 0 & 1 & 0 & 0 & 0 \\ 1 & 1 & 0 & 0 & 0 & 0 \\ 0 & 0 & 0 & 0 & 1 & 0 \\ 0 & 0 & 0 & 0 & 0 & 1 \\ 0 & 0 & 0 & 1 & 1 & 0 \end{bmatrix}, \tag{2.21}$$

$$B = \begin{bmatrix} 0 & 1 & 1 & 0 & 0 & 0 \\ 0 & 0 & 1 & 0 & 0 & 0 \\ 0 & 0 & 0 & 0 & 1 & 1 \\ 0 & 0 & 0 & 0 & 0 & 1 \end{bmatrix}, \tag{2.22}$$

$$C = \begin{bmatrix} 1 & 0 & 0 & 0 \\ 0 & 0 & 0 & 0 \\ 1 & 0 & 0 & 0 \\ 0 & 0 & 1 & 0 \\ 0 & 0 & 0 & 0 \\ 0 & 0 & 1 & 0 \end{bmatrix}, \tag{2.23}$$

$$D = \begin{bmatrix} 0 & 1 & 0 & 0 \\ 1 & 0 & 0 & 0 \\ 0 & 0 & 0 & 1 \\ 0 & 0 & 1 & 0 \end{bmatrix}. \tag{2.24}$$

We applied an extended spread symbol interleaver [19] to the above constituent code. The extended spread symbol interleaver is a semi-random interleaver due to the random selection without replacement of N integers from 1 to N under certain constraints.

In Figure 2.7, we present the superposition turbo TCM encoder for the family of 64-point square constellations. The same rate-2/2, 8-state, recursive convolutional code of the superposition encoder for 16-point square constellations is used as the sub-code of the constituent code. The encoder for the 64-point square constellation is the direct extension of that for the 16-point square constellation in Figure 2.6. Three levels of superposition are used for this structure. Three QPSK data streams are summed together to generate the transmitted data stream. The performance is within 0.9 dB of constrained capacity for all three SNR ranges. Further discussion of the simulation can be found in Section 2.4.

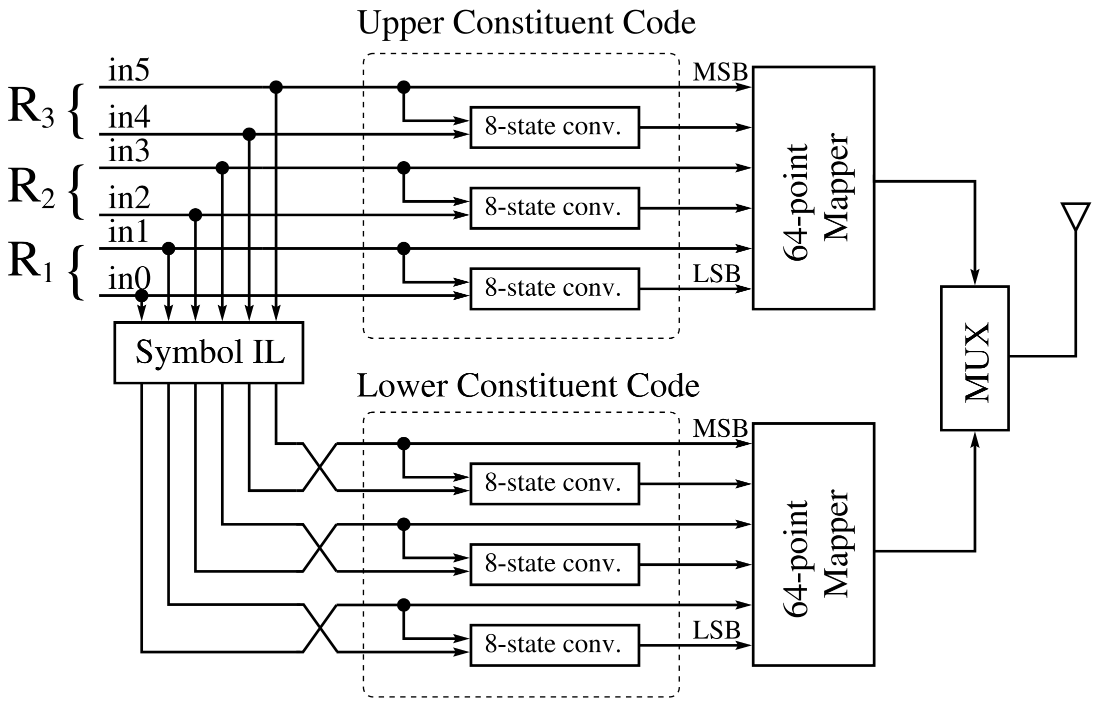

Figure 2.7: PCTCM Superposition Turbo TCM Encoder for Three Rates and a 64-point Square Constellation.

Figure 2.8 shows the standard Gray labeled 64-QAM constellation used in simulation.

Figure 2.9 shows the superposition turbo TCM encoder for for 8-point circular constellation. Two levels of superposition are used for this structure. A BPSK data stream (i.e. the LSB) is added on top of a QPSK data stream. Since we use rate-1/2 code for the LSB, we encode two 8-point circular constellation symbols at the same time. The rate-2/2, 8-state, recursive convolutional code described by (2.11-2.16) is also used for each sub-code of the constituent code for the 8-point circular constellation encoder.

The state-space description of the 512-state bi-8-PSK upper constituent code

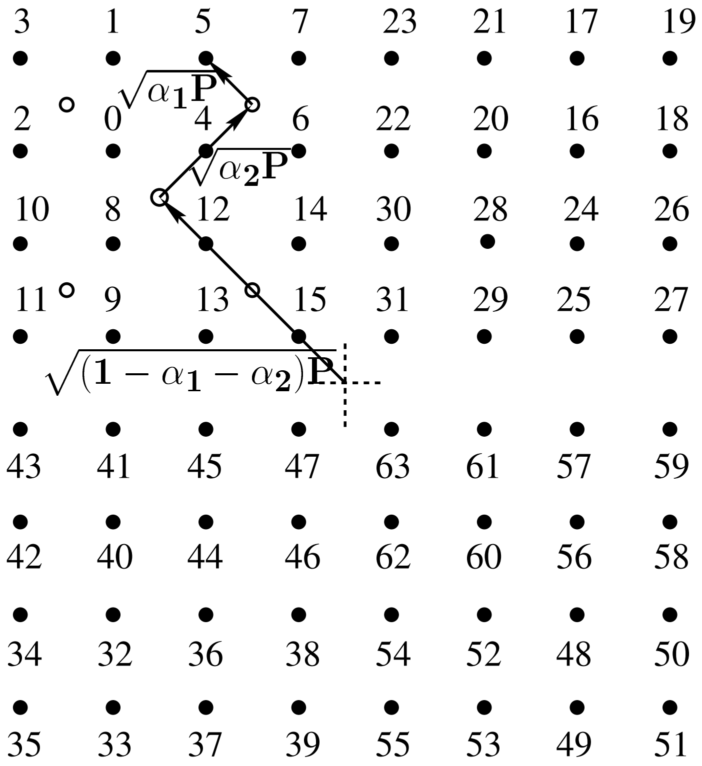

Figure 2.8: Labeling for the 64-QAM Constellations used in Simulations ($\alpha_1 = 1/21$, $\alpha_2 = 4/21$).

is as follows:

$$A = \begin{bmatrix} 0 & 1 & 0 & 0 & 0 & 0 & 0 & 0 & 0 \\ 0 & 0 & 1 & 0 & 0 & 0 & 0 & 0 & 0 \\ 1 & 1 & 0 & 0 & 0 & 0 & 0 & 0 & 0 \\ 0 & 0 & 0 & 0 & 1 & 0 & 0 & 0 & 0 \\ 0 & 0 & 0 & 0 & 0 & 1 & 0 & 0 & 0 \\ 0 & 0 & 0 & 1 & 1 & 0 & 0 & 0 & 0 \\ 0 & 0 & 0 & 0 & 0 & 0 & 0 & 1 & 0 \\ 0 & 0 & 0 & 0 & 0 & 0 & 0 & 0 & 1 \\ 0 & 0 & 0 & 0 & 0 & 0 & 1 & 1 & 0 \end{bmatrix}, \tag{2.25}$$

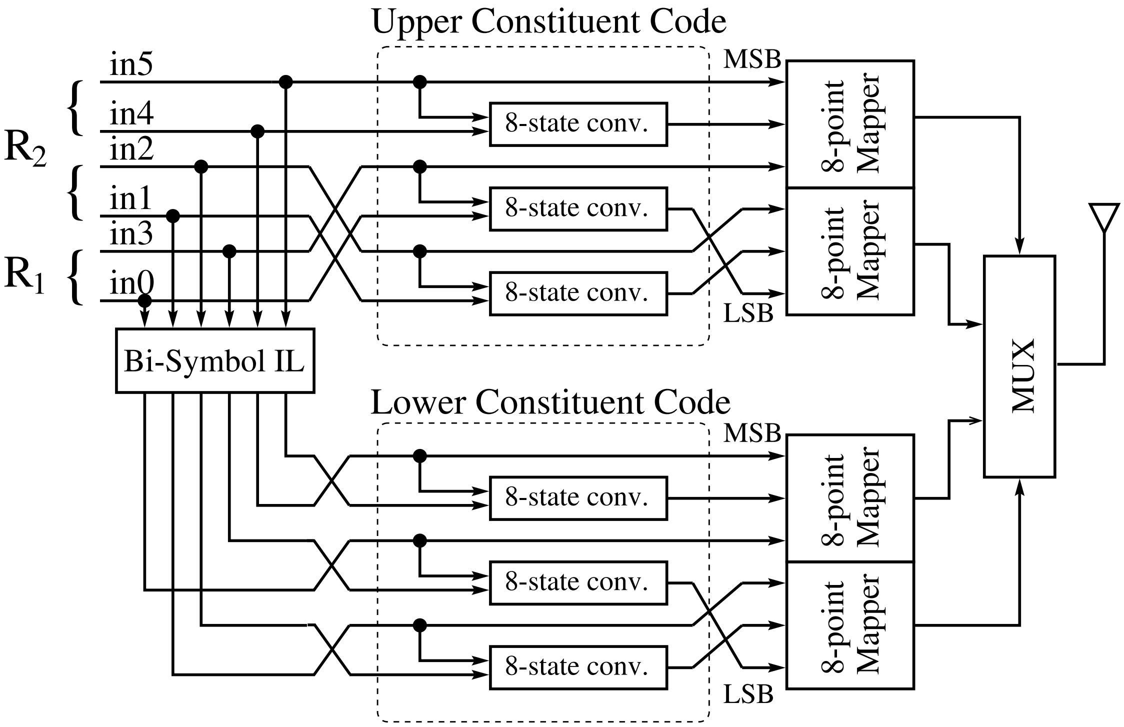

Figure 2.9: PCTCM Superposition Turbo TCM Encoder for Two Rates and a 8-point Circular Constellation

$$B = \begin{bmatrix} 0 & 0 & 0 & 0 & 0 & 1 & 0 & 0 & 0 \\ 0 & 0 & 1 & 0 & 0 & 0 & 0 & 0 & 0 \\ 0 & 1 & 1 & 0 & 0 & 0 & 0 & 0 & 0 \\ 0 & 0 & 0 & 0 & 1 & 1 & 0 & 0 & 0 \\ 0 & 0 & 0 & 0 & 0 & 0 & 0 & 0 & 1 \\ 0 & 0 & 0 & 0 & 0 & 0 & 0 & 1 & 1 \end{bmatrix}, \tag{2.26}$$

$$C = \begin{bmatrix} 0 & 1 & 0 & 0 \\ 0 & 0 & 0 & 0 \\ 0 & 1 & 0 & 0 \\ 1 & 0 & 0 & 0 \\ 0 & 0 & 0 & 0 \\ 1 & 0 & 0 & 0 \\ 0 & 0 & 1 & 0 \\ 0 & 0 & 0 & 0 \\ 0 & 0 & 1 & 0 \end{bmatrix}, \tag{2.27}$$

$$D = \begin{bmatrix} 1 & 0 & 0 & 0 & 0 & 0 \\ 0 & 1 & 0 & 0 & 0 & 0 \\ 0 & 0 & 1 & 0 & 0 & 0 \\ 0 & 0 & 0 & 1 & 0 & 0 \\ 0 & 0 & 0 & 0 & 1 & 0 \\ 0 & 0 & 0 & 0 & 0 & 1 \end{bmatrix}. \tag{2.28}$$

And, the state-space description of the 512-state bi-8-PSK lower constituent code is as follows:

$$A = \begin{bmatrix} 0 & 1 & 0 & 0 & 0 & 0 & 0 & 0 & 0 \\ 0 & 0 & 1 & 0 & 0 & 0 & 0 & 0 & 0 \\ 1 & 1 & 0 & 0 & 0 & 0 & 0 & 0 & 0 \\ 0 & 0 & 0 & 0 & 1 & 0 & 0 & 0 & 0 \\ 0 & 0 & 0 & 0 & 0 & 1 & 0 & 0 & 0 \\ 0 & 0 & 0 & 1 & 1 & 0 & 0 & 0 & 0 \\ 0 & 0 & 0 & 0 & 0 & 0 & 0 & 1 & 0 \\ 0 & 0 & 0 & 0 & 0 & 0 & 0 & 0 & 1 \\ 0 & 0 & 0 & 0 & 0 & 0 & 1 & 1 & 0 \end{bmatrix}, \tag{2.29}$$

$$B = \begin{bmatrix} 0 & 0 & 0 & 0 & 1 & 1 & 0 & 0 & 0 \\ 0 & 1 & 1 & 0 & 0 & 0 & 0 & 0 & 0 \\ 0 & 0 & 1 & 0 & 0 & 0 & 0 & 0 & 0 \\ 0 & 0 & 0 & 0 & 0 & 1 & 0 & 0 & 0 \\ 0 & 0 & 0 & 0 & 0 & 0 & 0 & 1 & 1 \\ 0 & 0 & 0 & 0 & 0 & 0 & 0 & 0 & 1 \end{bmatrix}, \tag{2.30}$$

$$C = \begin{bmatrix} 0 & 1 & 0 & 0 \\ 0 & 0 & 0 & 0 \\ 0 & 1 & 0 & 0 \\ 1 & 0 & 0 & 0 \\ 0 & 0 & 0 & 0 \\ 1 & 0 & 0 & 0 \\ 0 & 0 & 1 & 0 \\ 0 & 0 & 0 & 0 \\ 0 & 0 & 1 & 0 \end{bmatrix}, \tag{2.31}$$

$$D = \begin{bmatrix} 0 & 0 & 0 & 1 & 0 & 0 \\ 0 & 0 & 1 & 0 & 0 & 0 \\ 0 & 1 & 0 & 0 & 0 & 0 \\ 1 & 0 & 0 & 0 & 0 & 0 \\ 0 & 0 & 0 & 0 & 0 & 1 \\ 0 & 0 & 0 & 0 & 1 & 0 \end{bmatrix}. \tag{2.32}$$

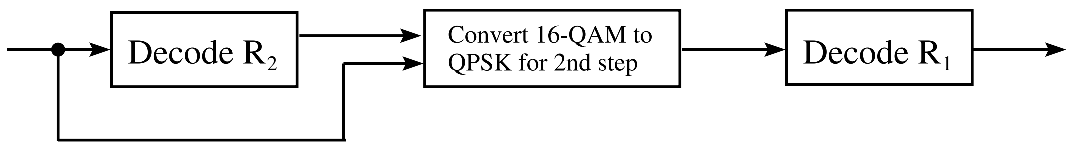

Figure 2.10: PCTCM Superposition Turbo TCM Decoder (high level)

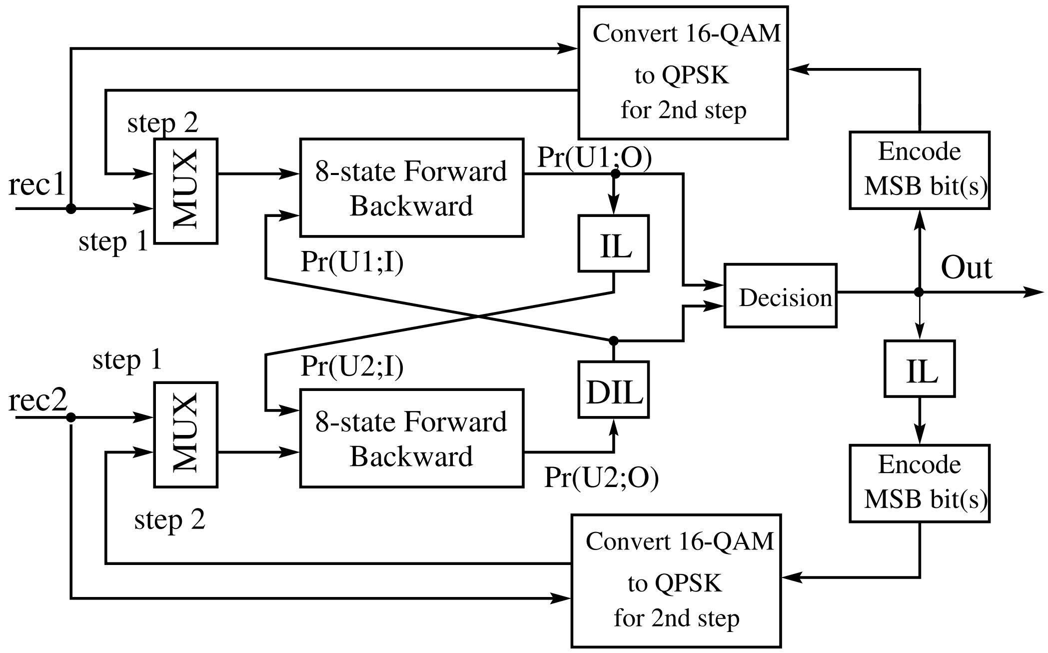

Figure 2.11: PCTCM Superposition Turbo TCM Decoder

2.3.2 Decoder

We use two-stage decoding for the two-rate encoder of Figure 2.6 with a SISO decoder as in Figure 2.10 and Figure 2.11. Figure 2.10 is the high level block diagram of the decoder, and Figure 2.11 shows the detailed data flow of the decoder for implementation. It is similar to the "onion peeling" algorithm in

[24].

The first decoding stage decodes the two input MSBs. It uses an 8-state-trellis, and calculates the metric by summing up the squared Euclidean distance between the received symbol and all four constellation points of the same quadrant.

Before starting the second decoding stage, the received 16-point square constellation symbols are converted to QPSK symbols. The first decoding stage essentially selects a quadrant of the 16-point square constellation. The received value is then shifted and possibly reflected about the X or Y axis to produce a noise-distorted point from a QPSK constellation whose labeling is the same regardless of the originating quadrant.

The second decoding stage decodes two input LSBs by decoding the resulting QPSK symbols. The block diagram of the multi-stage-decoding decoders for the three-rate encoder using a 64-point square constellation and the two-rate encoder using a 8-point circular constellation are similar to that for 16-point square constellation in Figure 2.11. We use a three-stage decoding algorithm for the three-rate decoder, and a two-stage algorithm for the two-rate decoders.

Generally, with the constituent code consisting of multiple independent codes, joint decoding outperforms separately decoding the multiple codes. But, in the degraded broadcast channel, two-stage decoding has essentially the same performance as that of joint decoding. Moreover, the complexity of the jointly decoding algorithm is sixteen times that of the two-stage decoding scheme.

For receivers with high SNR, the two input MSBs are effectively error free. Joint decoding with a 64-state-trellis performs the same as two-stage decoding with 8-state trellises.

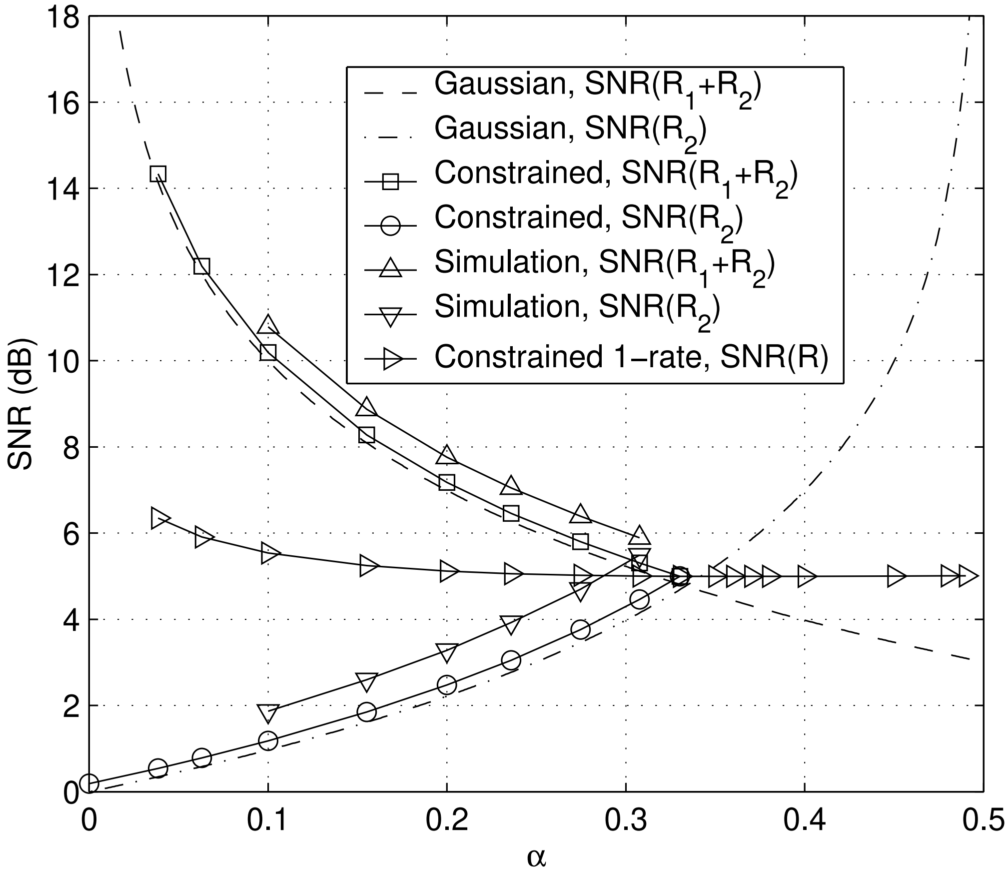

Figure 2.12: SNR required for error-free theoretical performance and simulated performance with $BER = 10^{-5}$ for high rate and low rate Rx vs. α; IL = 8,192; number of iter. = 15; $R_1 = R_2 = 1$ (bit/s/Hz); 16-point square constellation.

For receivers with low SNR, only the first stage of two-stage decoding is conducted. By summing up the squared Euclidean distance between the received symbol and all four constellation points belonging to the same quadrant as the metric, the first decoding stage in fact performs joint decoding of the two MSBs of the 16-QAM symbol.

2.4 Simulation Results

This section discusses simulation results for two-rate and three-rate superposition turbo-TCM structures with a 16-point square constellation, an 8-point circular constellation and 64-QAM.

The simulation results for the Robertson-Wörz structure are in Section 2.5.

The interleavers used in the simulations are semi-random interleavers [19]. To describe an interleaver we give the constraint parameters in the following order: (S, T, X), where $S_1 = S_2 = S$, $T_1 = T_2 = T$, and $X_1 = X_2 = X$.

2.4.1 Two-Rate Superposition with a 16-point Square Constellation

Figure 2.12 shows the performance as SNR required for $BER = 10^{-5}$ vs. α for two-rate encoder using a 16-point square constellation. The symbol interleaver has design parameters $(S = 54, T = 6, X = 1)$ and length 8,192. The constituent code (2.11-2.16) was optimized for the 16-QAM (i.e. $\alpha = 0.2$). But, it works fine with other α's. For the various α's from 0.1 to 0.3077 that we simulated, the high-SNR performance is within 0.6 dB of constrained capacity at BER of 10^{-5}, while the low-SNR performance increases from 0.7 dB (at $\alpha = 0.1$) to 1 dB (at

$\alpha = 0.3$) away from constrained capacity at BER of 10^{-5}.

The first two curves listed in the legend of Figure 2.12 are theoretical results from (2.6-2.7) with fixed rates $R_1 = R_2 = 1$. Both the transmitted signal and noise are assumed to be Gaussian for these two curves. The third and fourth curves are numerically calculated constrained capacities, in which the noise is still Gaussian, but the transmitted signals are 16 equi-probable constellation points placed according to α. Incorporating the constraint into standard 16-QAM signaling [25] reduces the tolerable noise to $N_1 = 0.1917P$ and $N_2 = 0.5651P$ respectively. As a result, the error free SNRs are 7.2 dB and 2.5 dB for standard 16-QAM ($\alpha = 0.2$). This represents loss of 0.2 dB and 0.3 dB respectively from the performance of Gaussian signaling. Curves five and six are the simulation results with various α. The last curve is the numerically calculated constrained capacity for single rate scheme using the 16 constellation points associated with a particular α.

Taking into account that the transmitted signal is not Gaussian, when $\alpha = 0.33015$ (instead of 1/3), the two-rate and the single rate schemes should theoretically perform the same.

Our simulation results for an α of 0.3077 are as good as that of typical single rate TCM with α of 0.2 [19], [16]. The constituent code searched was optimized for the standard 16-QAM (i.e. $\alpha = 0.2$). However, it turns out to be very robust for other αs. The theoretical performance of the single rate scheme is not sensitive to the change of α for $\alpha \geq 0.2$ as shown in last curve in Figure 2.12.

Choosing α to be smaller than 0.33015 for the 16-point, two-rate scheme, we will have unequal error protection [26]. There is a trade-off in picking the parameter α. To lower the operating SNR for the data stream of R_2, one must pay the price of a higher operating SNR for the data stream of $R_1 + R_2$.

Figure 2.13 and Figure 2.14 show the performance as BER vs SNR for different interleaver lengths at high and low SNR. At $BER = 10^{-5}$, the difference between interleaver lengths of 8,192 and 4,096 is about 0.1 to 0.15 dB, and the difference between interleaver lengths of 4,096 and 2,048 is about 0.2 dB.

Figure 2.15 and Figure 2.16 show the performance degradation when the number of iterations for SISO decoding decreases. There is about 0.05 dB difference between 15 iterations and 11 iterations at $BER = 10^{-5}$. Interleaver length is 8,192.

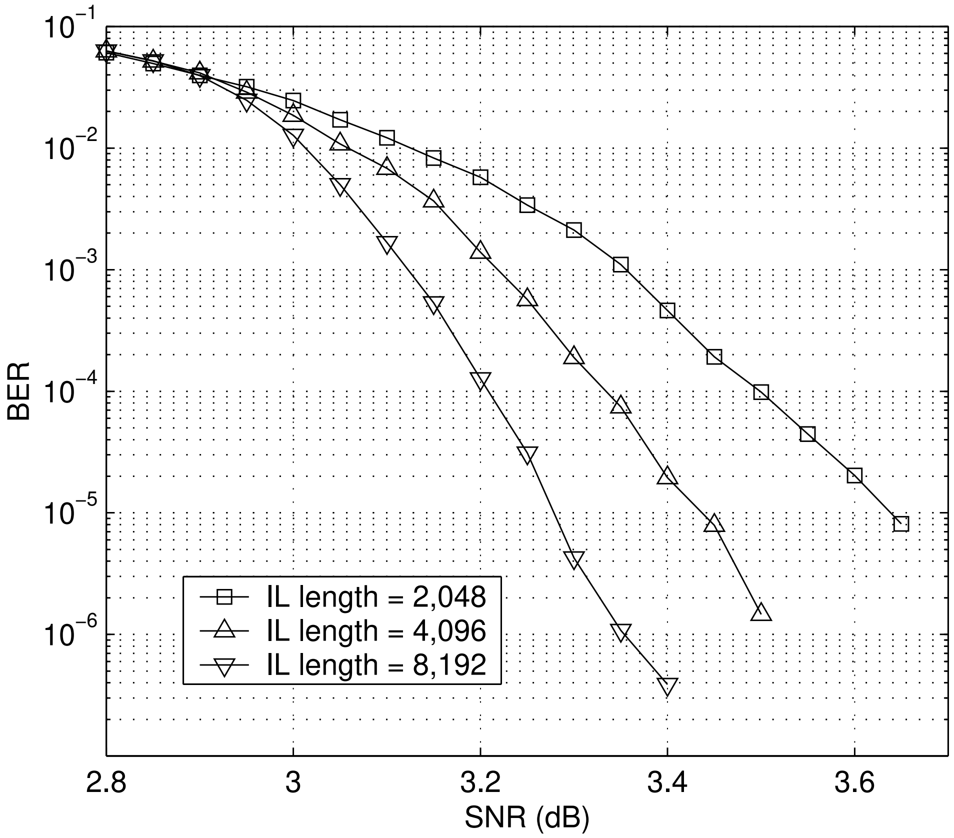

Figure 2.13: BER vs. SNR at low SNR range; $\alpha = 0.2$; number of iteration = 15; $R_1 = R_2 = 1$ (bit/s/Hz); 16-QAM

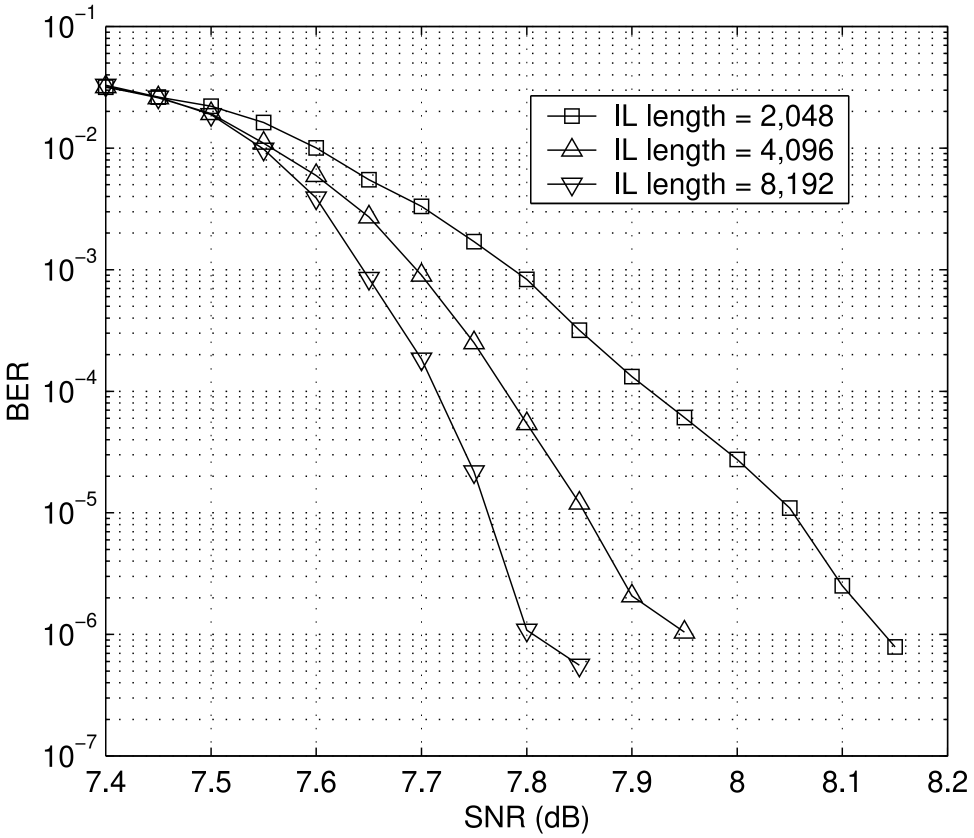

Figure 2.14: BER vs. SNR at high SNR range; $\alpha = 0.2$; number of iteration = 15; $R_1 = R_2 = 1$ (bit/s/Hz); 16-QAM

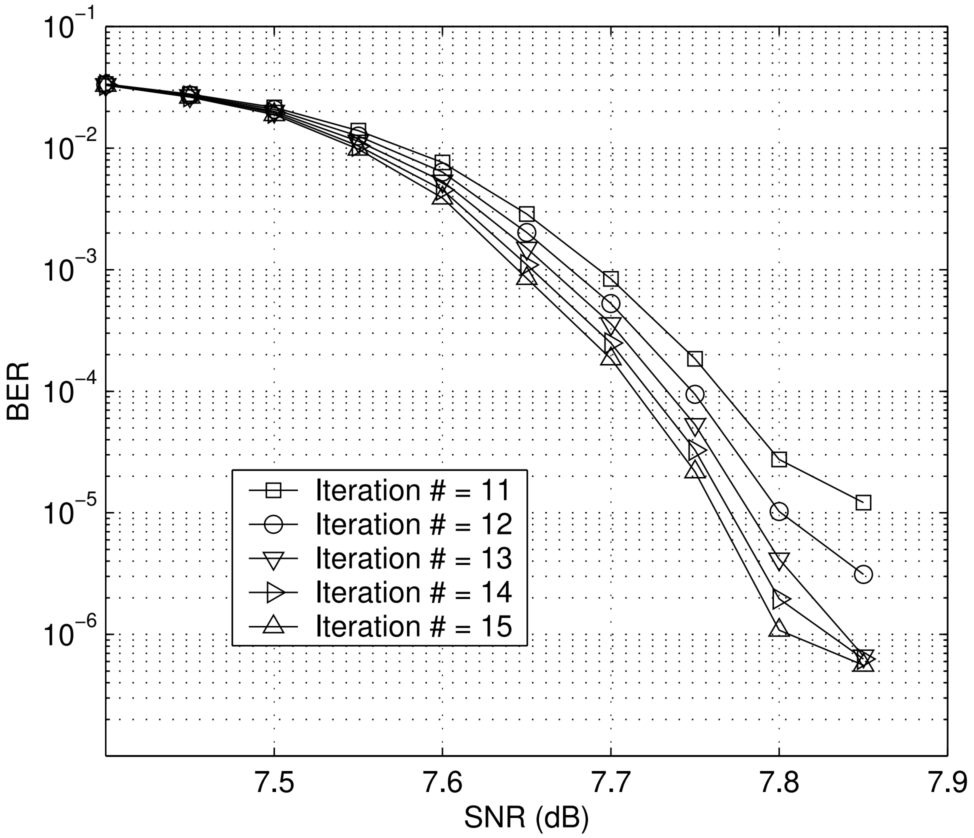

Figure 2.15: BER vs. SNR at high SNR range; $\alpha = 0.2$; IL = 8,192; number of iteration = 15; $R_1 = R_2 = 1$ (bit/s/Hz); 16-QAM

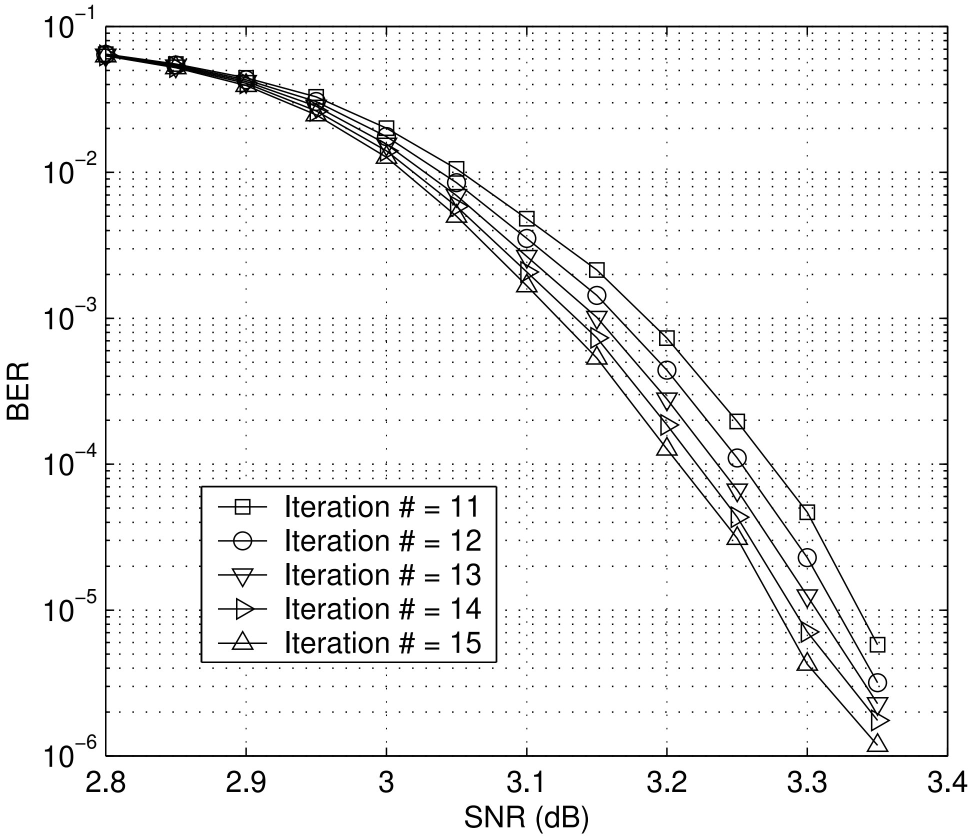

Figure 2.16: BER vs. SNR at low SNR range; $\alpha = 0.2$; IL = 8,192; number of iteration = 15; $R_1 = R_2 = 1$ (bit/s/Hz); 16-QAM

2.4.2 Two-Rate Superposition with an 8-point Circular Constellation

Figure 2.17 shows the performance as SNR required for $BER = 10^{-5}$ vs. α for a two-rate structure using an 8-point circular constellation ($R_1 = 0.5, R_2 = 1$). The theoretical range for α is from 0 to $\frac{\sqrt{2}-1}{2\sqrt{2}-1}$ (i.e. 0.2265), under the assumption that both the transmitted signal and the noise have Gaussian distributions. Including the performance-loss due to an 8-point circular signaling constellation, the practical range of α is around 0 to 0.25. For the various α's from 0.0794 to 0.2438 that we simulated, the SNR is within 0.7 dB of constrained capacity at BER of 10^{-5}. The symbol interleaver has design parameter ($S = 54, T = 6, X = 1$) and length 8,192. At high SNR and low SNR, the performance is within 0.6 dB and 0.7 dB of constrained capacity respectively, at BER of 10^{-5}.

Figure 2.18 and Figure 2.19 show BER vs SNR for different interleaver lengths at high SNR and low SNR. At $BER = 10^{-5}$, the difference between interleaver lengths of 8,192 and 4,096 is about 0.1 to 0.15 dB, and the difference between interleaver lengths of 4,096 and 2,048 is about 0.2 dB.

Figure 2.20 and Figure 2.21 show the performance degradation when the number of iterations for SISO decoding decreases. There is about 0.05 dB difference between 15 iterations and 11 iterations at $BER = 10^{-5}$. Interleaver length is 8,192.

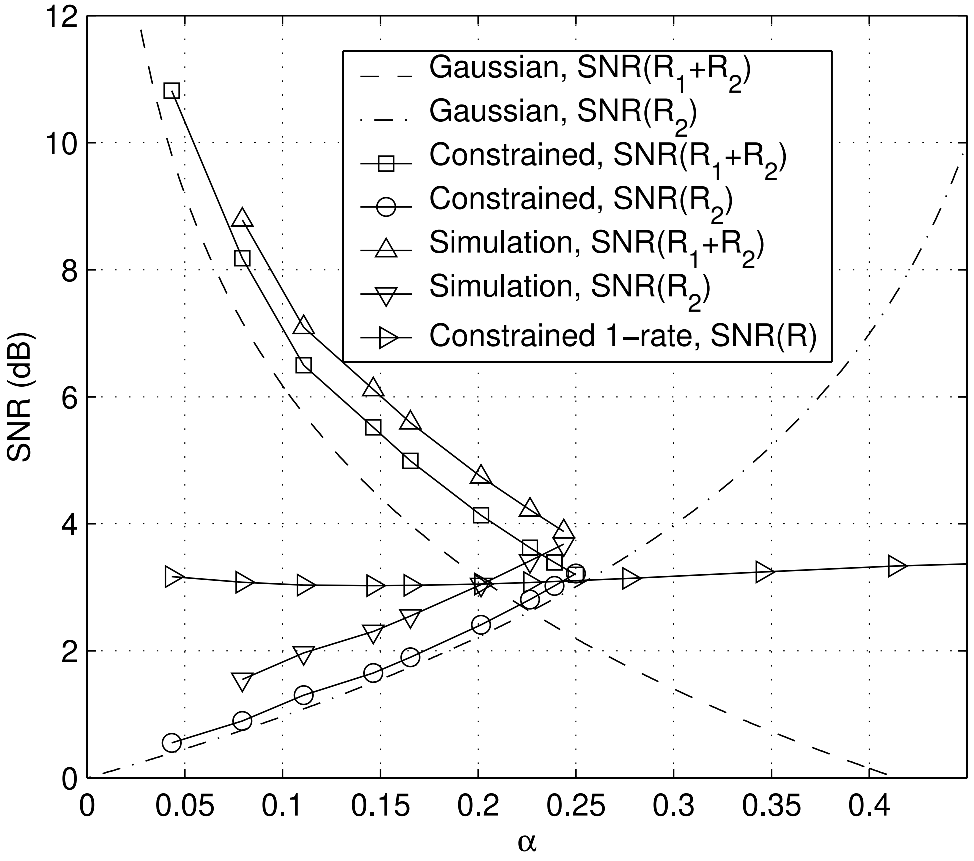

Figure 2.17: SNR required for error-free theorectical performance and simulated performance with $BER = 10^{-5}$ for high rate and low rate Rx vs. α; IL = 8,192; number of iter. = 15; $R_1 = 0.5$ (bit/s/Hz); $R_2 = 1$ (bit/s/Hz); 8-point circular constellation

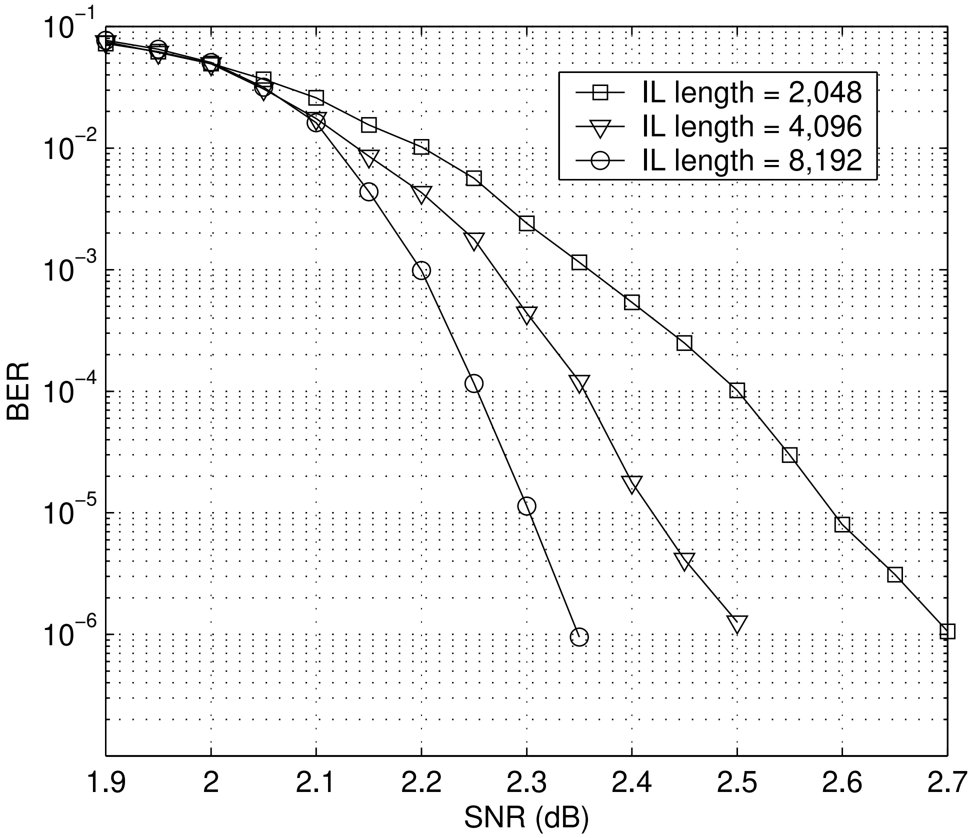

Figure 2.18: BER vs. SNR at low SNR range; $\alpha = 0.1464$; number of iteration $= 15$; $R_1 = R_2 = 1$ (bit/s/Hz); 8-PSK

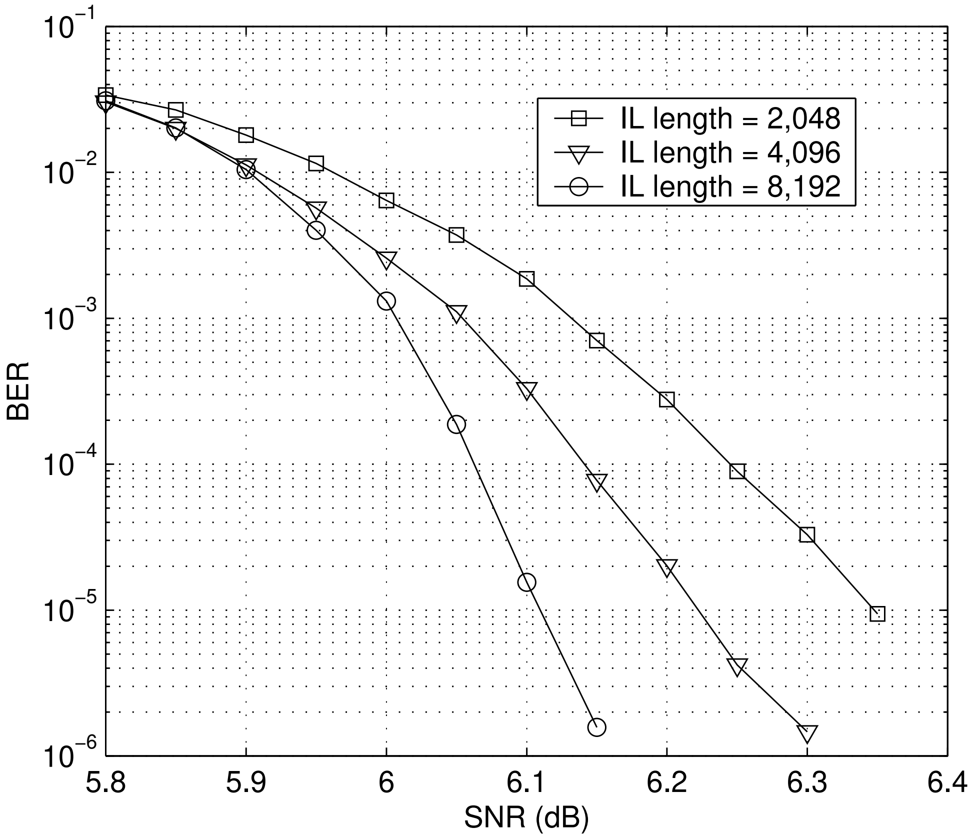

Figure 2.19: BER vs. SNR at high SNR range; $\alpha = 0.1464$; number of iteration $= 15$; $R_1 = R_2 = 1$ (bit/s/Hz); 8-PSK

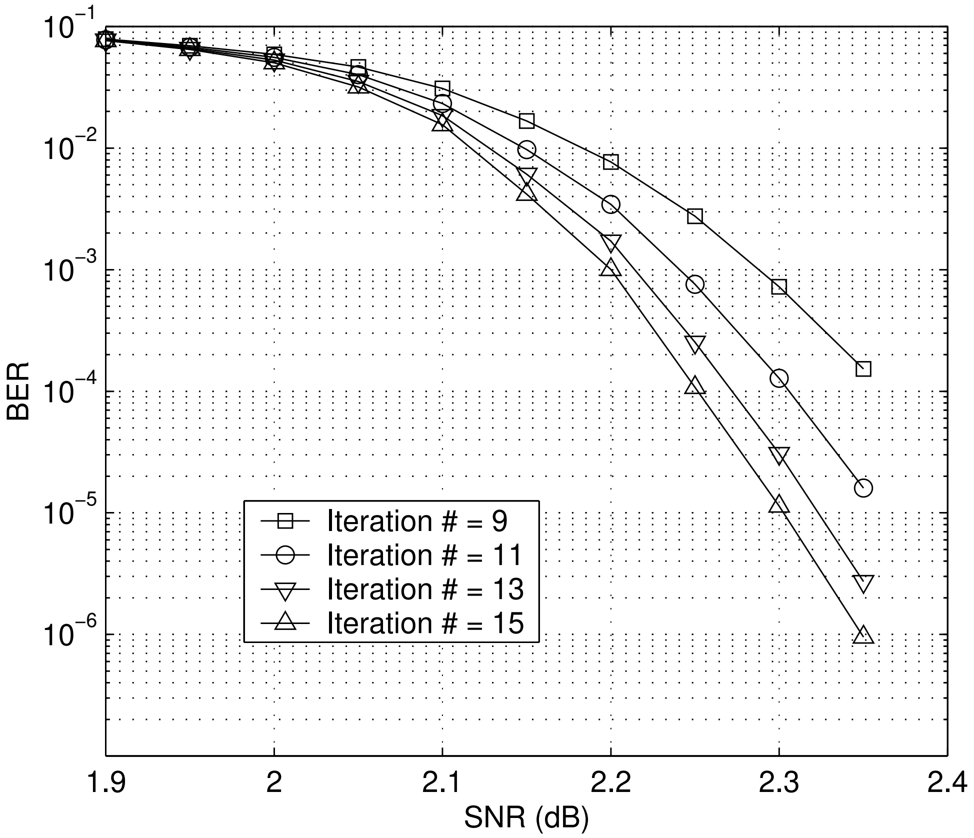

Figure 2.20: BER vs. SNR at high SNR range; $\alpha = 0.1464$; IL = 8,192; number of iteration = 15; $R_1 = R_2 = 1$ (bit/s/Hz); 8-PSK

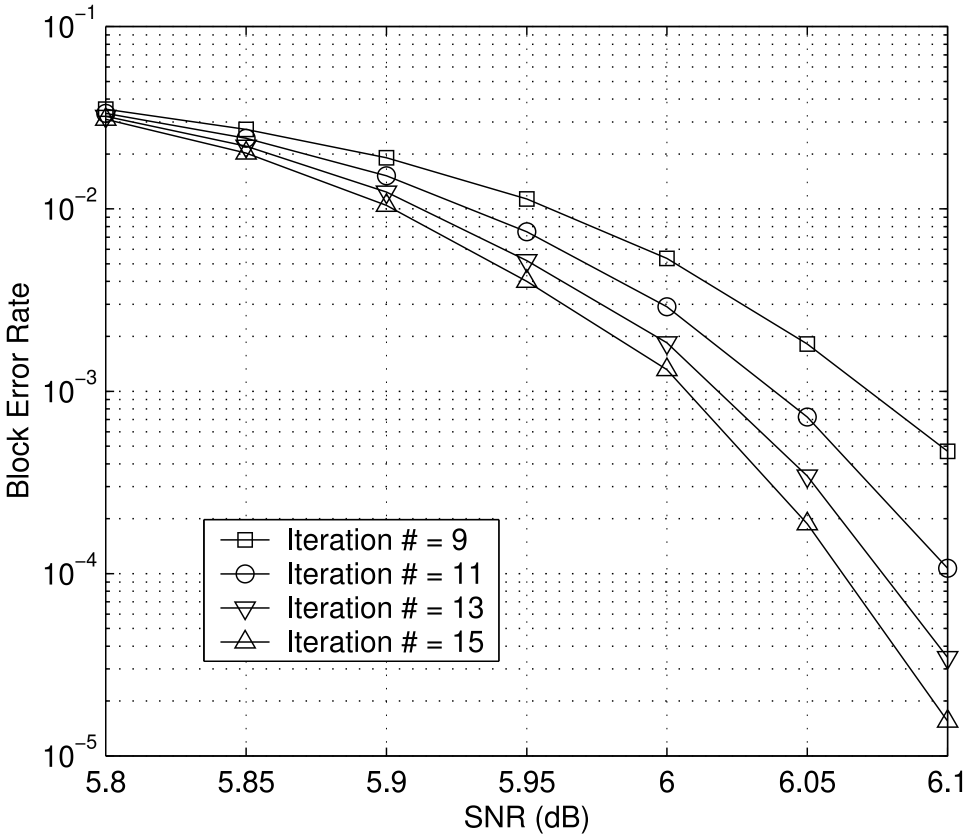

Figure 2.21: BER vs. SNR at low SNR range; $\alpha = 0.1464$; IL = 8,192; number of iteration = 15; $R_1 = R_2 = 1$ (bit/s/Hz); 8-PSK

2.4.3 Three-rate Superposition Structure with 64-QAM

Figure 2.22, 2.23, 2.24 shows the performance as BER vs. SNR for three SNR ranges with $R_1 = R_2 = R_3 = 1$ using standard 64-QAM ($\alpha_1 = 1/21$, $\alpha_2 = 4/21$), where α_1 and α_2 are the power allocation parameters in (2.8-2.9). The constrained capacities are 3.0913 dB, 8.7095 dB and 13.4094 dB for low, middle and high SNR ranges respectively. The interleaver with length of 8,192, 4,096 and 2,048 are ($S = 54, T = 6, X = 1$), ($S = 37, T = 5, X = 1$), and ($S = 26, T = 4, X = 0$) respectively. For standard 64-QAM, at high SNR, the performance is within 0.6 dB of constrained capacity at BER of 10^{-5}, while at middle SNR, the performance is within 0.8 dB of constrained capacity at BER of 10^{-5}. At low SNR, it is within 0.9 dB.

In general, for our simulations, the performance at high SNR is closest to the theoretical limit, and the performance at middle SNR is closer than that at low SNR.

At $BER = 10^{-5}$, the difference between interleaver length of 8,192 and 4,096 is about 0.1 to 0.15 dB, and the difference between interleaver length of 4,096 and 2,048 is about 0.2 dB.

Figure 2.25, Figure 2.26 and Figure 2.20 show the performance degradation when the number of iterations for SISO decoding decreases. There is about 0.05 dB difference between 15 iterations and 11 iterations at $BER = 10^{-5}$. Interleaver length is 8,192.

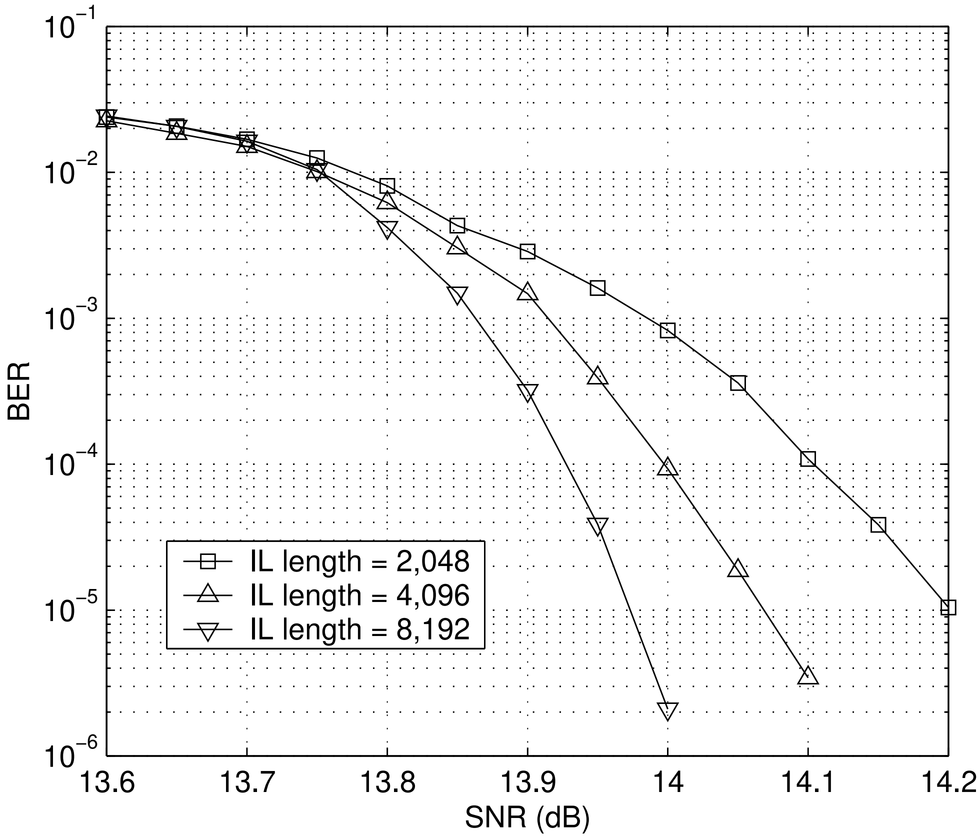

Figure 2.22: Three-rate F-W Structure with 64-QAM at high SNR range, Constrained capacity = 13.4094 (dB), 15 iterations

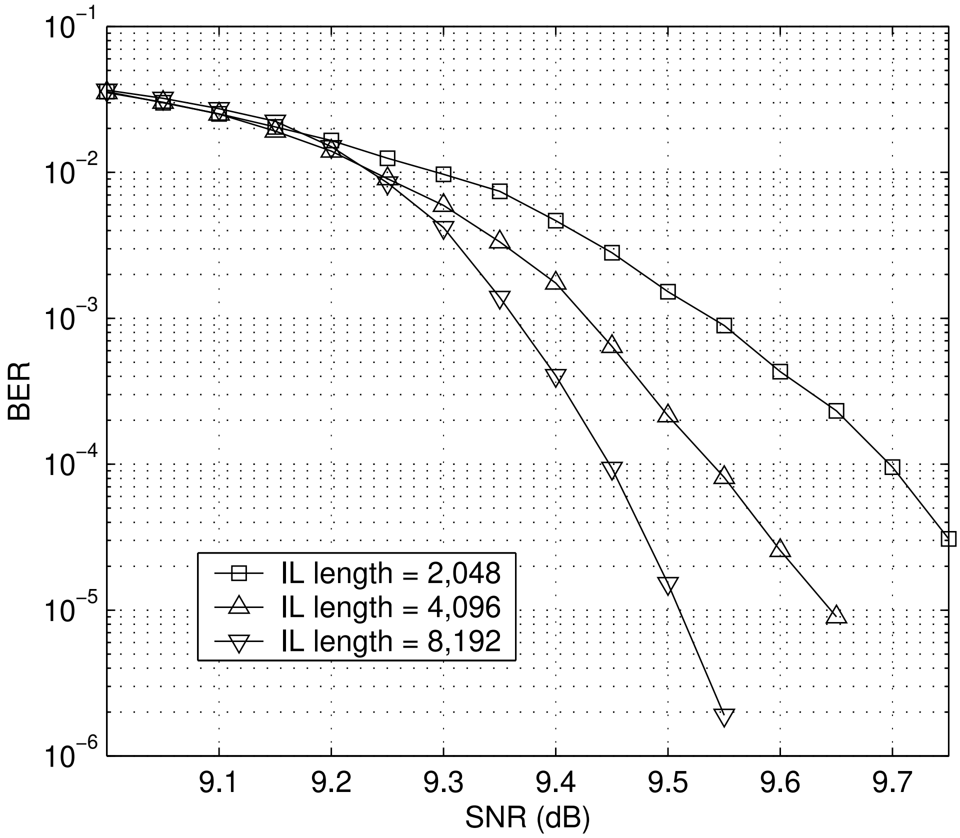

Figure 2.23: Three-rate F-W Structure with 64-QAM at middle SNR range, Constrained capacity = 8.7095 (dB), 15 iterations

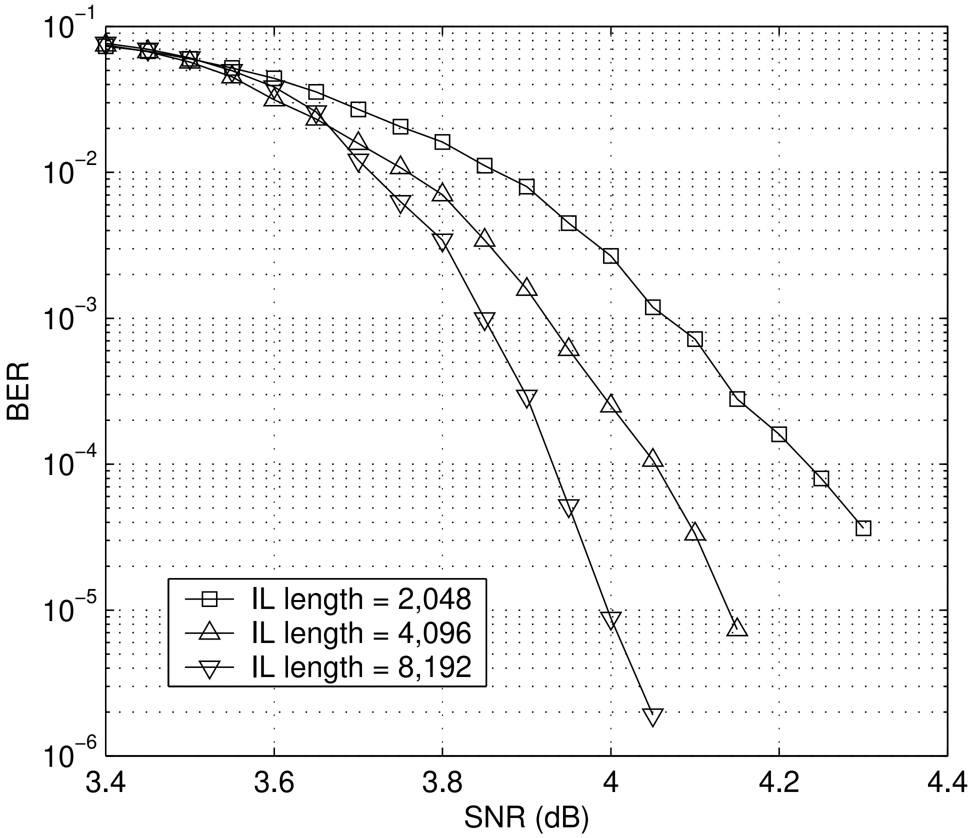

Figure 2.24: Three-rate F-W Structure with 64-QAM at low SNR range, Constrained capacity = 3.0913 (dB), 15 iterations

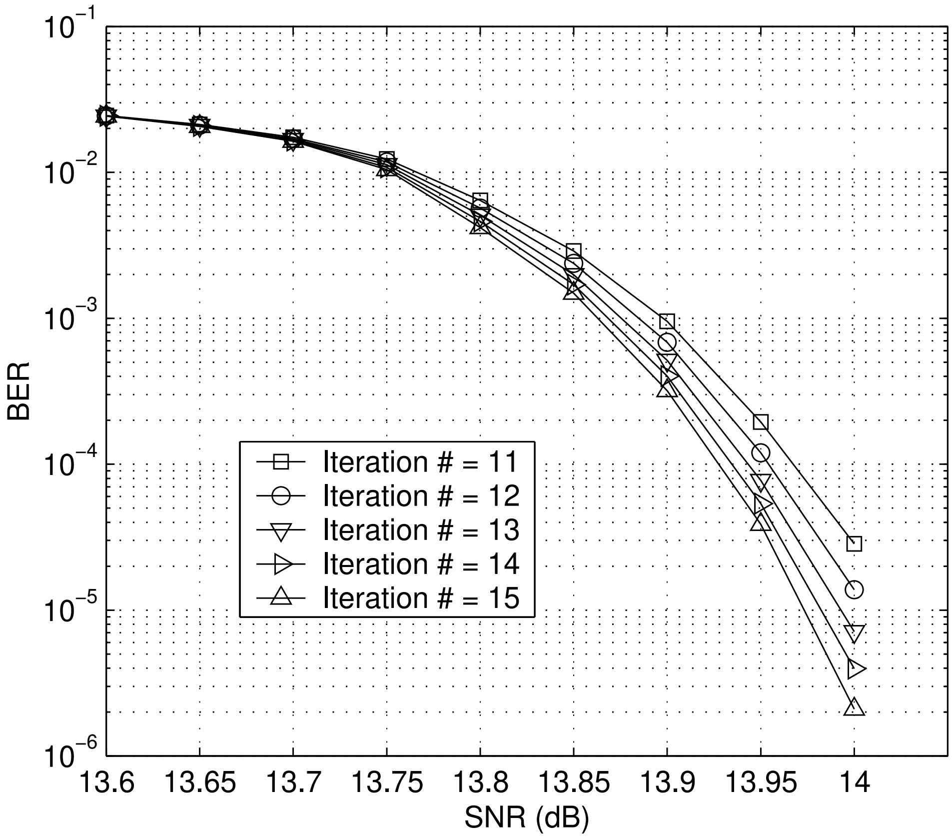

Figure 2.25: BER vs. SNR at high SNR; $\alpha_1 = 1/21$; $\alpha_2 = 4/21$; IL = 8,192; number of iteration = 15; $R_1 = R_2 = 1$ (bit/s/Hz); 64-QAM

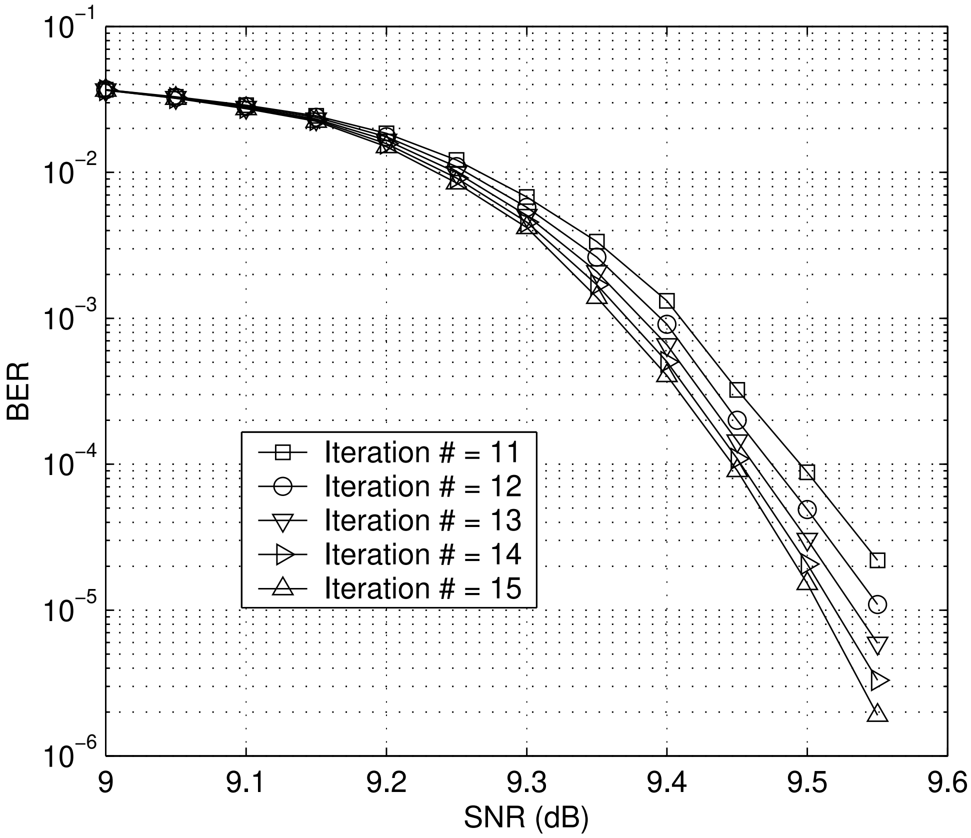

Figure 2.26: BER vs. SNR at middle SNR; $\alpha_1 = 1/21$; $\alpha_2 = 4/21$; IL = 8,192; number of iteration = 15; $R_1 = R_2 = 1$ (bit/s/Hz); 64-QAM

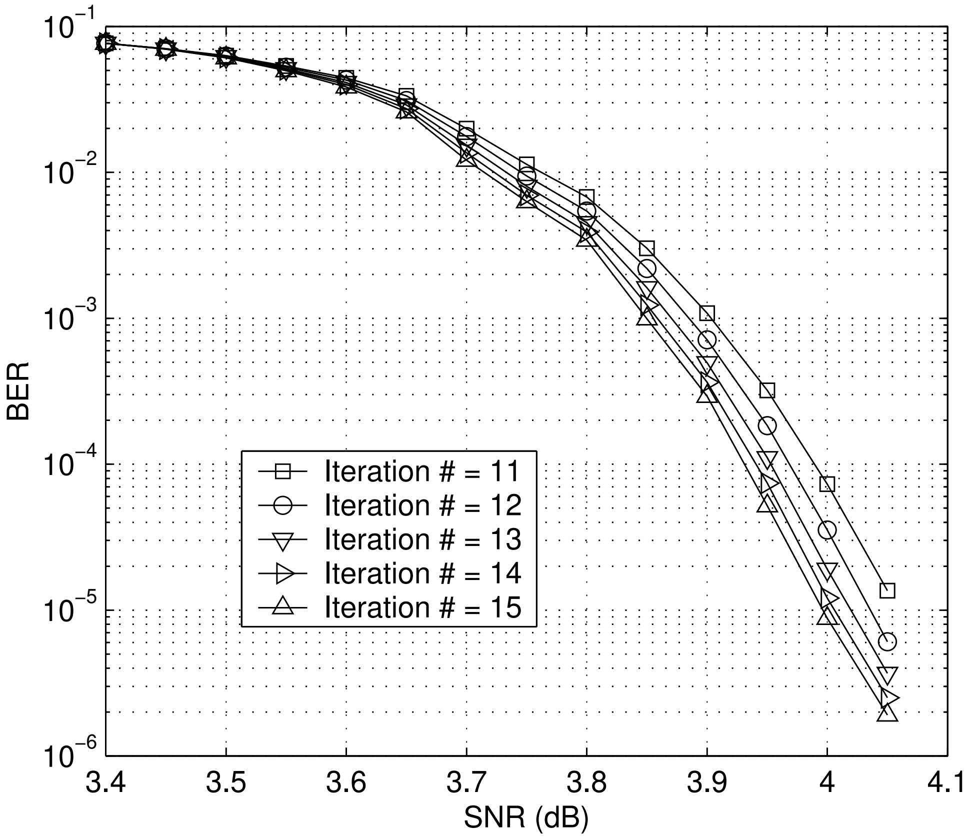

Figure 2.27: BER vs. SNR at low SNR; $\alpha_1 = 1/21$; $\alpha_2 = 4/21$; IL = 8,192; number of iteration = 15; $R_1 = R_2 = 1$ (bit/s/Hz); 64-QAM

2.5 Two-Rate 16-QAM Robertson-Wörz based SCM

We also explored SCM based on the Robertson-Wörz structure described in [16]. Only the two-rate structure with 16-QAM has been simulated for Robertson-Wörz scheme.

2.5.1 Encoder Using Robertson-Wörz Structure

We also explored a superposition turbo TCM with Robertson-Wörz (R-W) structure.

Figure 2.28 shows the structure of the superposition encoder. It is a parallel concatenated trellis-coded modulation (PCTCM) with constituent encoder of rate-2/4. The constituent code consists of two identical recursive convolutional code of rate-1/2. The upper constituent encoder has as systematic outputs both input bits. The lower constituent encoder also has as systematic outputs both input bits. Thus, the systematic bits are outputs of both upper constituent encoder and lower constituent encoder. However, the multiplexer only takes the "even" symbols from the upper constituent encoder and the "odd" symbols from the lower constituent encoder. As a result, the systematic bit is transmitted only once.

There are actually two spread symbol interleavers in the encoder. One for "even" symbols of the block and one for "odd" symbols of the block. Hence, we have less interleaver gain as a trade-off.

The number of trellis edges in the Robertson-Wörz structure is typically

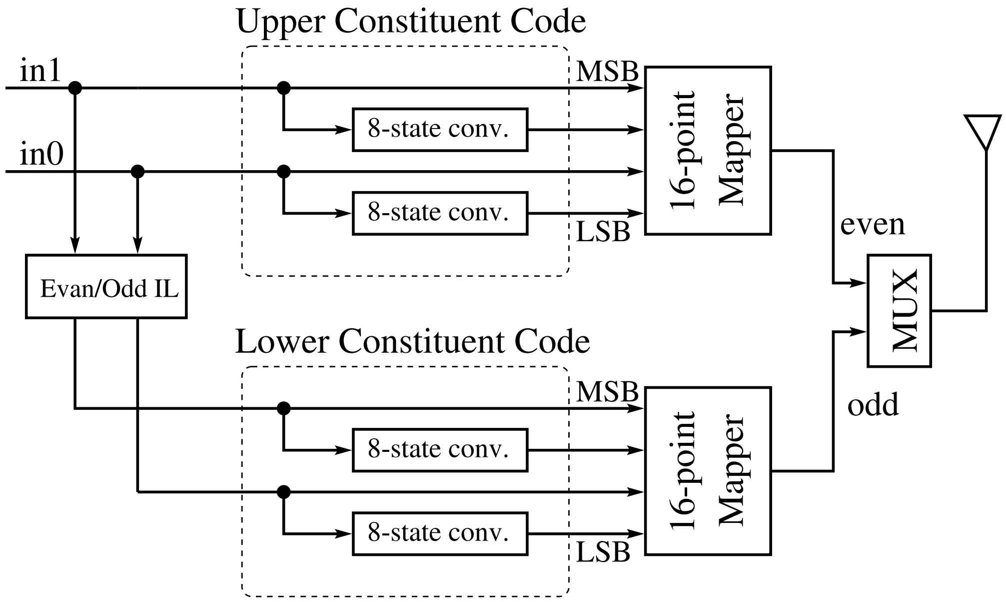

Figure 2.28: PCTCM Superposition Turbo Code Encoders Using Robertson-Wörz Structure for Two Rates and a 16-point Square Constellation

smaller when a high rate constituent code is used. This is attractive in implementation. However, since the Robertson-Wörz structure uses separate interleavers for even symbols and odd symbols, the reduced complexity causes a reduction of the so-called "interleaver gain". In our example, the encoders are all rate-1/2, and as a result both the Fragouli-Wesel (F-W) and Robertson-Wörz (R-W) structures have the same complexity, since the total numbers of trellis edges to be calculated for the same information blocks are the same in both structures.

The 8-state recursive convolutional code we used in our encoder for the Robertson-Wörz structure was found by a search that optimized for normalized

d_{s2}^E. The encoder is described by

$$A = \begin{bmatrix} 0 & 1 & 0 \\ 0 & 0 & 1 \\ 1 & 1 & 0 \end{bmatrix}, \tag{2.33}$$

$$B = \begin{bmatrix} 0 & 0 & 1 \end{bmatrix}, \tag{2.34}$$

$$C = \begin{bmatrix} 0 & 0 \\ 0 & 0 \\ 1 & 0 \end{bmatrix}, \tag{2.35}$$

$$D = \begin{bmatrix} 1 & 1 \end{bmatrix}. \tag{2.36}$$

The upper and lower constituent codes for 16-QAM R-W Superposition turbo coding are identical. The state-space description of the 64-state constituent code is as follow:

$$A = \begin{bmatrix} 0 & 1 & 0 & 0 & 0 & 0 \\ 0 & 0 & 1 & 0 & 0 & 0 \\ 1 & 1 & 0 & 0 & 0 & 0 \\ 0 & 0 & 0 & 0 & 1 & 0 \\ 0 & 0 & 0 & 0 & 0 & 1 \\ 0 & 0 & 0 & 1 & 1 & 0 \end{bmatrix}, \tag{2.37}$$

$$B = \begin{bmatrix} 0 & 0 & 1 & 0 & 0 & 0 \\ 0 & 0 & 0 & 0 & 0 & 1 \end{bmatrix}, \tag{2.38}$$

$$C = \begin{bmatrix} 0 & 0 & 0 & 0 \\ 0 & 0 & 0 & 0 \\ 1 & 0 & 0 & 0 \\ 0 & 0 & 0 & 0 \\ 0 & 0 & 0 & 0 \\ 0 & 0 & 1 & 0 \end{bmatrix}, \tag{2.39}$$

$$D = \begin{bmatrix} 1 & 1 & 0 & 0 \\ 0 & 0 & 1 & 1 \end{bmatrix}. \tag{2.40}$$

2.5.2 Decoder Using Robertson-Wörz Structure

The block diagram of the two-stage-decoding with a SISO decoder for Robertson-Wörz based Superposition stays the same as that in Figure 2.11. The first decoding stage decodes two input MSBs of the labeling of 16-QAM symbols. It uses an 8-state-trellis, and calculates the metric by summing up the squared Euclidean distances between the received symbol and all four constellation points belonging to the same quadrant. For the received symbols of the upper block, only the "even" symbol's metric is updated. Similarly, the received symbols of the lower block, only the "odd" symbol's metric is updated. Before starting the second decoding stage, the whole block of received 16-QAM symbols is converted to QPSK symbols in the same way as in subsection 2.3.2. The second decoding stage decodes two LSB input bits of the labeling of 16-QAM symbols by decoding the resulting QPSK symbols.

Figure 2.29 shows the performance of the Robertson-Wörz based SCM as BER vs. SNR for two SNR ranges. Performance of the Fragouli-Wesel based SCM is included for comparison. The symbol interleaver length is 16,384 which consists of two length-8,192 ($S = 54, T = 6, X = 1$) interleavers for even and odd symbols respectively. At high SNR, the Robertson-Wörz based SCM has performance within 0.7 dB of constrained capacity at BER of 10^{-5}, while at low SNR, the performance is within 0.9 dB of constrained capacity at BER of 10^{-5}.

2.6 Conclusion of Chapter 2

With turbo codes, superposition coding with multi-stage decoding performs quite well, always within 1 dB of the achievable region boundary for our examples. In the context of the work of Cover and Bergmans [4, 6], and the well-known power of turbo codes, this is not that surprising.

The two-stage decoding of the separate 8-state trellises for 16-QAM presented in this paper achieves the same performance as joint decoding of the 64-state overall trellis, while the latter is sixteen times more complicated than the former.

Multilevel coding is a special case of multi-rate superposition coding with α selected so that all rates are decoded at the same SNR. The proposed schemes offers the same complexity and performance as that of the typical single rate turbo TCM, but provides the flexibility of controlling unequal error protection through the choice of α.

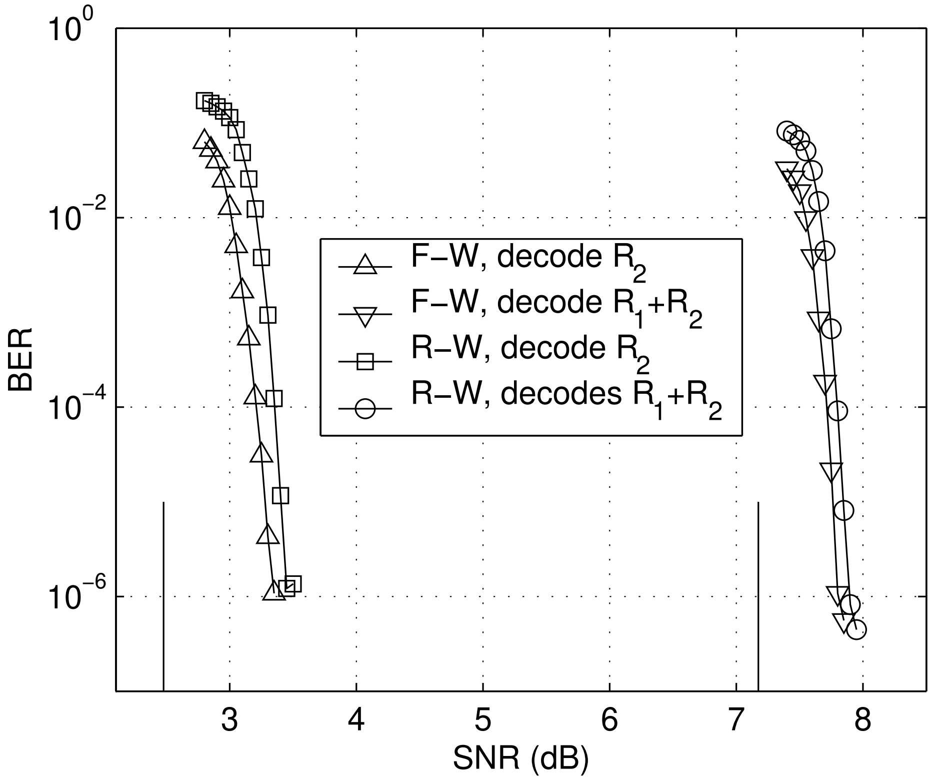

Figure 2.29: Two-rate Superposition Turbo TCM (R-W and F-W) with 16-QAM, $R_1 = R_2 = 1$ bit/s/Hz, Constrained Capacities = 2.4786 (dB), and 7.1746 (dB) respectively, Block length = 32,768 bits for all curves.

Chapter 3

Constellation Labeling for Error-Resilient Source Coding

3.1 Introduction of Chapter 3

When lossy compression is followed by transmission over a noisy channel, the best combination of source and channel coding can be simply a properly labeled source. For example, transmitting a properly scaled Gaussian source directly over a Gaussian channel achieves the theoretical minimum squared-error distortion.

In [27], Zeger and Gersho used a training set to design a pseudo-Gray code labeling that reduced the mean squared error of vector quantized data transmitted over a noisy channel.

This chapter considers 1-D source data under the distortion criterion of maximum Euclidean distance. Under the assumption that bit errors are sparse, we seek a labeling that minimizes the maximum of the Euclidean distance associated with a single bit error. We call this quantity d_{max}. This chapter lower bounds

d_{max} and proposes a labeling which approaches that lower bound.

One year after the publication of [28], we found that similar results were derived by Harper in [29] in 1964. The proof in this chapter is different from that of Harper. In [29], the proof utilizes graph theory.

Section 3.2 introduces basic definitions, and examines the d_{max} performance of Gray-code labeling and natural labeling. Section 3.3 derives three lower bounds on d_{max}. Section 3.4 proposes the Monotonic Decreasing Hamming Weight (MDHW) labeling, and analyzes the performance of MDHW labeling. Section 3.5 concludes the chapter. Appendix 3.6.1 describes some interesting properties and an important lemma which is useful in proving Theorem 2. Appendix 3.6.2 proves the close form expression of d_{max} of the MDHW labeling. Appendix 3.6.3 proves that the MDHW labeling outperforms natural labeling.

3.2 The Problem Statement

3.2.1 Basic Definitions

For our analysis, constellations are fully-connected, weighted graphs in which the constellation points are the vertices. Figure 3.1 shows an example of such a graph for a 2-bit 1-D constellation, with arcs illustrating each edge. In this chapter,

only the edges with Unit-Hamming-Weight (UHW) are considered. We use edges to represent UHW edges in this chapter. When the constellation is labeled, each of 2^n vertices has an n-bit label. Then each edge has both a label and weight. The edge label is the exclusive-or of the labels of two points connected by the edge. The edge weight is equal to the Euclidean distance between the two corresponding points. These definitions are the same as used in [18]. The

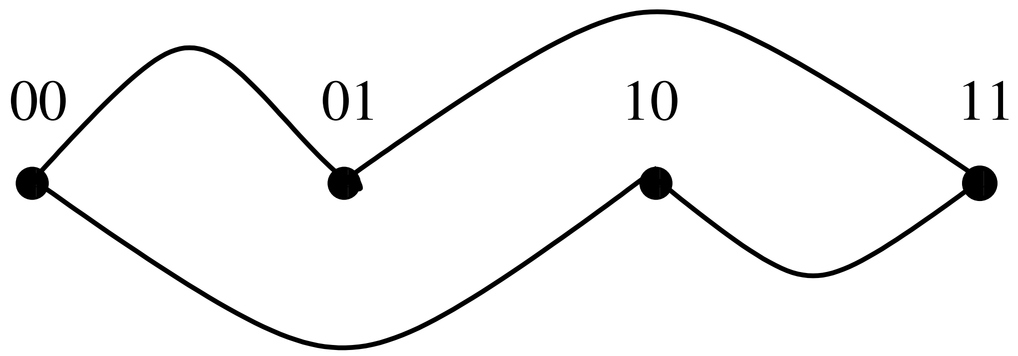

Figure 3.1: 2-bit one dimensional labeling

Euclidean distance between any two adjacent points is assumed to be 1.

In n-bit 1-D labeling, the $d_{pmax}(i)$ of constellation point i is defined as the maximum Euclidean distance from the constellation point i to any of the n other constellation points which have edges connecting to point i. d_{max} of a labeling is defined as the maximum of $d_{pmax}(i)$ of all 2^n constellation points.

$$d_{max} = \max_i d_{pmax}(i) \tag{3.1}$$

where $i = 1, 2, \cdots, 2^n$.

3.2.2 Gray-Code (GC) Labeling and Natural Labeling

The commonly used Gray-code labeling [30] turns out to be the worst possible labeling for this problem with $d_{max} = 2^n - 1$. For this labeling, the labels of the two end points differ by only one bit. Figure 3.2 shows such a GC labeling of 3-bit 1-D source coding.

The "natural" labeling uses binary labels in the order of the integers they

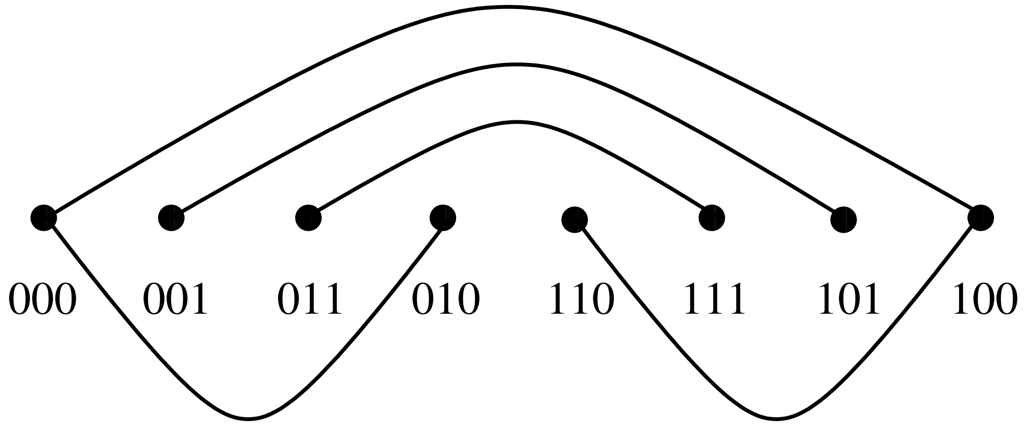

Figure 3.2: 3-bit 1-D GC labeling (edges with $d_{pmax}(i)$ are shown)

represent. For this labeling, $d_{pmax}(i) = 2^{n-1}$ for all $i = 1, 2, \cdots, 2^n$. Hence $d_{max} = 2^{n-1}$. Figure 3.3 shows such a natural labeling of 3-bit 1-D source coding.

3.3 Lower Bound of the d_{max}

This section examines lower bounds on d_{max} before the design of an effective labeling. We present three lower bounds of the d_{max} in this section.

Lemma 1 *For n-bit 1-D labeling,*

$$d_{max} \geq 2n - 2 \tag{3.2}$$

Proof: We study the labeling of the most left $2n$ points. We name them points i ($i = 1, 2, \cdots, 2n$) starting with the left end point. Without loss of generality, label point 1 with all zeros.

Assume that the Hamming weight of point 2 is one. Now consider the remaining $2n - 2$ points of interest. To minimize d_{max}, it is necessary to label $n - 1$ of

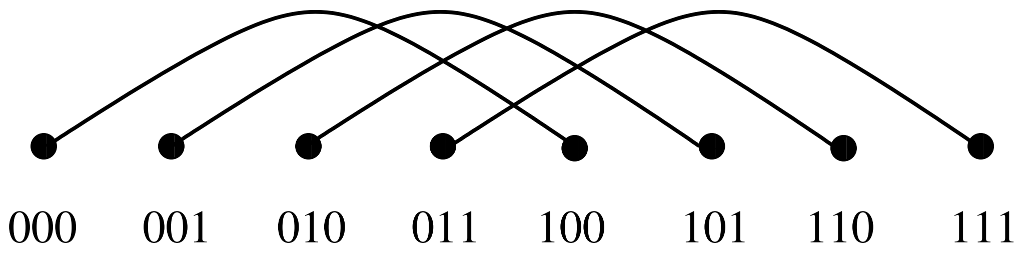

Figure 3.3: 3-bit 1-D natural labeling (edges with $d_{pmax}(i)$ are shown)

those $2n-2$ points with the rest of the $n-1$ UHW labelings, and label $n-1$ of those $2n-2$ points with Hamming-weight-2 labelings which have unit Hamming distance from point 2. This leads to inequality (3.2).

If the Hamming weight of point 2 is two, we have to label n of those $2n-2$ points with UHW labelings, and the remaining $n-2$ of those $2n-2$ points with Hamming-weight-3 labelings that have unit Hamming distance from point 2. This also leads to inequality (3.2).

At last, we examine the case that the Hamming weight of point 2 (w_2) is greater than two. To satisfy inequality (3.2), we need to label n of those $2n-2$ points with UHW labelings, and n of those $2n-2$ points with Hamming-weight-(w_2-1) labelings which has unit Hamming distance from point 2. Thus, it is impossible to satisfy inequality (3.2) under this condition. That means $d_{max} > 2n-2$ for this case.

Hence, inequality (3.2) is proved. $\square$

Figure 3.4 shows an example of 3-bit 1-D labeling.

Lemma 2 *For n-bit 1-D labeling, and $n \geq 2$,*

$$d_{max} > \frac{2^n - 1}{n} \tag{3.3}$$

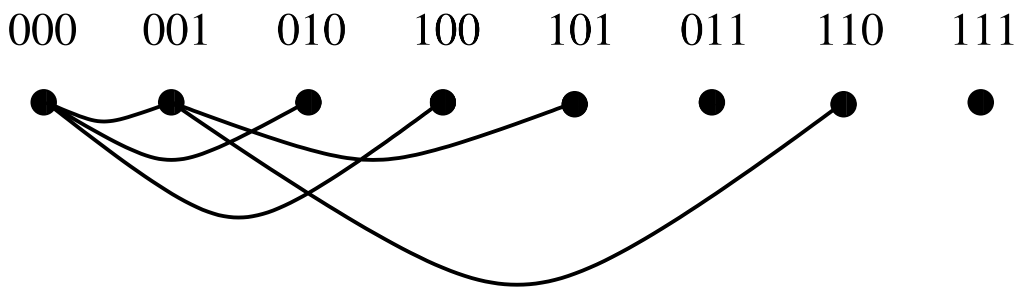

Figure 3.4: $d_{max} \geq 2n-2$ in n-bit 1-D labeling

Proof: Without loss of generality, label the left end point with all zeros. Consider a path from the left end point to the right end point traveling along exactly w edges, where w is the Hamming weight of the right end point. The minimum distance of such a path is $2^n - 1$. This is achieved when there is no back tracking. Since d_{max} is longer than the average length of a UHW edge in our path, $d_{max} \geq \frac{2^n-1}{w}$. To minimize this lower bound, label the right end point with all ones. In this case, $d_{max} \geq \frac{2^n-1}{n}$. In fact, the inequality is strict because there are multiple paths of edges connecting the left end point to the right end point, and at most one of these paths has all edges with equal lengths. $\square$

Lemma 3 *For n-bit 1-D labeling, and $n \geq 2$,*

$$d_{max} > \frac{2^n - 1 - \sum_{i=0}^{n-1-\lfloor \frac{n}{2} \rfloor} \begin{pmatrix} n \\ i \end{pmatrix}}{\lfloor \frac{n}{2} \rfloor} \tag{3.4}$$

Proof: Without loss of generality, label the left end point with all zeros. Let's consider $\begin{pmatrix} n \\ i \end{pmatrix}$ weight (n-i) points, There are $(n-i)! \cdot \begin{pmatrix} n \\ i \end{pmatrix}$ i-UHW-edge paths from the left end point (i.e. weight 0 point) to each of those $\begin{pmatrix} n \\ i \end{pmatrix}$ weight (n-i) points. We claim that for any labeling, there exists such path(s) that the i-edge path sum

$$S_{n-i} = \sum_{j=1}^{n-i} UHWedge(j) \geq 2^n - 1 - \sum_{j=1}^{n-1-i} \binom{n}{j} \tag{3.5}$$

The necessary and sufficient condition for equality are:

(1) All points with weight greater than i occupies those right most positions.

(2) All those $(n-i)! \cdot \binom{n}{i}$ i-UHW-edge paths are going right (i.e. no back tracking).

The brief of the proof of the claim is following:

(i) If no back tracking,

$$S_{n-i} = \sum_{j=1}^{n-i} UHWedge(j) = 2^n - 1 - \sum_{j=1}^{n-1-i} \binom{n}{j} \tag{3.6}$$

(ii) Contradiction exists if not all points with weight greater than i occupying those right most positions.

Last, it is easy to prove that when $i = \lfloor \frac{n}{2} \rfloor$, we have the tightest lower bound of this family. □

The lower bound in (3.2) can be achieved for $n = 2$ and $n = 3$. As indicated in the proof of Lemma 2, the lower bounds in (3.3) and (3.4) are never achievable. Additionally, (3.2) is tighter than (3.3) and (3.4) for small n, while (3.4) and (3.3) are tighter than (3.2) for large n as shown in Figure 3.5. The combined lower bound of the d_{max} can be the maximum of lower bounds in (3.2) and (3.4) under various n.

3.4 Monotonic Decreasing Hamming Weight Labeling for n-bit 1-D Source Coding

We now describe the best labeling we have found in terms of minimizing d_{max}.

3.4.1 Definition of MDHW Labeling

For n-bit 1-D labeling, with 2^n n-bit unsigned binary numbers as point labels, label points according to the following two rules:

(i) Binary numbers with least Hamming weight should be chosen first.

(ii) Under (i), the binary number should be selected in numerical order, with the largest first.

For example, MDHW labeling for 3-bit 1-D source coding is:

$$\{000,\ 100,\ 010,\ 001,\ 110,\ 101,\ 011,\ 111\}$$

More examples of n-bit 1-D labeling for $n = 2, 3, 4$, and 5 are shown in Figure 3.6.

3.4.2 d_{max} of MDHW Labeling

The following theorem shows the performance of MDHW labeling in terms of d_{max}.

Theorem 2 *For MDHW labeling for n-bit 1-D source coding, $n \geq 2$,*

$$d_{max} = 1 + \sum_{i=1}^{n-1} \binom{i}{\lfloor \frac{i}{2} \rfloor} \tag{3.7}$$

Proof: With Property 1 to 3 and Lemma 4 in Appendix, Equation 3.7 is proved in Appendix 3.6.2. □

With Theorem 2, the following Corollary can be easily proved.

Corollary 1 *The MDHW labeling outperforms the natural labeling for n-bit 1-D source coding, $n \geq 2$, i.e.*

$$1 + \sum_{i=1}^{n-1} \binom{i}{\lfloor \frac{i}{2} \rfloor} \leq 2^{n-1} \tag{3.8}$$

Proof: See Appendix 3.6.3. □

Figure 3.5 displays d_{max} of both GC labeling and natural labeling, along with that MDHW labeling and three of its lower bounds. In addition, Figure 3.5 shows that d_{max} of MDHW labeling is not greater than that of natural labeling. With Theorem 2, the observation can be easily proved through induction.

The exhaustive search result shows that the MDHW labeling is optimal for $n = 2, 3$, and 4 1-D source coding.

Note that a $2n$-bit (n by n) 2-D constellation labeled with the direct product of two MDHW n-bit 1-D labelings will achieve the same d_{max} as n-bit 1-D and source coding.

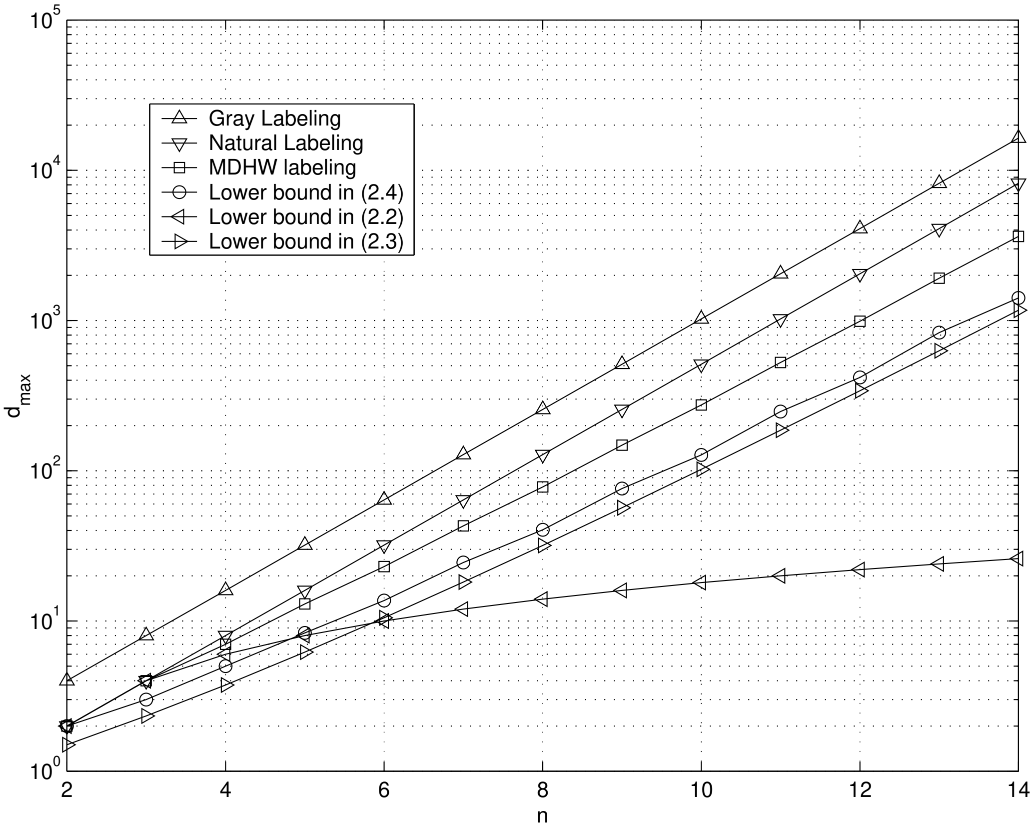

Figure 3.5: d_{max} of n-bit 1-D labeling vs. n

3.5 Conclusion of Chapter 3

This chapter lower bounds a metric d_{max}, and proposes the Monotonic-Decreasing-Hamming-Weight (MDHW) labeling for n-bit 1-D source coding which approaches the lower bound closer than any other labelings examined. d_{max} is the maximum of the Euclidean distance between any two constellation points which have unit Hamming distance between their point labeling. The analytical result of d_{max} is derived. The total number of points whose d_{pmax} reaches d_{max}, and their location in n-bit 1-D MDHW labeling are also derived. A $2n$-bit (n by n) 2-D constellation labeled with the direct product of two MDHW n-bit 1-D labelings will achieve the same d_{max} as n-bit 1-D source coding.

A year after the publication of [28], we found that similar results were derived by Harper in [29] in 1964 utilizing a different method, graph theory.

3.6 Appendix

3.6.1 Properties and Lemma about Labeling

Some properties can be directly obtained from the definition of MDHW labeling.

Property 1 *The MDHW point label of n-bit 1-D quantization can be divided into $n+1$ sections, with each section having a constant Hamming weight. The order of Hamming weights is:* $0, 1, 2, ..., n$.

Property 2 *Any point has n UHW neighbors, whose labels differ in one bit from the point of interest. For any point in section i, i UHW neighbors are in section $i-1$ while other $n-i$ UHW neighbors are in section $i+1$.*

Property 3 *The MDHW point labeling is complementary symmetric, i.e. the label for point i is the bitwise complement of the label for point $2^n - i$.*

Proof: Complement all bits of 2^n rows in MDHW labeling, the Hamming weight in sector i becomes $n - i$. Hence, the Hamming weight in each sectors with the same weight (from top to bottom) in the order of: $n, n-1, ..., 0$. Also, consider row m and $m+1$ within the same section i, the rule from row m to row $m+1$ becomes a new rule: the largest possible unsigned binary number should be selected as the next row. However, that the rule from row $m+1$ to row m is the same as rule (ii) stated at Section 3.4.1. Thus, the complemented labeling is the same if we start at last row and up instead of starting at first row down. As a result, Property 3 is true. $\square$

Property 4 *Total number of paths from weight 0 point (i.e. all "one" point) to weight n point (i.e. all "zero" point) with exactly n edges is $n!$.*

Property 5 *Total number of UHW edges paths connecting weight i points and weight $i+1$ points is*

$$(n-i) \cdot \begin{pmatrix} n \\ i \end{pmatrix} = (i+1) \cdot \begin{pmatrix} n \\ i+1 \end{pmatrix} = \frac{n!}{i!(n-i-1)!}. \tag{3.9}$$

Lemma 4 *For MDHW n-bit 1-D labeling with $n \geq 2$, there is a point $\{P_i\}$ in section $i = \lfloor \frac{n-1}{2} \rfloor$, which has an UHW neighbor $\{P_{i+1}\}$ in section $i+1$ such that the Euclidean distance between $\{P_i\}$ and $\{P_{i+1}\}$ is d_{max}. In addition, the Euclidean distance between $\{1P_i\}$ and $\{1P_{i+1}\}$ is d_{max} of $(n+1)$-bit 1-D labeling.*

Proof: The Lemma 4 can be proved through induction.

With MDHW labeling, section i can be divided into two subsections i_1 and i_0, where the subscripts indicates the MSB of labels in that subsection. There are $\begin{pmatrix} n \\ i \end{pmatrix}$ points in section i, with $\begin{pmatrix} n-1 \\ i-1 \end{pmatrix}$ in subsection i_1 and $\begin{pmatrix} n-1 \\ i \end{pmatrix}$ in subsection i_0.

Note that with MDHW labeling, subsection i_1 of n-bit 1-D labeling is identical to section $i-1$ of $(n-1)$-bit 1-D labeling, except for the additional MSB in the $2n$-bit 1-D labels. Similarly, subsection i_0 is identical to section i of $(n-1)$-bit 1-D labeling except for the additional MSB in the n-bit 1-D labels. Figure 3.6 shows these relationships.

(1) n = 2:

Point label	d_{pmax}
0 0	2
1 0	2
0 1	2
1 1	2

(2) n = 3:

Point label	d_{pmax}
0 0 0	3
1 0 0	4
0 1 0	4
0 0 1	3
1 1 0	3
1 0 1	4
0 1 1	4
1 1 1	3

(3) n = 4:

Point label	d_{pmax}
0 0 0 0	4
1 0 0 0	6
0 1 0 0	7
0 0 1 0	7
0 0 0 1	6
1 1 0 0	7
1 0 1 0	7
1 0 0 1	6
0 1 1 0	6
0 1 0 1	7
0 0 1 1	7
1 1 1 0	6
1 1 0 1	7
1 0 1 1	7
0 1 1 1	6
1 1 1 1	4

identical

identical

(4) n = 5:

Point label	d_{pmax}
0 0 0 0 0	5
1 0 0 0 0	8
0 1 0 0 0	10
0 0 1 0 0	11
0 0 0 1 0	11
0 0 0 0 1	10
1 1 0 0 0	12
1 0 1 0 0	13
1 0 0 1 0	13
1 0 0 0 1	12
0 1 1 0 0	13
0 1 0 1 0	13
0 1 0 0 1	12
0 0 1 1 0	12
0 0 1 0 1	11
0 0 0 1 1	11
1 1 1 0 0	11
1 1 0 1 0	11
1 1 0 0 1	12
1 0 1 1 0	12
1 0 1 0 1	13
1 0 0 1 1	13
0 1 1 1 0	12
0 1 1 0 1	13
0 1 0 1 1	13
0 0 1 1 1	12
1 1 1 1 0	10
1 1 1 0 1	11
1 1 0 1 1	11
1 0 1 1 1	10
0 1 1 1 1	8
1 1 1 1 1	5

Section 2_1

Section 2

Section 2_0

Figure 3.6: MDHW labeling of n-bit 1-D labelings for $n = 2, 3, 4,$ and 5

We are now showing two facts in the following proof. First, when $n = 2$, there is a specific point $\{P_i\}$ in section $i = \lfloor \frac{n-1}{2} \rfloor$, its furtherest UHW neighbor is $\{P_{i+1}\}$ in section $i+1$ with the Euclidean distance between them of d_{max}. Second, if the furtherest UHW neighbor of the point $\{P_i\}$ is the point $\{P_{i+1}\}$ in n-bit 1-D labeling, the furtherest UHW neighbor of the point $\{1P_i\}$ is the point $\{1P_{i+1}\}$ in $(n+1)$-bit 1-D labeling, since the Euclidean distance between $\{1P_i\}$ and the point $\{1P_{i+1}\}$ increases the most from the Euclidean distance between $\{P_i\}$ and the point $\{P_{i+1}\}$ among all of the increase of the Euclidean distances from $\{P_i\}$ -$\{P_U\}$ distance to $\{1P_i\}$ -$\{1P_U\}$ distance. $\{P_U\}$ is any one of the UHW neighbors of point $\{P_i\}$.

When $n = 2$, section 0 has one point $\{00\}$ ($\{P_i\}$). Its furtherest UHW neighbor is $\{01\}$ ($\{P_{i+1}\}$) in section 1. For $n = 3$, point $\{100\}$ ($\{1P_i\}$) is in section 1, and point $\{101\}$ ($\{1P_{i+1}\}$) is in section 2 with the Euclidean distance between $\{1P_i\}$ and $\{1P_{i+1}\}$ is d_{max} of 3-bit 1-D labeling. Lemma 4 holds for $n = 2$.

Assume for $n = k$, Lemma 4 is true. When $n = k + 1$, for a point in subsection i_1 with label $\{1P_i\}$, its Euclidean distance to the point $\{1P_{i+1}\}$ in subsection $(i+1)_1$ is equal to d_{max}. It increases by $\begin{pmatrix} k \\ i \end{pmatrix}$, the block length of section $\{0P_i\}$, from the UHW edge between point $\{P_i\}$ and point $\{P_{i+1}\}$ in k-bit 1-D labeling due to the following two facts. First of all, in k-bit 1-D labeling, the Euclidean distance between point $\{P_i\}$ and point $\{P_{i+1}\}$ equals d_{max}. Secondly, in $(k+1)$-bit 1-D labeling, the Euclidean distance between point $\{1P_i\}$ and any of its i UHW neighbor points in subsection $(i-1)_1$ increases by $\begin{pmatrix} k \\ i-1 \end{pmatrix}$. The Euclidean distance between point $\{1P_i\}$ and any of its $k - i$ UHW neighbor points in subsection $(i+1)_1$ increases by $\begin{pmatrix} k \\ i \end{pmatrix}$. And, the Euclidean distance between point $\{1P_i\}$ and $\{0P_i\}$ is $\begin{pmatrix} k \\ i \end{pmatrix}$. For $i = \lfloor \frac{k}{2} \rfloor$, $\begin{pmatrix} k \\ i \end{pmatrix} > \begin{pmatrix} k \\ i-1 \end{pmatrix}$. In fact, the increase of $\begin{pmatrix} k \\ i \end{pmatrix}$ in Euclidean distance is the maximum among the increases from any possible $\{P_j\}$-$\{P_{j+1}\}$ pairs in k-bit 1-D labeling to $\{1P_j\}$-$\{1P_{j+1}\}$ pairs in $(k+1)$-bit labeling. $j = 0, 1, \cdots, k-1$. Thus, we proved that Lemma 4 is true for $n = k+1$. Hence, Lemma 4 is true for any $n \geq 2$. $\square$

3.6.2 Proof of Theorem 2

In addition to equation (3.7) in Theorem 2, we claim that there are $2^{\lfloor \frac{n}{2} \rfloor + 1}$ points whose $d_{pmax}(i)$ equal d_{max} in the middle four subsections of n-bit 1-D point labeling.

If n is even, $2^{\lfloor \frac{n}{2} \rfloor - 1}$ points whose $d_{pmax}(i)$ equal d_{max} are located in subsection $(\lfloor \frac{n-1}{2} \rfloor)_0$, subsection $(\lfloor \frac{n+1}{2} \rfloor)_1$, subsection $(\lfloor \frac{n+1}{2} \rfloor)_0$, and subsection $(\lfloor \frac{n+3}{2} \rfloor)_1$ respectively.

If n is odd, $2^{\lfloor \frac{n}{2} \rfloor - 1}$ points whose $d_{pmax}(i)$ equal d_{max} are located in subsection $(\lfloor \frac{n-1}{2} \rfloor)_1$, subsection $(\lfloor \frac{n-1}{2} \rfloor)_0$, subsection $(\lfloor \frac{n+1}{2} \rfloor)_1$, and subsection $(\lfloor \frac{n+1}{2} \rfloor)_0$ respectively.

Proof: The sketch of the proof is as follow: First, we verify the inequality (3.8) is true for the even and odd special case $n = 2$, and $n = 3$. Second, through induction, we proved that inequality (3.8) is true for any even or odd n by Lemma 4. And we specifically identify the subsections where those points whose $d_{pmax}(i)$ equals d_{max} belong to.

For $n = 2$, all four points i have $d_{pmax}(i) = d_{max} = 2$, where $i = 1, \cdots, 4$.

For $n = 3$, Four out of eight points have $d_{pmax} = d_{max} = 4$.

Next, we just consider the points in section i, where $0 \leq i \leq \lfloor \frac{n-1}{2} \rfloor$, due to the symmetric property.

Assume for $n = k$, Theorem 2 is true. Now, let $n = k + 1$.

If k is odd (i.e. $k+1$ is even). By assumption, there are $2^{\lfloor \frac{k}{2} \rfloor}$ points whose d_{pmax} equal d_{max} of 2^k-PAM in section $\lfloor \frac{k-1}{2} \rfloor$ of k-bit 1-D source labeling, $2^{\lfloor \frac{k}{2} \rfloor -1}$ each for subsections $\lfloor \frac{k-1}{2} \rfloor_1$ and $\lfloor \frac{k-1}{2} \rfloor_0$. Due to symmetry, there are $2^{\lfloor \frac{k}{2} \rfloor}$ points whose d_{pmax} equal d_{max} of k-bit 1-D source labeling in section $\lfloor \frac{k-1}{2} \rfloor + 1$ of 2^k-PAM. As stated in the proof of Lemma 4, subsection $(\lfloor \frac{k}{2} \rfloor)_0$ of $k+1$-bit 1-D labeling is identical to section $\lfloor \frac{k-1}{2} \rfloor + 1$ of k-bit 1-d labeling, if we discard the "0" value MSB of the former. Additionally, subsection $(\lfloor \frac{k}{2} \rfloor + 1)_0$ of $k+1$-bit 1-D labeling is identical to section $\lfloor \frac{k-1}{2} \rfloor + 1$ of k-bit 1-D labeling, if we discard the "0" value MSB of the former.

Since the points whose d_{pmax} equal d_{max} of k-bit 1-D source labeling are located in sections $\lfloor \frac{k-1}{2} \rfloor$ and $\lfloor \frac{k-1}{2} \rfloor + 1$ of k-bit 1-D source labeling, and $\begin{pmatrix} k \\ \lfloor \frac{k}{2} \rfloor \end{pmatrix} = \begin{pmatrix} k \\ \lfloor \frac{k}{2} \rfloor + 1 \end{pmatrix} > \begin{pmatrix} k \\ i \end{pmatrix}$, with $0 \leq i \leq \lfloor \frac{k}{2} \rfloor$, by Lemma 4, there are $2^{\lfloor \frac{k+1}{2} \rfloor -1}$ points whose d_{pmax} equal d_{max} of $k+1$-bit 1-D source labeling in subsections $(\lfloor \frac{k}{2} \rfloor)_0$ and $(\lfloor \frac{k}{2} \rfloor + 1)_0$ of $k+1$-bit 1-D source labeling. Due to symmetry, there are $2^{\lfloor \frac{k+1}{2} \rfloor -1}$ points whose d_{pmax} equal d_{max} of $k+1$-bit 1-D source labeling in subsections $(\lfloor \frac{k}{2} \rfloor + 1)_1$ and $(\lfloor \frac{k}{2} \rfloor + 2)_1$ of $k+1$-bit 1-D source labeling.

If k is even (i.e. $k+1$ is odd). By assumption, there are $2^{\lfloor \frac{k}{2} \rfloor -1}$ points whose d_{pmax} equal d_{max} of k-bit 1-D source labeling in sections $\lfloor \frac{k-1}{2} \rfloor$ and $\lfloor \frac{k-1}{2} \rfloor + 2$ of

k-bit 1-D source labeling, as well as $2^{\lfloor \frac{k}{2} \rfloor}$ such points in section $\lfloor \frac{k-1}{2} \rfloor + 1$ of k-bit 1-D source labeling, since it is true for $k = 4$ as we just proved for k being odd. As stated in the proof of Lemma 4, subsection $(\lfloor \frac{k}{2} \rfloor)_1$ of $k+1$-bit 1-D source labeling is identical to section $\lfloor \frac{k-1}{2} \rfloor$ of k-bit 1-D source labeling, if we discard the "1" value MSB of the former. Additionally, subsection $(\lfloor \frac{k}{2} \rfloor + 1)_1$ of $k+1$-bit 1-D source labeling is identical to section $\lfloor \frac{k-1}{2} \rfloor + 1$ of k-bit 1-D source labeling, if we discard the "0" value MSB of the former.

Since the points whose d_{pmax} equal d_{max} of k-bit 1-D source labeling are located in section $\lfloor \frac{k-1}{2} \rfloor$, section $\lfloor \frac{k-1}{2} \rfloor + 1$, and section $\lfloor \frac{k-1}{2} \rfloor + 2$ of k-bit 1-D source labeling respectively, and $\begin{pmatrix} k \\ \lfloor \frac{k}{2} \rfloor + 1 \end{pmatrix} > \begin{pmatrix} k \\ \lfloor \frac{k}{2} \rfloor \end{pmatrix} > \begin{pmatrix} k \\ i \end{pmatrix}$, with $0 \leq i \leq \lfloor \frac{k}{2} \rfloor$, by Lemma 4, there are $2^{\lfloor \frac{k+1}{2} \rfloor - 1}$ points whose d_{pmax} equal d_{max} of $k+1$-bit 1-D source labeling in subsection $(\lfloor \frac{k}{2} \rfloor)_1$ and subsection $(\lfloor \frac{k}{2} \rfloor + 1)_1$ of $k+1$-bit 1-D source labeling respectively. Due to symmetry, there are $2^{\lfloor \frac{k+1}{2} \rfloor - 1}$ points whose d_{pmax} equal d_{max} of $k+1$-bit 1-D source labeling in subsections $(\lfloor \frac{k}{2} \rfloor + 1)_0$ and $(\lfloor \frac{k}{2} \rfloor + 2)_0$ of $k+1$-bit 1-D source labeling respectively.

Thus we proved that the claims in Theorem 2 are correct for $n = k+1$, if they are correct for $n = k$. With the special cases of $n = 2$ and $n = 3$, the claims in Theorem 2 are correct for any integer $n \geq 2$. $\square$

3.6.3 Proof of Corollary 1

Proof: We first prove that the inequality (3.12) is true. Then, by adding the inequality (3.12) to the inequality (3.8), we can easily prove that the inequality (3.8) is true for $n = j+1$, if we assume it is true for $n = j$.

When k is an odd number, since $\begin{pmatrix} k \\ i \end{pmatrix} = \begin{pmatrix} k \\ k-i \end{pmatrix}$ for $0 \leq i \leq k$,

$$2^k = \sum_{i=0}^{k} \begin{pmatrix} k \\ i \end{pmatrix} = 2 \sum_{i=0}^{\lfloor \frac{k}{2} \rfloor} \begin{pmatrix} k \\ i \end{pmatrix} \geq 2 \begin{pmatrix} k \\ \lfloor \frac{k}{2} \rfloor \end{pmatrix} \tag{3.10}$$

So, we have $\begin{pmatrix} k \\ \lfloor \frac{k}{2} \rfloor \end{pmatrix} \leq 2^{k-1}$.

When k is an even number, $k \geq 2$,

$$2^k = \sum_{i=0}^{k} \begin{pmatrix} k \\ i \end{pmatrix} = 2 \sum_{i=0}^{\lfloor \frac{k-1}{2} \rfloor} \begin{pmatrix} k \\ i \end{pmatrix} + \begin{pmatrix} k \\ \lfloor \frac{k}{2} \rfloor \end{pmatrix} \tag{3.11}$$

Since $\begin{pmatrix} k \\ i \end{pmatrix} \geq \begin{pmatrix} k-1 \\ i \end{pmatrix}$ for $0 \leq i \leq \lfloor \frac{k}{2} \rfloor - 1$, and $k \geq 2$, $\begin{pmatrix} k \\ \lfloor \frac{k}{2} \rfloor \end{pmatrix} = 2^k - 2 \sum_{i=0}^{\lfloor \frac{k-1}{2} \rfloor} \begin{pmatrix} k \\ i \end{pmatrix} \leq 2 \cdot 2^{k-1} - 2 \sum_{i=0}^{\lfloor \frac{k-1}{2} \rfloor} \begin{pmatrix} k-1 \\ i \end{pmatrix} = 2^{k-1}$. Thus, for positive integer k,

$$\begin{pmatrix} k \\ \lfloor \frac{k}{2} \rfloor \end{pmatrix} \leq 2^{k-1} \tag{3.12}$$

For $n = 2$ and 3, the left hand side of (3.8) equals the right hand side of (3.8).

Assume inequality (3.8) holds for $n = j$. Add inequality (3.12) for $k = j$ to inequality (3.8), we proved that inequality (3.8) holds for $n = j + 1$. Thus, inequality (3.8) holds for any integer $n \geq 2$. $\square$

Chapter 4

A Data Fusion Model and its Application in Multiuser Detection Using Successive Interference Cancellation in DS/CDMA Systems

4.1 Introduction of Chapter 4

Decentralized detection and estimation has attracted recent interest. In classical multi-sensor detection and estimation, it is assumed that all local sensors transmit all of their data to a central processing center that performs optimal detection and tracking of targets based on conventional statistical techniques. However, in decentralized detection and estimation, some preliminary local processing of data (often lossy compression) is carried out at each sensor. The condensed information is sent from each sensor, maybe via other sensors, to the central processor which is often known as fusion center. In the terminology of distributed sensor networks, we say that the network has intelligence at each node [31].

Some of the advantages of distributed signal processing schemes are reduced communication bandwidth, increased reliability, and reduced cost. In addition, a distributed system architecture may yield a better response to rapid changes in background scenario. Unlike the central processor in centralized systems, the fusion center of a decentralized system has only partial information as communicated by the sensors. This results in a loss of performance in decentralized systems as compared to centralized systems. However, the performance loss can be made small by optimally processing the information at the sensors [32].

In wireless sensor networks, the local sensors send information with finite precision to the fusion center, and the fusion center makes the final decisions based on these information. To reduce the power consumption in each sensor, the number of bits of information sent by the sensors to the fusion center needs to be as small as possible. There is always tradeoff between the precision of the information and the system performance, i.e. the probability of error. The design of local processing in every sensor and the fusion rule in the fusion center to achieve global optimal performance is a challenging research problem. In [2], we studied a binary fusion distributed detection with the assumption of identical sensors with AWGN channels. In this chapter, we consider the case of a binary fusion distributed detection with the assumption of identical sensors with fading channels.

In distributed multi-sensor detection systems, sensor SNR is usually time varying, and it is different from sensor to sensor. Let us consider the case in a battlefield where a military airplane is spreading dozens of identical sensors on an open area to detect the movement of military vehicles. Before a sensor lands on a specific spot, and as vehicles are moving, the exact SNR of that sensor at time t is, in general, unknown. However, we might know the distribution of the SNR in practical cases, which is equivalent to the case we might know the fading channels between the sensors and the fusion center.

We present our model by finding the optimal threshold τ for local sensors in the distributed detection of $s \in \{-1, 1\}$, where the ith of n local sensors observes $x_i = s + z_i$ with z_i i.i.d. $\sim \mathcal{N}(0, m^{-2})$. The positive random variable m has a pdf $g(m)$. The fusion center makes a decision based on the n local binary decisions. To make analysis easier, we consider the case that signal s is either m or $-m$ with pdf $g(m)$, where the ith of n local sensors observes $x_i = s + z_i$ with z_i i.i.d. $\sim \mathcal{N}(0, 1)$. The ith sensor compares x_i to a threshold τ to compute a binary decision u_i as

$$u_i = \begin{cases} 0 & \text{when } x_i < \tau \\ 1 & \text{when } x_i \geq \tau. \end{cases}$$

Next, each u_i is transmitted to a fusion center and the fusion center applies a fusion rule F to the sum $k = \sum_{i=1}^{n} u_i$ to produce the final decision $F(k)$. The system with constant m is analyzed in detail in [33]. The first half of this chapter studies the variable SNR model with a positive random variable m of pdf $g(m)$ and describes a technique for identifying the pair (τ, F) that minimizes the probability of error.

The problem is complicated by the existence of multiple local minima. Furthermore, minimizing probability of error is difficult because the Bayesian error probability is a discontinuous function. Hashlamoun and Varshney [34, 35] have overcome this difficulty by using a continuous bound on the Bayesian error probability to approximately determine the optimal pair (τ, F). Avi-Itzhak and Diep [36] have provided an even tighter bound leading to a very good approximation. Even so, these techniques still produce a minimization problem that has local minima.

In this chapter we show that for any admissible fusion rule F (i.e., any F that is optimal for at least one τ), the probability of error is a quasi-convex function of τ. The admissible functions F are simply threshold tests of the form

$$s = F_i(k) = \begin{cases} -m & \text{if } k < i \\ m & \text{if } k \geq i. \end{cases} \tag{4.1}$$

Hence, the problem decomposes into a series of n quasi-convex optimization problems (one for each F_i) that may be solved exactly using a variety of techniques including, for example, the ellipsoid algorithm [37]. The concept of quasi-convexity eliminates the existence of multiple local [38] optima .

We have used this technique to identify the optimal (τ, F) pairs for a variety of cases, and extensive observations suggest that the optimal F is always essentially majority vote. If $p(s = -m) = 0.5$ and n is odd, the optimal pair is $(0, F_{(n+1)/2})$. If $p(s = -m)$ is not 0.5, the optimal threshold can be identified by solving only n quasi-convex equations.

Based on our distributed detection model, we present a multiuser detection scheme with successive interference cancellation. In code division multiple-access (CDMA) systems, multiple users transmit, often asynchronously, over a common communication channel, typically using the direct sequence spread spectrum technique. There are two most important factors that limit the capacity of a multiuser DS/CDMA system: multiple access interference (MAI) resulting from signals of different users transmitted simultaneously, and the near-far effect due to a difference in distance between the users and the base station. Recently, much research has been focused on the subject of multiuser detection which can mitigate the near-far effect and cancel MAI [39, 40].

Generally, a major problem with multiuser detectors and interference cancelers is the maintenance of simplicity. In Section 4.4 we present a simple multiuser detector adding only one fusion delay to the computational delay requirements of conventional SIC.

4.2 Theory Concerning the Distributed Detection Model

Let us define

$$A_k(\tau) = \frac{1}{2}\binom{n}{k} Q_P^k(\tau) Q_P^{n-k}(-\tau)$$

and

$$B_k(\tau) = \frac{1}{2}\binom{n}{k} Q_N^k(\tau) Q_N^{n-k}(-\tau)$$

where $A_k(\tau)$ ($B_k(\tau)$) is the probability that k sensors decide 1 and $n-k$ sensors decide 0 while $s = -m$ ($s = m$).

Let $Q(x) = \frac{1}{\sqrt{2\pi}} \int_x^\infty e^{-\frac{t^2}{2}} dt$. $Q_P(\tau) = \int_m Q(\tau + m) g(m) dm$ be the probability of false alarm and $Q_N(\tau - m) = \int_m Q(\tau - m) g(m) dm$ be the probability of detection.

Lemma 5 *Under the maximum a posteriori probability (MAP) criterion, the optimal F for a fixed τ has the following property: if $F(k) = -m$, then $F(k-1) = -m$ and if $F(k) = m$, then $F(k+1) = m$.*

Proof: Under the MAP criterion and the equal *a-priori* probability assumption, $F(k) = -m$ implies that

$$A_k(\tau) \geq B_k(\tau) \tag{4.2}$$

and also,

$$\frac{A_{k-1}(\tau)}{B_{k-1}(\tau)} = \frac{A_k(\tau)}{B_k(\tau)} \frac{Q_N(\tau) Q_P(-\tau)}{Q_P(\tau) \hat{Q_N}(-\tau)} \geq \frac{A_k(\tau)}{B_k(\tau)} \tag{4.3}$$

As a consequence of inequalities (4.2) and (4.3), $A_{k-1}(\tau) \geq B_{k-1}(\tau)$, which implies that $F(k-1) = -m$. Similarly,
if $F(k) = m$, then $F(k+1) = m$. $\square$

Theorem 3 *Only fusion rules of the form F_i in (4.1) are admissible, i.e., are MAP for some choice of τ.*

Proof: Lemma 5 implies that for every τ the MAP F has the form F_i in (4.1). $\square$

Claim 1 *Define*

$$D(\tau) = \frac{\int_m Q'(\tau - m)g(m)dm}{\int_m Q'(\tau + m)g(m)dm} \tag{4.4}$$

$D(\tau)$ is monotonically increasing for $\tau \in (-\infty, +\infty)$. And, $D(+\infty) \to +\infty$.

Proof: Define

$$\begin{aligned} K(\tau) = & \int_m Q'(\tau + m)g(m)dm \int_m Q''(\tau - m)g(m)dm \\ & - \int_m Q'(\tau - m)g(m)dm \int_m Q''(\tau + m)g(m)dm \end{aligned} \tag{4.5}$$

Since

$$Q''(x) = -xQ'(x)$$

$$\begin{aligned} K(\tau) &= \int_m Q'(\tau + m)g(m)dm \int_m (m - \tau)Q'(\tau - m)g(m)dm \\ &- \int_m Q'(\tau - m)g(m)dm \int_m (-m - \tau)Q'(\tau + m)g(m)dm \\ &= \int_m Q'(\tau + m)g(m)dm \int_m m \cdot Q'(\tau - m)g(m)dm \\ &+ \int_m Q'(\tau - m)g(m)dm \int_m m \cdot Q'(\tau + m)g(m)dm \end{aligned}$$

for any $m > 0$, and any τ, $K(\tau) > 0$. Thus $D(\tau)$ is monotonically increasing for $\tau \in (-\infty, +\infty)$, since

$$D'(\tau) = \frac{1}{[\int_m Q'(\tau + m)g(m)dm]^2} K(\tau) \tag{4.6}$$

and $Q(x)$ is monotonically decreasing.

$$D(+\infty) = \lim_{\tau \to +\infty} \frac{\int_m Q'(\tau - m)g(m)dm}{\int_m Q'(\tau + m)g(m)dm} \tag{4.7}$$
$$= \lim_{\tau \to +\infty} \frac{\int_m e^{\tau m} e^{-\frac{m^2}{2} g(m)} dm}{\int_m e^{-\tau m} e^{-\frac{m^2}{2} g(m)} dm} \to +\infty$$

□

Claim 2 *For any $m > 0$, and any τ, $Q_N(\tau) > D(\tau) \cdot Q_P(\tau)$.*

Proof: Since for any $m > 0$, and any τ, $Q(\tau - m) > Q(\tau + m)$,

$$\int_m Q(\tau - m)g(m)dm > \int_m Q(\tau + m)g(m)dm. \tag{4.8}$$

For $\tau \leq 0$, we have $D(\tau) \leq 1$. Thus inequality (4.8) holds. Define

$$H(\tau) = \int_m Q(\tau - m)g(m)dm - \int_m Q(\tau + m)g(m)dm \cdot D(\tau) \tag{4.9}$$

$$H'(\tau) = -\int_m Q(\tau + m)g(m)dm \cdot D'(\tau) < 0 \tag{4.10}$$

So, for any τ, inequality (4.8) holds. □

Claim 3 $\left(\frac{Q_N(\tau)}{Q_P(\tau)}\right)^k$ *is monotonically increasing for $\tau \in (-\infty, +\infty)$, where $k = 1, 2, \cdots$*

Proof:

$$\frac{\partial}{\partial \tau}\left(\frac{Q_N(\tau)}{Q_P(\tau)}\right) = -\frac{Q'_N(\tau)[Q_N(\tau) - Q_P(\tau)] \cdot D(\tau)}{Q_P(\tau)^2} \tag{4.11}$$
$$> 0$$

due to Claim 2. So, for positive integer k, $\left(\frac{Q_N(\tau)}{Q_P(\tau)}\right)^k$ is monotonically increasing for $\tau \in (-\infty, +\infty)$. Replacing τ by $-\tau$, $\left(\frac{Q_P(-\tau)}{Q_N(-\tau)}\right)^k$ is monotonically decreasing for $\tau \in (-\infty, +\infty)$ $\Box$

Theorem 4 *For a fixed admissible fusion rule F_i, the probability of error is a quasi-convex function of τ.*

Proof: Define $P_e(\tau, i)$ as the probability of error for (τ, F_i). $P_e(\tau, i)$ can be expressed as

$$P_e(\tau, i) = \frac{1}{2} + \sum_{k=0}^{i-1} (B_k(\tau) - A_k(\tau)) \tag{4.12}$$

where $i = 1, 2, \cdots, n$.

With the facts that

$$\binom{n}{k}(n-k) = \binom{n}{k+1}(k+1)$$

and

$$Q_N{}'(\tau) = Q_P{}'(\tau) D(\tau)$$

the derivative of $P_e(\tau, i)$ is a telescoping sum (i.e., has the form $\sum_{k=0}^{i-1}(f_k(\tau) - f_{k-1}(\tau))$ for a specific $f_k(\tau)$):

$$\frac{\partial B_k(\tau,m)}{\partial \tau} = \begin{pmatrix} n \\ k \end{pmatrix} k{Q_N}^{k-1}(\tau){Q_N}^{n-k}(-\tau)Q'_N(\tau)$$

$$- \begin{pmatrix} n \\ k \end{pmatrix} (n-k){Q_N}^{k}(\tau){Q_N}^{n-k-1}(-\tau)Q'_N(\tau)$$

$$= \begin{pmatrix} n \\ k \end{pmatrix} k{Q_N}^{k-1}(\tau){Q_N}^{n-k}(-\tau)Q'_N(\tau)$$

$$- \begin{pmatrix} n \\ k+1 \end{pmatrix} (k+1){Q_N}^{k}(\tau){Q_N}^{n-k-1}(-\tau)\hat{Q'_N}(\tau)$$

So, $P'_e(\tau, i)$ can be simplified to

$$P'_e(\tau, i) = \alpha(\tau)(\beta(\tau) - \gamma(\tau)) \tag{4.13}$$

where

$$\alpha(\tau) = \frac{1}{2}\begin{pmatrix} n \\ i \end{pmatrix} i|{Q_P}'(\tau)|{Q_P}^{i-1}(\tau){Q_N}^{n-i}(-\tau)$$

$$\beta(\tau) = D(\tau)\left(\frac{Q_N(\tau)}{Q_P(\tau)}\right)^{i-1}$$

$$\gamma(\tau) = \left(\frac{Q_P(-\tau)}{Q_N(-\tau)}\right)^{n-i}$$

Clearly, $\alpha(\tau)$ is always positive, $\beta(\tau)$ is a positive and monotonically increasing function and $\gamma(\tau)$ is a positive and monotonically decreasing function because of Claim 1, Claim 2 and Claim 3. Furthermore $\beta(-\infty) = 0 < \gamma(-\infty) =$

$D(+\infty)^{n-i} \to +\infty$ and $\beta(\infty) = D(+\infty)^i \to +\infty > \gamma(\infty) = 1$. Therefore $P_e'(\tau, i) = 0$ for only one τ^*, for which $\beta(\tau^*) = \gamma(\tau^*)$. For $\tau < \tau^*$ we have $P_e'(\tau, i) < 0$ and for $\tau > \tau^*$ we have $P_e'(\tau, i) > 0$. Hence $P_e(\tau, i)$ is quasi-convex. $\square$

Figure 4.1 presents a numerical example of quasi-convex probability of error vs. τ curves for the admissible fusion rules F_i.

The problem of distributed binary hypothesis testing with multiple sensors has been extensively studied in the last decade. The optimal decision rules are likelihood ratio threshold tests. Nevertheless it is difficult to determine the thresholds, and to implement when the variables are in ratio test space since a faster divider is difficult to build in integrated circuits. On the other hand, received signals are in observation space in most communication receivers. Therefore, a slicer test dealing with variables in the observation space is very popular in communication systems. We derive a necessary and sufficient condition for the slicer test to be optimal, and verify that the slicer test is optimal under the condition that received signals passed through a Rayleigh fading channel with AWGN.

Theorem 5 *Consider a communication system that the transmitted BPSK signal passes an additive noise channel before it arrives the receiver, where the pdf of the noise is $f(x)$. A slicer demodulates the received signal. The necessary and sufficient condition that slicer is optimal is that $ln(f(x))$ concave down.*

Proof: It is known that Likelihood Ratio Test (LRT) is optimal, and continuous Receiver Operating Characteristic (ROC) concave down. It is also known that ROC passes (0,0) and (1,1) on P_d vs.P_f plane, and $\lambda = \frac{dP_d}{dP_f}$.

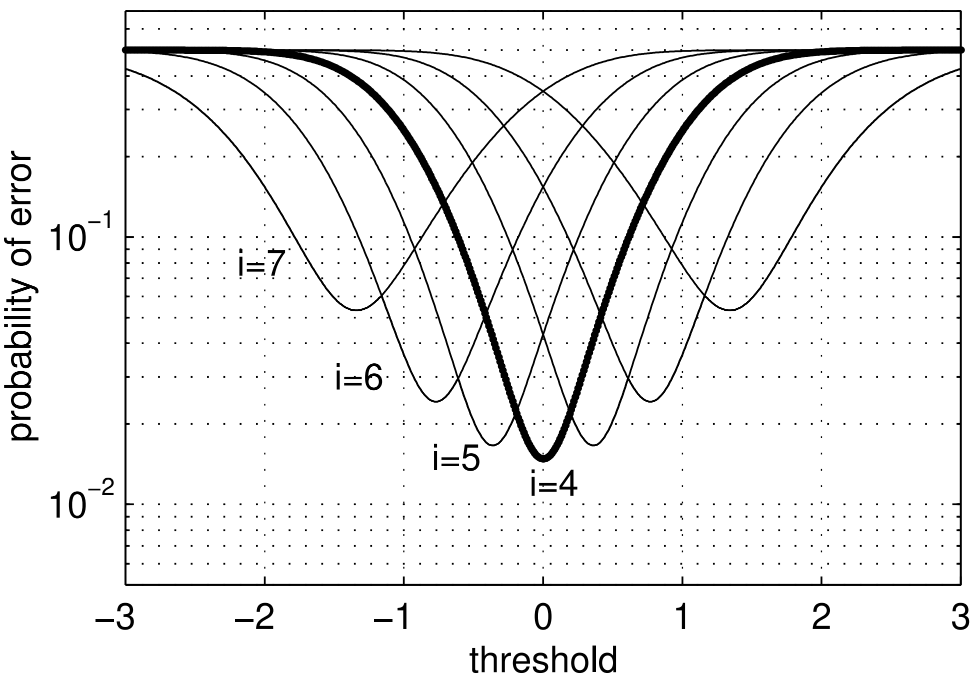

Figure 4.1: $P_e(\tau, i)$ vs. τ for various i with 7 sensors. The optimal pair is $(0, F_4)$. $m = 1.0$.

If the slicer test is optimal, then $Z_0 \in (-\infty, \tau)$, $Z_1 \in (\tau, +\infty)$, and λ and τ are one-to-one mapping. Z_i is the observation space of H_i, $i = 0, 1$. Also,

$P_d(\tau) = \int_{\tau}^{+\infty} p_1(x)dx$, $P_f(\tau) = \int_{\tau}^{+\infty} p_0(x)dx$. For additive noise with pdf $f(x)$, $p_1(\tau) = f(\tau - m)$, and $p_0(\tau) = f(\tau + m)$ where $m > 0$ is the amplitude of BPSK signal. So, $\frac{dP_f(\tau)}{d\tau} = -p_0(\tau) < 0$ and $\frac{d\lambda(\tau)}{dP_f(\tau)} < 0$. Then, $\frac{d\lambda(\tau)}{d\tau} < 0$ which is equivalent to $\frac{f'(\tau-m)}{f(\tau-m)} > \frac{f'(\tau+m)}{f(\tau+m)}$ where $\tau \in (-\infty, +\infty)$. With arbitrary positive m, We have $(\frac{f'(\tau)}{f(\tau)})' < 0$ which means $ln(f(\tau))$ concave down.

If $ln(f(\tau))$ concave down, then $(ln(f(\tau)))'' < 0$ which means $(\frac{f(\tau-m)}{f(\tau-m)})' > 0$. Thus $\frac{f(\tau-m)}{f(\tau-m)}$ monotonically increases over τ.

Consider the Bayes cost function:

$$\begin{aligned} R =& P_0 c_{10} + P_1 c_{11} + \int_{Z_0} \{[P_1(c_{01} - c_{11}) Pr_{u|H_1}(U|H_1) - \\ & P_0(c_{10} - c_{00}) Pr_{u|H_0}(U|H_0)]\} dU \end{aligned} \tag{4.14}$$

It is reasonable to assume $c_{10} > c_{00}$, $c_{01} > c_{11}$. So we have

$$R - A = B \int_{Z_0} (\frac{Pr_{u|H_1}(U|H_1)}{Pr_{u|H_0}(U|H_0)} - \frac{C}{B}) Pr_{u|H_0}(U|H_0) dU \tag{4.15}$$

where $A = P_0 c_{10} + P_1 c_{11} > 0$, $B = P_1(c_{01} - c_{11}) > 0$, and $C = P_0(c_{10} - c_{00}) > 0$

If we choose $Z_0 \in (-\infty, \tau)$, $Z_1 \in (\tau, +\infty)$, then

$Pr_{u|H_1}(U|H_1) = f(\tau - m)$, and $Pr_{u|H_0}(U|H_0) = f(\tau + m)$. For any B_0, C_0, there is one and only one τ_0 minimize $R - A$, since $\frac{f(\tau-m)}{f(\tau+m)}$ monotonically increases over τ. As a result, such Z_0, Z_1 uniquely lead to optimal LRT. With $\lambda(\tau) = \frac{f(\tau-m)}{f(\tau+m)}$ monotonically increases over τ, λ and τ are one one mapping, and the slicer test is optimal. $\square$

With Theorem 5, it can be easily proved that in the above model, with a binary symmetric channel between sensor i and the fusion center, each $P_e(\tau, n)$

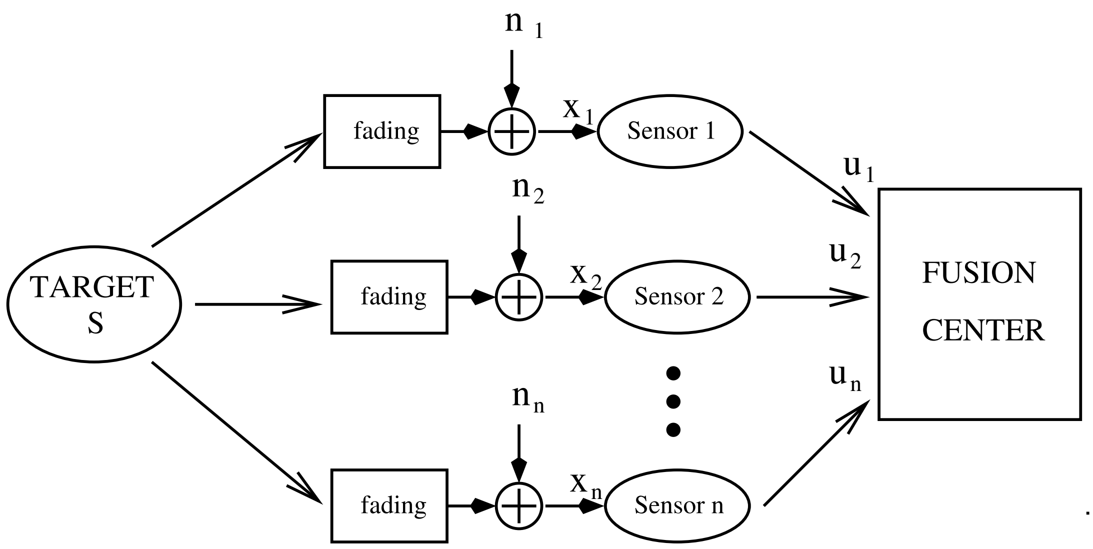

Figure 4.2: Proposed distributed detection model with on tap fading channels between target and sensors.

vs. τ curve in Fig. 4.2 is quasi-convex if $ln(f(x))$ is concave down, where τ is the detection threshold of every sensor and n is the number of i.i.d. sensors.

The following example is a special case of the proposed model.

Example 1:

In this example, we consider the parallel data fusion model in Fig. 4.2. The target signal is BPSK with amplitude of m. The additive noise is i.i.d. $\sim \mathcal{N}(0, 1)$. The fading channel between the target and sensor i is a one tap Rayleigh fading channel with pdf of $g(\alpha) = 2\alpha e^{-\alpha^2}, \alpha > 0$. The channel between sensor i and the fusion center is a perfect channel.

$$P_D(\tau,m) = \int_0^{+\infty} Q(\tau-\alpha m)g(\alpha)d\alpha$$
$$= -\int_0^{+\infty} Q(\tau-\alpha m)de^{-\alpha 2}$$
$$= Q(\tau) + \frac{m}{\sqrt{m^2+2}}e^{-\frac{\tau^2}{m^2+2}}Q(-\frac{\tau m}{\sqrt{m^2+2}}) \tag{4.16}$$

Similarly

$$P_F(\tau,m) = Q(\tau) - \frac{m}{\sqrt{m^2+2}}e^{-\frac{\tau^2}{m^2+2}}Q(\frac{\tau m}{\sqrt{m^2+2}}) \tag{4.17}$$

It is obvious that P_D and P_F monotonically decreasing over τ. So λ and τ are one-to-one mapping. Hence the slicer test is optimal in this case. The $P_e(\tau,i)$ vs. τ curve with $p_0 = p_1 = 0.5$ is plotted in Fig. 4.3. With the $m = 1.0$, the global minimum of $P_e(\tau)$ occurs at $\tau = 0$ with the majority vote fusion rule.

$$P_e(0,2l+1) = \frac{1}{2}\sum_{k=l+1}^{2l+1} A_k(0,m) + \frac{1}{2}(1-\sum_{k=l+1}^{2l+1} B_k(0,m)) \tag{4.18}$$

4.3 Hard and Soft Data-Fusion-Based SIC System Model

Successive interference cancellation schemes can be described by defining an interference canceling unit (ICU) as in Fig. 4.4. Then it can be used to build the conventional SIC and multi-stage SIC shown in [41]. In Fig. 4.5 we present the hard and soft data-fusion-based SIC scheme. The received signal $r_i(t)$ might be from a single antenna or from multiple antennas.

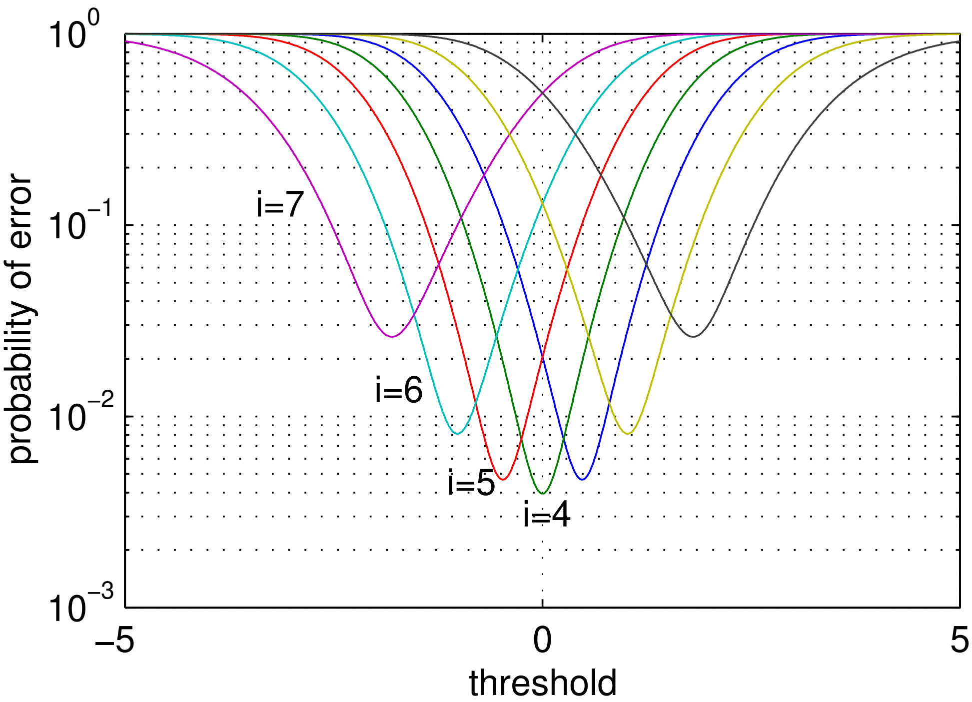

Figure 4.3: $P_e(\tau, i)$ vs. τ for various i with 7 sensors. The optimal pair is $(0, F_4)$. $m = 1.0$. $g(\alpha) = 2\alpha e^{\alpha^{-2}}$

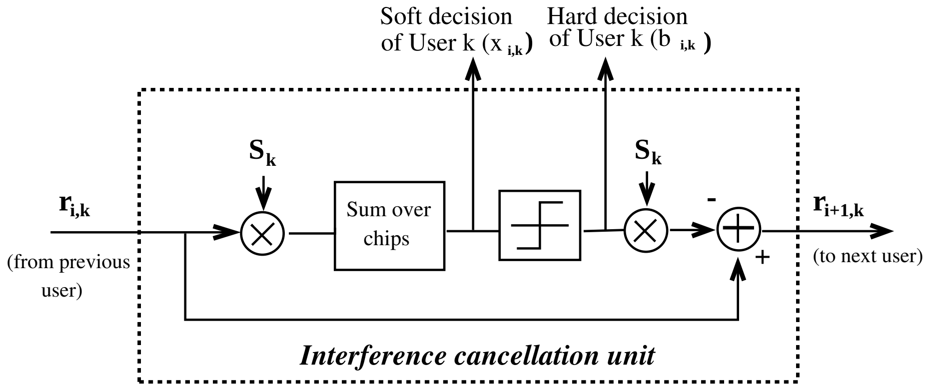

Figure 4.4: Interference cancellation unit. Both soft decision and hard decision can be used as data fusion input to enhance performance.

In hard data-fusion-based successive interference canceler (DFSIC), we select $\tau = 0$ as the detection threshold for the odd number of data fusion paths with majority vote fusion rule since it seems that the probability of error has a global minimum at $\tau = 0$ with odd number of fusion. In conventional SIC, the detection threshold of a slicer is also at $\tau = 0$ which has the simplest implementation. It is well known that the maximum ratio combining method is optimal since the fused soft decision is a sufficient statistic. But in a lot of cases, estimating SNR will be either very difficult or complicated. We use equal gain combining as our soft fusion rule. The number of fusion paths could be either an even or odd positive integer.

By taking advantage of space diversity and order diversity, our proposed SIC structure has better performance than that of the conventional SIC.

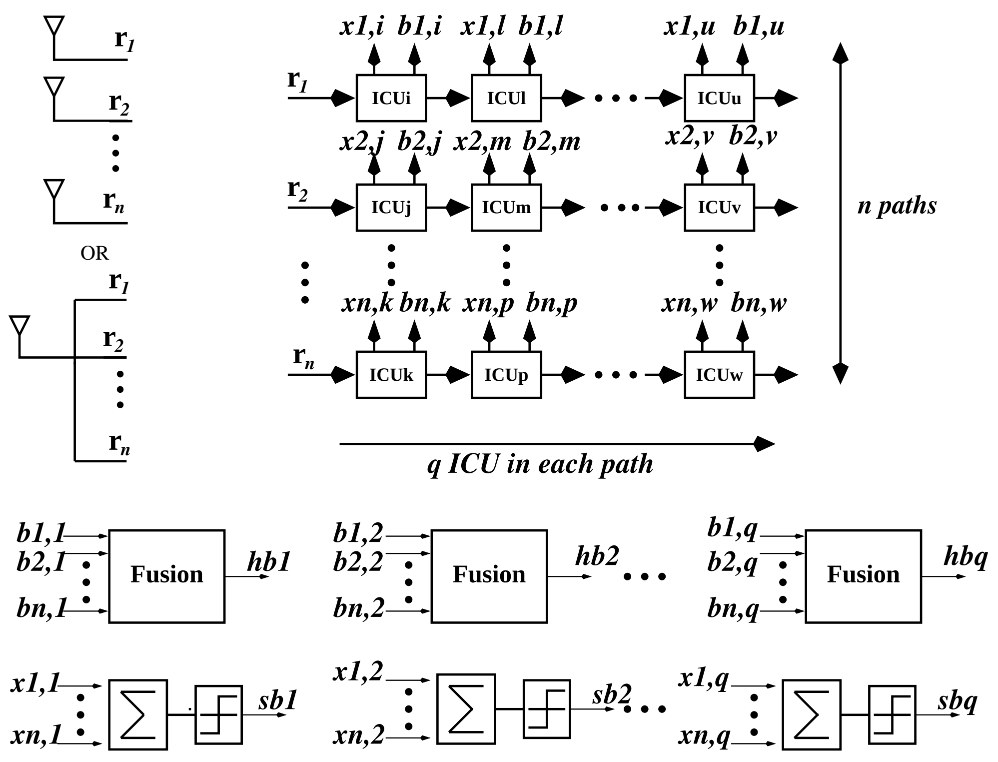

Figure 4.5: Proposed soft decision and hard decision data fusion based successive interference canceler.

4.4 Data-Fusion-Based Successive interference canceler (DFSIC) and Simulation Result

Direct sequence code division multiple access (DS/CDMA) has attracted great attention in recent years. However, the capacity of a DS/CDMA system is severely limited by the multiple access interference (MAI) caused by other users using the same frequency band. The effect of MAI is more serious when coupled with a near-far problem which results in difficulties in decoding signals due to their spread in received power caused by different propagation path losses. It is important to realize that the elimination of unwanted signals is not restricted to the processing gain of the spreading codes, since the interference signals are not unpredictable jammers and totally unknown to the receiver. Actually, their coding is completely known in the CDMA system. A lot of research has been focused on the subject of multiuser detection which can mitigate the near-far effect and cancel MAI [39, 40, 42]. In CDMA systems, multiple users transmit, often asynchronously, over the uplink channel to the base station. We present a successive interference cancellation multiuser detection scheme utilizing space diversity and order diversity based on a data fusion model we proposed in this chapter. Generally, a major problem with multiuser detectors and interference cancelers is the maintenance of simplicity. The data fusion based SIC we present in this chapter enhances the system performance with very limited increase in complexity. Only one small fusion delay is added compared to conventional SIC.

We consider the coherent BPSK modulation as in [40], where the received signal is

$$r(t) = \sum_{k=1}^{K} A_k a_k(t-\tau_k) b_k(t-\tau_k) \cos(\omega_c t + \Phi_k) + n(t) \tag{4.19}$$

$$\begin{aligned}
r(t) &= \text{received signal} \\
K &= \text{total number of active users} \\
A_k &= \text{amplitude of } k^{th} \text{ user} \\
b_k(t) &= \text{bit sequence of } k^{th} \text{ user at bit-rate } R_b \\
a_k(t) &= \text{spreading chip sequence of } k^{th} \text{ user at chip-rate } R_c \\
n(t) &= \text{additive white Gaussian noise} \\
&\quad \text{(two sided power spectral density} = N_0/2) \\
N &= T/T_c \text{ where } T = \text{bit period and } T_c = \text{chip period}
\end{aligned}$$

τ_k and Φ_k are the time delay and phase of the k^{th} user, which are assumed to be known, i.e., tracked accurately.

The bits and chips are rectangular waveforms. Their values are all i.i.d. random values with probability 0.5 of being either 1 or -1. For the asynchronous case, the τ_k and Φ_k are i.i.d. uniform random variables in $[0, T]$ and $[0, 2\pi]$ respectively.

The model we propose in this chapter for analyzing the hard decision fused SIC is a distributed detection model with a parallel fusion network (Figure 4.2). The channel between the target and sensor i is a one tap fading channel. We proved that for a given K-out-of-N fusion rule, the probability of error is quasi-convex if $ln(f(x))$ is concave down, where $f(x)$ is the pdf of the additive noise.

The system without a fading channel is analyzed in detail in [33] showing that each $P_e(\tau, i)$ vs. τ curve is quasi-convex, and the global minimum of P_e

can be found through n quasi-convex optimizations. The quasi-convex result is extended to the variable SNR case at the beginning of this chapter. In [43], Zhang, Varshney and Wesel generalized observation distribution in likelihood ratio space instead of observation space. In their result, a perfect channel between sensors and the fusion center is assumed.

The conventional SIC detects and cancels the users sequentially, in the order of their power. In DFSIC, we use an odd number (n=3, 5, $\cdots$) of identical conventional SIC paths. Among these paths, only one path has the same user order as that of conventional SIC, while the other $n-1$ paths have randomly selected user orders. All n paths process in parallel. The final detection of user i, for $i = 0, 1, \cdots, K-1$, is parallelly decided by a majority vote of detections for user i from n independent paths for all K users. In this way, only one small fusion delay is added. The DFSIC structure is just a parallel array of conventional SIC processors, which is straightforward for VLSI implementation. The only added circuits are n parallel majority-vote circuits. From Figure 4.6, it is evident that in 3-path fusion, the BER decreases significantly, while in 5-path fusion the BER doesn't decrease much from 3-path fusion's performance. This suggests that 3-path DFSIC should be the best choice from an economic point of view.

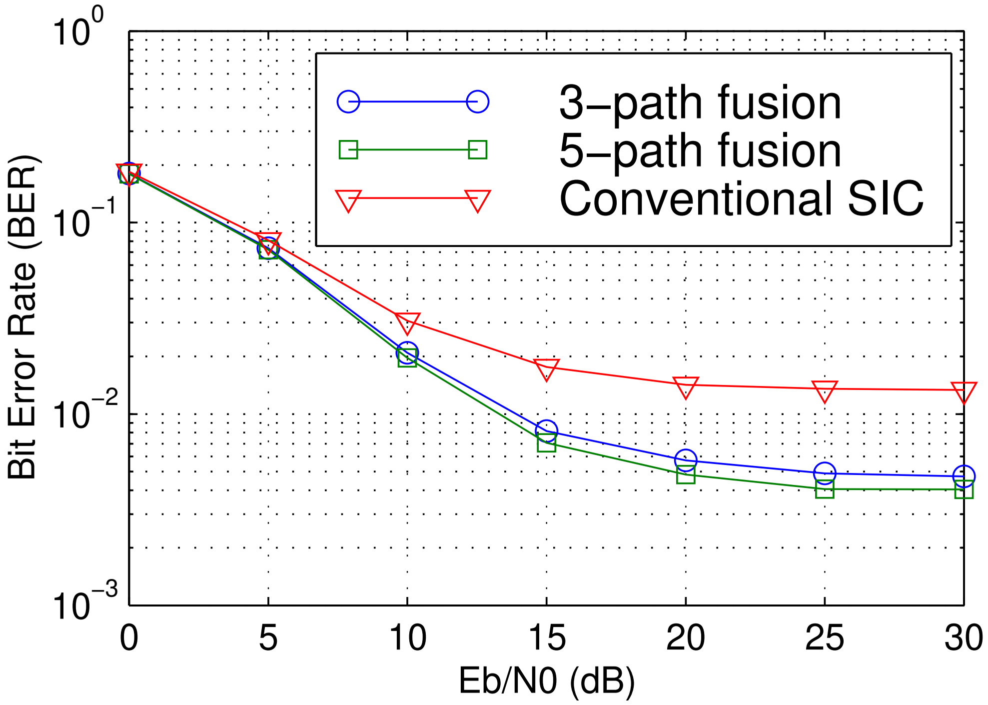

Figure 4.6: BER vs E_b/N_0 under ideal power control, 20 active users. Processing gain of 31, asynchronous AWGN channel.

Based on the simulation of our distributed detection model, we selected $\tau = 0$ as the detection threshold for our odd number of detection DFSIC to achieve a low bit error rate as in Figure 4.7. Note that interference and noise for user i in DFSIC is no longer i.i.d. In fact, most practical data fusion systems experience correlated noise. That is why we can see the performance degraded, comparing Figure 4.7 and Figure 4.6. The reason why, in 5-path DFSIC, the BER cannot decrease significantly from that in 3-path DFSIC is that the interference and noise are correlated, and 3-path DFSIC has corrected most detection errors caused by the uncorrelated part of the interference and noise. If the signal to interference and noise ratio is extremely low or high, or if the correlation of interference and noise is very close to one, data fusion cannot improve performance. This explains why DFSIC decreases BER significantly for high E_b/N_0 in Fig. 4.6. DFSIC cancels more interference than noise.

We simulated the bit error rate of DFSIC for n=3 and n=5 with an asynchronous AWGN channel under ideal and non-ideal power control. In our non-ideal power control case, the amplitude of every user's signal at the receiver is uniformly distributed from its peak value to 2/3 of peak value, i.e., a 3 dB difference in worst case. The Gold sequence with processing gain (or period) of 31 is used as the spreading sequence. Our simulation of multistage SIC shows that data-fusion-based multistage SIC outperforms conventional multistage SIC [42].

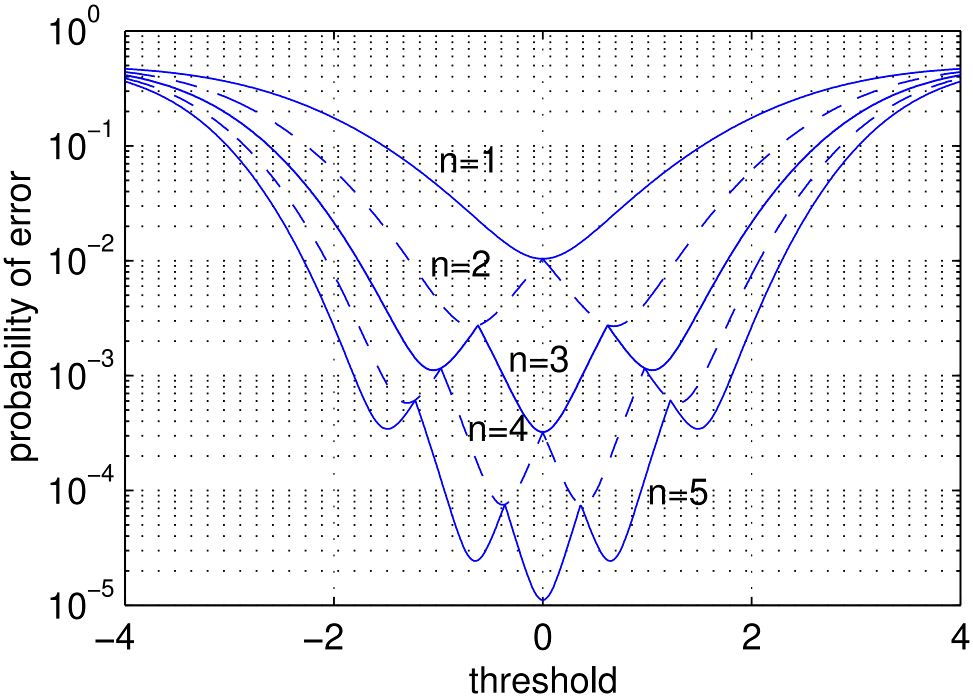

Figure 4.7: $P_e(\tau, n)$ vs. τ for $n = 1, 2, 3, 4$, and 5. The optimal pair for odd n is $(0, F_n)$. $p(m = 2.0, 2.2, 2.4, 2.6, 2.8) = 0.2$

According to [39], because of error propagation, it is crucial that data estimates of at least the strong user, that are canceled first, be reliable. We added one more level of fusion for the first user of each of the n SIC paths for this reason. We take the majority-vote of three detection results, of which the first is the direct detection of the first user from the received signal $r(t)$ with a correlator detector, the second is the detection of the first user after the second user is detected and canceled from $r(t)$, and the third is the detection of the first user after the third user is detected and canceled from $r(t)$. In this scheme, one more correlation detection delay is added. Our simulation shows that error propagation does exist but it is not significant, especially in the high E_b/N_0 case.

4.5 Discussions

In this chapter, we have considered a distributed detection model with variable SNR, and we have presented a technique to find the optimal pair (τ, F) that minimizes the probability of error. We have shown that, for any admissible fusion rule, the probability of error is a quasi-convex function of threshold τ. Hence, the problem decomposes into a series of n quasi-convex optimization problems that can be solved by using any of a variety of well-known techniques. As an application of this model, we have presented a multiuser detection scheme with data fusion based successive interference cancellation (DFSIC) for DS/CDMA. Our simulation results for an asynchronous AWGN channel show that DFSIC significantly decreases the bit error rate (BER) from that of conventional SIC. Compared to conventional SIC, DFSIC extends the system delay by just one short fusion time interval. The processing consists of n (typically $n = 3$) identical conventional SIC processors as well as K parallel n-to-1 fusion circuits. For $n = 3$, the 3-to-1 fusion circuit is just a 3-input, single output, combinational logic circuit with a nanosecond delay! The data fusion concept can be added to other existing algorithms and techniques such as multistage SIC with clipped soft-decision (CSD) in [42], etc.

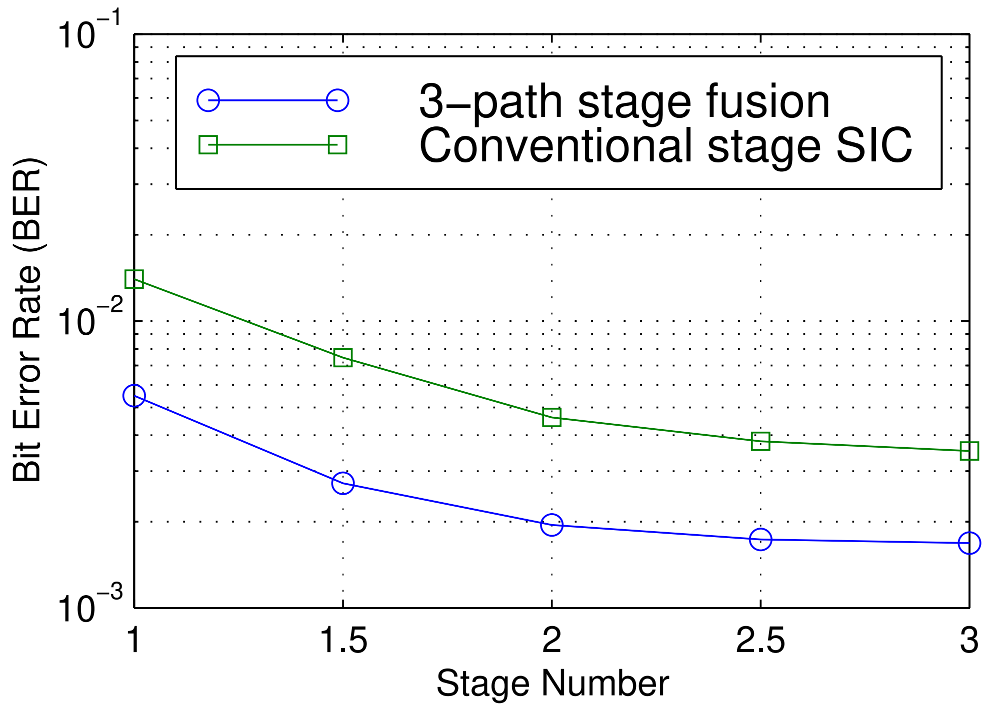

Figure 4.8: BER vs number of stages, ideal power control, 20 active users, E_b/N_0 = 20 dB. Processing gain of 31, asynchronous AWGN channel.

Chapter 5

Conclusion

This dissertation presented several new error protection techniques for wireless communications.

Chapter 2 showed that superposition turbo TCM performs within 1 dB of the achievable capacity region boundary for all two-rate and three-rate schemes we simulated. We designed and simulated two-rate structure with 16-point square constellations and 8-point circular constellations. The three-rate scheme utilizes 64-point square constellations.

Our two-stage decoding of the separate 8-state trellis for 16-QAM presented in this chapter achieves the same performance of joint decoding utilizing 64-state overall trellis. Joint decoding is sixteen-times more complicate than the two-stage decoding of the 8-state trellis.

We proved that multilevel coding is a special case of multi-rate superposition coding with α tuned so that all rates have the same error free SNRs. The proposed schemes offers the same complexity and performance as that of the typical single rate turbo TCM for this power allocation parameter α, but provides the flexibility of controlling unequal error protection through the selection of α.

Chapter 3 shows two lower bounds for a metric d_{max}, and presented the Monotonic-Decreasing-Hamming-Weight (MDHW) labeling for n-bit one-dimension source coding which approaches the lower bound closer than any other labelings examined. The metric d_{max} is defined as the maximum of the Euclidean distance between any two points which are associated with a single bit error.

We derived the closed form expression of d_{max} of MDHW labeling. Total number of points whose d_{pmax} reaches d_{max}, and their brief location in n-bit one-dimension MDHW labeling are also derived. A $2n$-bit (n by n) two-dimension labeling with the direct product of two n-bit one-dimension MDHW labelings will achieve the same d_{max} as that of n-bit one-dimension MDHW labeling.

In Chapter 4, we consider the case that a binary data fusion based distributed detection with the assumption of identical sensors with fading channels. A technique is presented to find the optimal pair (τ, F) that minimizes the probability of error. We also showed that, for any admissible fusion rule, the probability of error is a quasi-convex function of the threshold τ. As a result, the problem decomposes into a series of n quasi-convex optimization problems which can be easily solved by using any of a number of well-known techniques including, for example, the ellipsoid algorithm. In addition, we derived a necessary and sufficient condition when the slicer detection is optimal in Chapter 4.

By applying this distributed detection model in wireless communications, we presented a multiuser detection scheme with data fusion based successive interference cancellation (DFSIC) for direct sequence CDMA systems. Our simulation results for an asynchronous AWGN channel show that DFSIC significantly decreases the bit error rate from that of a typical SIC.

A major advantage of data fusion based successive interference cancellation is that it does not increase complexity and delay significantly.

The data fusion concept can be incorporated in other existing multi-user interference cancellation algorithms, such as multi-stage SIC with clipped soft-decision in [42].

Bibliography

[1] P. P. Bergmans and T. M. Cover. Cooperative broadcast. *IEEE Trans. on Info. Theory*, 20(3):317–324, May 1974.

[2] W. Shi, T. W. Sun, and R. D. Wesel. Optimal binary distributed detection. In *Proc. of 2000 IEEE International Symposium on Information Theory*, page 678, June 2000.

[3] T. M. Cover. Broadcast channels. *IEEE Trans. on Info. Theory*, 18(1):2–14, January 1972.

[4] P. P. Bergmans. Random coding theorem for the broadcast channels with degraded components. *IEEE Trans. on Info. Theory*, 19(2):197–207, March 1973.

[5] P. P. Bergmans. A simple converse for broadcast channels with additive white Gaussian noise. *IEEE Trans. on Info. Theory*, 20(2):279–280, March 1974.

[6] T. M. Cover. Comments on broadcast channels. *IEEE Trans. on Info. Theory*, 44(6):2524–2530, October 1998.

[7] L. Wei. Coded modulation with unequal error protection. *IEEE Trans. on Comm.*, 41(10):1439–1449, October 1993.

[8] S. Gadkari and K. Rose. Time-division versus superposition coded modulation schemes for unequal error protection. *IEEE Trans. on Comm.*, 47(3):370–379, March 1999.

[9] X. Wang and M. T. Orchard. Design of superposition coded modulation for unequal protection. In *Proceedings of ICC2001*, pages 4120–416, June 2001.

[10] T. M. Cover and J. A. Thomas. *Elements of Information Theory.* John Wiley & Sons, Inc., 1991.

[11] C. E. Shannon. A mathematical theory of communication. *Bell System Technical Journal*, 1948.

[12] C. E. Shannon. Certain results in coding with multilevel/phase signals. *Information and Control*, 1, 1957.

[13] R. G. Gallarger. *Information Theory and Reliable Communications.* Wiley Series in Telecommunications, USA, 1968.

[14] C. Berro, A. Clavieux, and P. Thitimajshima. Near Shannon limit error-correcting coding: turbo codes. In *Proceedings of ICC1993*, pages 1064–1070, May 1993.

[15] Christina Fragouli. *Turbo Code Design for High Spectral Efficiency.* PhD thesis, University of California at Los Angeles, September 2000.

[16] P. Robertson and T. Wörz. Bandwidth-efficient Turbo Trellis-Coded Modulation using punctured component codes. *IEEE J. Select. Areas Commun.*, 16(2):206–218, February 1998.

[17] U. Wachsmann, F. H. Fischer, and J. B. Huber. Multilevel codes: theoretical concepts and practical design rules. *IEEE Trans. on Info. Theory*, 45(5):1361–1391, July 1999.

[18] R. D. Wesel, X. Liu, J. M. Cioffi, and C. Komninakis. Constellation labeling for linear encoders. *IEEE Trans. on Info. Theory*, 47(6):2417–2431, September 2001.

[19] C. Fragouli and R. D. Wesel. Turbo-encoder design for symbol-interleavered parallel concatenated trellis-coded modulation. *IEEE Trans. on Comm.*, 49(3):425–434, March 2001.

[20] S. Benedetto, D. Divsalar, G. Montorsi, and F. Pollara. Parallel concatenated trellis coded modulation. In *Proc. IEEE Int. Conf. Communications 1996*, pages 974–978, June 1996.

[21] S. Benedetto and G. Montorsi. Unveiling turbo codes: some results on parallel concatenated coding schemes. *IEEE Trans. on Info. Theory*, 42(2):409–428, March 1996.

[22] R. D. Wesel. Reduced-state representation for trellis code error event diagrams. *IEEE Trans. on Comm. Accepted for publication.*

[23] D. Divsalar and R. J. McEliece. On the design of concatenated coding systems with interleavers. *TMO Progress Report 42-134*, August 1998.

[24] N. Chayat and S. Shamai. Iterative soft onion peeling for multi-access and broadcast channels. In *Proceedings of 9th International Symposium on Personal, Indoor, and Mobile Radio Communications (PIMRC'98)*, pages 1385–1390, September 1998.

[25] G. Ungerboeck. Channel coding with multilevel/phase signals. *IEEE Trans. on Info. Theory*, 28(1):55–67, January 1982.

[26] A. R. Calderbank and N. Seshadri. Multilevel codes for unequal error protection. *IEEE Trans. on Info. Theory*, 39(4):1234–1248, July 1993.

[27] K. Zeger and A. Gersho. Pseudo-Gray coding. *IEEE Trans. on Comm.*, 38(12):2147–2157, December 1990.

[28] T. W. Sun and R. D. Wesel. Constellation labeling for error-resilient source coding of PAM. In *Proc. of 35th Annual Conference on Information Sciences and Systems*, March 2001.

[29] L. H. Harper. Optimal assignments of numbers to vertices. *J. Soc. Indust. Appl. Math.*, 12(1):131–135, March 1964.

[30] F. Gray. Pulse Code Communications. *U.S. Patent 2632058*, March 1953.

[31] S. S. Iyengar, R. L. Kashyap, and R. N. Madan. Distributed sensor networks: Introduction to the special section. *IEEE Trans. on Syst., Man Cybern.*, 21, Sept. 1991.

[32] J. N. Tsistsiklis. Decentralized detection. In *Advances in Statistical Signal Processing, Signal Detection, vol. 2, H. V. Poor and J. B. Thomas, Eds. Greenwich, CT: JAI*, 1993.

[33] W. Shi, T. W. Sun, and R. D. Wesel. Optimal binary distributed detection. In *33rd Asilomar Conf. on Signals, Systems & Computers*, pages 675–679, October 1999.

[34] W. A. Hashlamoun and P. K. Varshney. Near-optimum quantization for signal detection. *IEEE Trans. on Comm.*, 44(3):294–297, March 1996.

[35] W. A. Hashlamoun, P. K. Varshney, and V.N.S.Samarasooriya. A tight upper bound on the Bayesian probability of error. 16(2):220–224, February 1994.

[36] H. Avi-Itzhak and T. Diep. Arbitrarily tight upper and lower bounds on the Bayesian probability of error. 18(1):89–91, January 1996.

[37] M. Grötschel, L. Lovász, and A. Schrijver. *Geometric Algorithms and Combinatorial Optimization.* New York: Springer-Verlag, 1988.

[38] L. Hörmander. *Notions of Convexity.* Birkhauser, Boston, 1994.

[39] S. Moshavi. Multi-user detection for DS/CDMA communications. *IEEE Trans. on Comm.*, 34(10):124–136, October 1996.

[40] P. Patel and J. Holtzman. Analysis of a simple successive interference cancellation scheme in a DS/CDMA system. *IEEE J. Select. Areas Commun.*, 12(5):796–807, June 1994.

[41] S. Sun, L. K. Rasmusen, T. J. Lim, and H. Sugimoto. A matrix-algebraic approach to linear hybrid interference cancellation in CDMA. In *ICUPC'98.*, pages 1319–1323, October 1998.

[42] L. K. Rasmussen *et al.*. Impact of estimation error on multiuser detection in CDMA. In *48th IEEE Vehicular Technology Conf.*, pages 1844–1848, May 1998.

[43] Q. Zhang, P. K. Varshney, and R. D. Wesel. Optimal distributed binary hypothesis testing with independent identical sensors. In *2000 Conf. on Information Science & Systems*, pages WA7b1–6, March 2000.